Doped Perovskite Materials for Solid Oxide Fuel Cell (SOFC) Anodes and Electrochemical Oxygen Sensors

William Donald Penwell

Thesis Submitted to the Faculty of Graduate and Postdoctoral Studies in partial fulfillment of the requirements for the M.Sc. Degree in Chemistry

Department of Chemistry
Faculty of Science
University of Ottawa

Table of Contents

List of Figures

List of Tables

List of Abbreviations

t-tolerance factor

SOFC- solid oxide fuel cell

IT-SOFC-intermediate temperature solid oxide fuel cell

LT-SOFC- low temperature solid oxide fuel cell

XRD- X-Ray diffraction

p-XRD- powder X-ray diffraction

SEM-scanning electron microscopy

EDS- energy dispersive spectroscopy

σ- conductivity

σ_T - conductivity

σ_i-ionic conductivity

σ_e-electronic conductivity

MIEC- mixed ionic/electronic conductor

OCV-open circuit voltage

R_{ct}-charge transfer resistance

R_p-polarization resistance

R_s-serial resistance

i_o-exchange current density

PEMFC- proton exchange membrane fuel cell

PAFC- phosphoric acid fuel cell

MCFC- molten carbonate fuel cell

AFC- alkaline fuel cell

TPD- triple phase boundary

YSZ- yttria stabilized zirconia

SDC- samarium doped ceria

GDC- gadolinium doped ceria

LSM- lanthanum strontium manganate ($La_{0.8}Sr_{0.2}MnO_3$)

LSCF- lanthanum strontium cobalt ferrite ($La_{0.6}Sr_{0.4}Co_{0.2}Fe_{0.8}O_3$)

LSCM- lanthanum strontium chromium manganate ($La_{0.8}Sr_{0.2}Cr_{0.5}Mn_{0.5}O_3$)

TEC- thermal expansion coefficient

pO_2- partial oxygen pressure

ρ- volume resistivity

S- sensor response

EIS- electrochemical impedance spectroscopy

CA- chronoamperometry

MFC- mass flow controller

BCF- $Ba_{0.95}Ce_{0.05}FeO_{3-\delta}$

SCF- $Sm_{0.95}Ce_{0.05}FeO_{3-\delta}$

SCF-Ni- $Sm_{0.95}Ce_{0.05}Fe_{0.97}Ni_{0.03}O_{3-\delta}$

SCF-Co- $Sm_{0.95}Ce_{0.05}Fe_{0.97}Co_{0.03}O_{3-\delta}$

Abstract

This work focused on the study of three independent projects involving perovskite oxide materials and their applications as solid oxide fuel cell (SOFC) anodes and electrochemical oxygen sensors. The underlying theme is the versatility and tune-ability of the perovskite structure. Reactivity and conductivity (ionic as well as electronic) are modified to optimize performance in a specific application.

The effect of Ce doping on the structure and the conductivity of $BaFeO_3$ perovskite materials is investigated and the resulting materials are applied as oxygen sensors. The new perovskite family, $Ba_{1-x}Ce_xFeO_{3-\delta}$ (x=0, 0.01, 0.03, and 0.05), was prepared via a sol-gel method. Powder XRD indicates a hexagonal structure for $BaFeO_3$ with a change to a cubic perovskite upon Cerium doping at the A site. The solubility limit of Ce at the A site was experimentally determined to be between 5-7 mol %. Bulk, electronic and ionic conductivities of $BaFeO_{3-\delta}$ and $Ba_{0.95}Ce_{0.05}FeO_{3-\delta}$ were measured in air at temperatures up to 1000˚C. Cerium doping increases the conductivity throughout the entire temperature range with a more pronounced effect at higher temperatures. At 800˚C the conductivity of $Ba_{0.95}Ce_{.05}FeO_{3-\delta}$ reaches 3.3 S/cm. Pellets of $Ba_{0.95}Ce_{.05}FeO_{3-\delta}$ were tested as gas sensors at 500 and 700˚C and show a linear, reproducible response to O_2.

Promising perovskite anodes have been tested in high sulfur fuel feeds. A series of perovskite solid oxide fuel cell (SOFC) anode materials: $Sm_{0.95}Ce_{0.05}FeO_{3-\delta}$, $Sm_{0.95}Ce_{0.05}Fe_{0.97}Ni_{0.03}O_{3-\delta}$ and $Sm_{0.95}Ce_{0.05}Fe_{0.97}Co_{0.03}O_{3-\delta}$ have been tested for sulfur tolerance at 500°C. The introduction of the extreme 5% H_2S enhances the performance of these anodes, verified by EIS and CA experiments. Post mortem analyses indicate that the performance enhancement arises from the partial sulfidation of the anode, leading to the formation of FeS_2, Sm_3S_4 and S on the perovskite surface. Testing in lower concentrations of sulfur, more common in sour fuels, 0.5% H_2S, also enhances the performance of these materials. The SCF-Co anode shows promising stability and an increase in exchange current density, i_o, from 13.72 to 127.02 mA/cm^2 when switching from H_2 to 0.5% H_2S/99.5% H_2 fuel composition. Recovery tests performed on the SCF-Co anode conclude that the open cell voltage (OCV) and power density of these cells recover within 4 hours of H_2S removal. We conclude that the formation of metal sulfide species is only partially reversible, yielding an anode material with an overall lower R_{ct} upon switching back to pure H_2. Combining their performance in sulfur containing fuels with their previously reported coke tolerance makes these perovskites especially attractive as low temperature SOFC anodes in sour fuels.

A new perovskite family $Ba_{1-x}Y_xMoO_3$ (x=0-0.05) has been investigated in regards to electrical conductivity and performance as IT-SOFC anode materials for the oxidation of H_2. Refinement of p-XRD spectra as well as SEM imaging conclude that the solubility limit of Y doping at the A site is 5 mol%, beyond which Y_2O_3 segregation occurs. The undoped $BaMoO_3$ sample has a colossal room temperature conductivity of 2500 S/cm in dry H_2. All materials maintain metallic conductivity in the temperature range of 25-1000°C with resistance increasing with Y doping. The $Ba_{1-x}Y_xMoO_3$ (x=0, 0.05) materials exhibit good performance as SOFC anode materials between 500-800°C, with R_{ct} values at 500°C in dry H_2 of 3.15 and 6.33 ohm*cm^2 respectively. The catalytic performance of these perovskite anodes is directly related to electronic conductivity, as concluded from composite anode performance.

Claim to Original Research

I, William D. Penwell performed all relevant experimental work and drafted the manuscripts for this thesis. All work presented herein is published or in preparation for publication.

Journal Publications Relevant to this thesis:

Chapter 3: W.D. Penwell, J.B. Giorgi, Sensors and Actuators B: Chemical 191 (2014) 171.

Chapter 4: S.M. Bukhari, W.D. Penwell, J.B. Giorgi, ECS Transactions 57 (2013) 1507.

Summary

This work focused on the study of three independent projects involving perovskite oxide materials and their applications as solid oxide fuel cell (SOFC) anodes and electrochemical oxygen sensors. The underlying theme is the versatility and tune-ability of the perovskite structure. Reactivity and conductivity (ionic as well as electronic) are modified to optimize performance in a specific application.

In Chapter 3 I investigated the structural and electronic effects of A site Ce doping in $BaFeO_{3-\delta}$. The experimental solubility limit of Ce at the A site was determined to be 5 mol%. Ce doping increased both the electronic and ionic conductivity of these materials, making them applicable as sensors for the detection of oxygen. The sensor behavior of the $Ba_{0.95}Ce_{0.05}FeO_{3-\delta}$ was measured at temperatures of 500°C and 700°C and a defect chemical model was inferred from the response data.

In Chapter 4 I focused on the $Sm_{0.95}Ce_{0.05}Fe_{1-x}M_xO_{3-\delta}$ perovskite materials where the dopant M is either Co or Ni in 3 mol%. These materials had previously been shown to be active as SOFC anode materials at intermediate temperatures (500-800°C) for H_2 and CH_4 oxidation. The primary goal of this work was to test the sulfur tolerance of these materials at 500°C. An extremely high concentration of H_2S (0.5-5%) in the fuel stream was used to accelerate anode poisoning. Interestingly, these materials show drastically improved performance when fed with H_2S, a rare case in comparison to typical state of the art anode materials. The performance increase was confirmed by AC impedance spectroscopy and DC chronoamperometry experiments. Post-mortem analysis of these fuel cells showed that that the partial sulfidation of the perovskite anode leads to a more electronically conductive and more reactive anode material for fuel oxidation. As well, the sulfidation is limited to the perovskite surface, with the interior of

the material remaining un-affected. The Co doped material performed the best, and was further tested for recovery when switching back to H_2 from sulfur containing fuels.

Finally, In Chapter 5 I investigated the effect of Y doping in $BaMoO_3$, with the primary goal of increasing the ionic conductivity of the material. These molybdenum perovskites have colossal electronic conductivities, as high as 2500 S/cm in dry H_2, which decrease with increasing concentrations of Y. These materials were then tested as SOFC anode materials at temperatures of 500-800°C in dry H_2. The undoped material exhibited the most promising performance, with low values for charge transfer resistance and high exchange current densities. The redox behavior of these materials was most interesting; these perovskites rapidly oxidize to a scheelite structure ($BaMoO_4$) at elevated temperatures when exposed to air. This puts a high demand on the Pyrex seal at the anode side of the SOFC test apparatus; we hypothesize that slight leakages lead to partial oxidation to the scheelite structure during fuel cell operation, evident from post mortem X-Ray diffraction (XRD). As well, drawing current from the button cell may lead to partial oxidation at the anode-electrolyte interface from the diffusion of oxide species through the SDC electrolyte. These molybdenum perovskite materials may offer improved performance as SOFC anodes with further optimization of the gas seal.

Acknowledgments

First and foremost I would like to express my gratitude to Dr. Javier Giorgi, my supervisor and mentor for all work outlined in this thesis. The inspiration and guidance he provided throughout this research project have been crucial for my success and enjoyment of the chemistry. His patience, generosity and sincere optimism are greatly appreciated.

I would also like to thank all current and former members of the Giorgi group, especially Julie O'Brien for her invaluable help with instrumental and experimental procedures. I would also like to thank Dr. Yun Liu and Dr. Tara Kell for help with experimental imaging and XRD respectively.

Finally, I would like dedicate this work to my family and friends, who have given me the utmost of confidence and support in every endeavor I have undertaken. Thank you.

Chapter 1
Introduction

1.1 Thesis Scope

This thesis work focuses on the development of new perovskite materials with applications towards solid-state gas sensors and solid oxide fuel cell (SOFC) anodes. Chapter 1 covers an introduction to perovskites, their history and applications. As well, the applications of perovskites for SOFCs and semiconductor oxygen sensors are thoroughly discussed. This work was fundamentally carried out in a general procedure of synthesis, complete structural and electrochemical characterization, followed by demonstrated application. Therefore, Chapter 2 covers the variety of synthetic and analytic procedures used as well as details regarding the electrochemical procedures and apparatus.

Within Chapter 3, the material of interest is an alkali-earth perovskite $BaFeO_3$. As mentioned throughout this introduction, the ferrites offer many unique advantages over other perovskites while also being a relatively un-investigated system. The doping of Ce at the A site in $BaFeO_3$ is performed and its effect on structure, ionic and electronic conductivity is thoroughly investigated. The 5% Ce doped material, $Ba_{1-x}Ce_xFeO_{3-\delta}$, is then applied as a conductometric gas sensor for the detection of oxygen at elevated temperatures.

Chapter 4 of this work deals with the sulfur tolerance of some previously developed perovskites reported in our group. Perovskites of the form $Sm_{0.95}Ce_{0.05}Fe_{1-x}M_xO_{3-\delta}$ where M= Ni, Co have been reported as catalytically active IT-SOFC anode materials for the direct utilization of H_2 and hydrocarbon fuels. The work outlined in Chapter 3 tests three anode materials ($Sm_{0.95}Ce_{0.05}FeO_{3-\delta}$, $Sm_{0.95}Ce_{0.05}Fe_{0.97}Co_{0.03}O_{3-\delta}$, and $Sm_{0.95}Ce_{0.05}Fe_{0.97}Ni_{0.03}O_{3-\delta}$) in high level

H_2S fuels of 0.5% and 5%. The anodes are electrochemically tested at 500°C with complete post-mortem analyses to investigate the effect of sulfur impurities on fuel cell performance.

Finally, Chapter 5 investigates a family of molybdenum based perovskites. As mentioned throughout this introduction, Mo perovskites have high electronic conductivities and are catalytically active as SOFC anode materials. The effect of A site Y doping in $BaMoO_3$ is investigated in an attempt to increase the ionic conductivity of these perovskites for application as anode materials for H_2. The effect of dopant on structure and conductivity is investigated as well as the electrochemical testing of these materials as SOFC anodes.

1.2 Perovskites

1.2.1 Structure and History

The perovskite structure is one of the oldest, most studied configurations in solid-state inorganic chemistry. Perovskite was originally the name given to the $CaTiO_3$ mineral discovered in the early 1900s by Russian scientist Gustav Rose, in honor of mineralogist Lev Perovski. It has since become a general name to describe the family of materials comprising this structure. Perovskites have a general formula ABX_3 where A and B represent metal cations and X is a charge balancing anion, typically oxygen. These perovskite oxides are therefore described by formula ABO_3. The A site cations are normally alkali, alkali earth or rare earth elements, whereas transition metals are conventionally in the B site. The B site cation is coordinated to 6 oxygen atoms forming a corner sharing octahedral network. The A site cations are larger, and coordinate to 12 oxygen atoms, laying within interstices formed by the octahedral network. The ideal perovskite structure is cubic, as is shown in Figure 1.1 with the A and B site cations represented in green and red respectively. Depending on the relative sizes of both A and B site cations, the B site octahedra tilt, to stabilize the structure. This leads to other structural forms such as orthorhombic, rhombohedral, hexagonal etc.

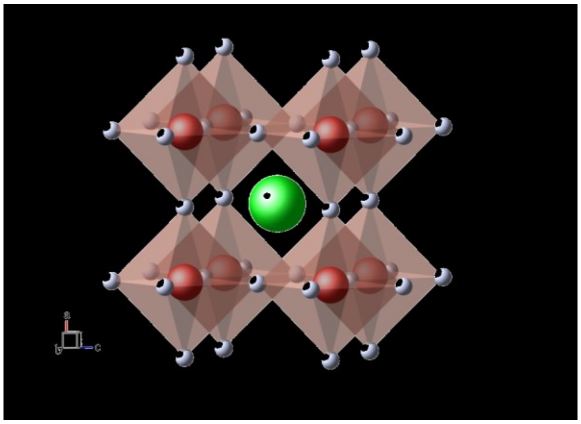

Figure 1.1: General cubic structure of the ABO_3 perovskite oxides. A site = green, B site = red, Oxygen = white

The ability of the perovskite structure to accommodate a variety of metal cations leads to many potential structures, not all of which are cubic. The prediction of the crystal parameters is an important aspect when developing and synthesizing new perovskite materials, therefore extensive work has been done to understand the effect of cation size on the structure. The majority of perovskite structures can be qualitatively predicted using the Goldshmidt Tolerance Factor. Developed in the 1920s, Goldshmidt's tolerance factor relates the ionic radii of the A and B cations to the lattice parameters of the perovskite unit cell [1]. The tolerance factor, t, is derived from trigonometry, utilizing a ratio between the A-O and B-O bond lengths. In the perovskite structure, the anions (oxygen) separate both the A and B cations. This means that the lattice constant, a, can be determined by the sum of the ionic diameters of oxygen and the B-cation, as is shown in Equation 1.1. The relationship between the lattice constant, a, and the A site cation is more complex due to their relative positions in the unit cell. Equation 1.2 is derived from the Pythagoras theorem where, in an ideal cubic perovskite, a is equal to $\sqrt{2}$ times the sum of ionic radii of the A cation and oxygen. Also, in the ideal cubic structure the contact distance between the A and B site cations are equal to each other, leading to Equation 1.3. Since most elements do not satisfy the requirements for the ideal structure, the tolerance factor, *t*, is included and is a direct ratio of the A-O to B-O bond lengths in the perovskite (Equation 1.4).

$$a = 2(r_B + r_O) \qquad [1.1]$$

$$a = \sqrt{2}(r_A + r_O) \qquad [1.2]$$

$$2(r_B + r_O) = \sqrt{2}(r_A + r_O) \qquad [1.3]$$

$$t = \frac{r_a + r_o}{\sqrt{2}(r_b + r_o)} \qquad [1.4]$$

The value of *t* is calculated and used to qualitatively determine the stability of the perovskite structure. Values between 0.9-1.0 are said to be the ideal case, giving rise to cubic perovskite structures where the A and B cation radii match perfectly. If, for example, a smaller A site metal cation is used, the B site octahedra tilt to accommodate the smaller A cation radius and the tolerance factor decreases. Generally, if a combination of A and B metals gives a *t* value of 0.8-1.0, the perovskite structure will be obtained in some form. Table 1.1 illustrates the relationship of *t*-value and potential perovskite structure.

Table 1.1: Effect of tolerance factor on possible perovskite structure [2].

t-value	Effect	Possible Structure
>1	A-site cations are too large to fit into their interstices	Hexagonal perovskite
~0.9-1.0	A-site and B-site cations fit exactly into their allotted sites (Ideal condition)	Cubic Perovskite
0.75-0.9	A-site cations are too small to fit into their allotted sites	Orthorhombic and Rhombohedral
< 0.71	Both A-site cations and B-site cations are of same size	Correndum and Ilmenite structures

1.2.2 Elemental Doping and Oxygen Stoichiometry

Over 90% of the elements from the periodic table can be accommodated in the perovskite structure, leading to a wide range of possible material combinations. This ability to include most elements allows one to easily tailor the material properties for specific applications by doping at the A and/or B site. Elemental doping has been shown to enhance many favorable properties such as magnetism, electrical conductivity, surface area, mechanical strength, catalytic reactivity etc. [3–5]. The dopant is typically chosen to specifically enhance a certain property of the material. Depending on the nature of the material, the dopant can drastically affect the band structure and hence the electronic properties. As well, dopants of varying oxidation states are conventionally used to introduce oxygen vacancies within the perovskite [4]. The majority of perovskites fall into three subcategories depending on the relative oxidation states of the A and B site cations (Table 1.2). However, the perovskite structure is highly tolerant to oxide vacancies and can therefore accommodate elements of various oxidation states in either the A and/or B sites. For example, a perovskite with trivalent A and B site cations would have a general formula $A^{+3}B^{+3}O_3$. By substituting a divalent metal for the B site cation, the perovskite structure necessarily loses oxygen in the form of vacancies to obey charge neutrality. This leads to the form $A^{+3}B^{+3}_{1-x}B^{+2}_{x}\ O_{3-\delta}$ where x equals the fraction of dopant and δ is the degree of oxygen vacancies. The structure can be further modified by additional doping at the A site, leading for example to a formula $A^{+3}_{1-x}A^{+2}_{x}B^{+3}_{1-y}B^{+2}_{y}O_{3-\delta}$. Clearly, the perovskite system can accommodate a large level of dopants and become quite complex.

Table 1.2: Perovskite oxidation state classifications and examples.

Relative Oxidation States	**Examples**
$A^{+3}B^{+3}O_3$	$SmFeO_3$
$A^{+2}B^{+4}O_3$	$BaFeO_3$ $BaMoO_3$
$A^{+1}B^{+5}O_3$	$NaWO_3$

1.2.3 Conductivity of the Perovskites

A key characteristic of the perovskite structure is its ability to conduct both electrons and ionic species, thus leading to them being labeled as Mixed Electronic and Ionic Conductors (MIECs). This mixed conductivity in the perovskites allows for their use in many applications from catalysis to fuel cells to gas sensors. Therefore the understanding and optimization of perovskite conductivity is currently an area of high interest. For the purposes of this work, the total conductivity of a perovskite is equal to the sum of the ionic and electronic conductivities as is shown in Equation 1.5.

$$\sigma_{total} = \sigma_{elecronic} + \sigma_{ionic} \qquad [1.5]$$

Perovskites are further classified as being either p or n type semi-conductors. In a p type material, the primary charge carriers are electron holes whereas in an n type material the carriers are electrons. While this classification is based on band structure, p/n type conductivities typically show a reversal of the atmospheric effect on total conductivity. P-type materials have increased conductivities in oxidizing atmospheres such as air or oxygen and decreased conductivities in reducing gases. N-type materials are the opposite, with increased conductivities in a reducing atmosphere. Perovskites that exhibit n-type behavior are primarily electronic conductors whereas p-type perovskites have mixed conductivities. Some perovskites have been shown to exhibit metallic conductivity behavior; almost exclusively electronic conductivity that decreases with increasing temperature. For example, Ikeda et al. reported a room temperature conductivity of 1.96×10^5 $\mathrm{Scm^{-1}}$ for a single-crystal sample of $SrMoO_3$, the highest conductivity value of any oxide material [6].

Ionic conductivity in perovskites is especially important for certain applications such as sensors and SOFC electrode materials. As mentioned previously, the doping of certain elements into the perovskite structure can lead to the formation of defects, allowing for the conduction of ionic species. The ionic conductivity is essentially the ‘hopping’ of charge carrying ions through site vacancies in the crystalline lattice. A defective structure, oxygen vacant in this case, is necessary for this conduction to occur. The energy required for ionic conduction in perovskites is typically quite large; therefore the majority of perovskites only conduct at elevated temperatures. Ionic conductivity in perovskites is described as a thermally activated process, increasing exponentially with temperature. Perovskites have been demonstrated to conduct several types of ions, as is shown in Table 1.3 [4]. The mobile ionic species of interest for this thesis work is primarily the oxide anion, O^{2-}.

Table 1.3: Examples of ionic conductivity in perovskite materials [4].

Perovskite	Ionic Species	Temperature	σ_{ionic} (S/cm)
$La_{0.8}Sr_{0.2}Ga_{0.8}Mg_{0.2}O_{2.85}$	O^{2-}	800°C	1.5×10^{-1}
$SrCe_{0.95}Yb_{0.05}O_{3-\delta}$	H^{+}	900°C	1×10^{-2}
$La_{0.51}Li_{0.34}TiO_{2.94}$	Li^{+}	27°C	1.4×10^{-3}
$CsPbCl_3$	Cl^{-}	500°C	1.2×10^{-3}
$CsPbBr_3$	Br^{-}	500°C	8×10^{-4}

1.2.4 Perovskite Applications

Due to their elemental flexibility and unique electronic properties, perovskite oxides have found applications in a variety of chemical fields [3]. Two applications are of particular interest for this thesis work and are therefore discussed in detail within the following section. These applications are: perovskites as solid oxide fuel cell (SOFCs) anode materials and as electrochemical gas sensors.

1.3 Solid Oxide Fuel Cells

1.3.1 Introduction and History

The growing environmental and economic concerns on the use of highly polluting fossil fuels is a continued driving force to find new, green energy sources for the production of electricity. Fuel cells are widely believed to be the technology of the future and are an area of extensive research in the scientific field. A fuel cell is defined as an electrochemical device capable of directly converting chemical energy to electricity. The operating principal of a fuel cell is quite simple; a fuel source, typically H_2, is oxidized at the anode and releases electrons to an external circuit. At the cathode, an oxidant (oxygen) is electrochemically reduced. The anode and cathode are separated by an electrolyte that conducts ionic species, thus completing the circuit. The net result is the production of electricity, heat and water with low emissions and extremely high efficiencies as is shown in Equation 1.6.

$$Hydrogen + Oxygen \rightarrow Water + Heat + Electricity \qquad [1.6]$$

The principles of a fuel cell were first developed in 1839 by William Grove, who was studying the electrolysis of water to produce hydrogen and oxygen. He discovered that, when switched off, an electrolysis cell constructed with sulfuric acid and Pt catalysts produced a small current. The term 'fuel cell' was later coined by Mond and Langer where, in 1889, they developed an electrolyte supported cell with porous Pt electrodes that operated on H_2 and O_2[7–9]. Currently, 5 major types of fuel cells can be identified based upon the electrolyte used: Proton Exchange Membrane Fuel Cells (PEMFCs), Solid Oxide Fuel Cells (SOFCs), Phosphoric Acid Fuel Cell (PAFCs), Molten Carbonate Fuel Cells (MCFCs) and Alkaline Fuel Cells (AFCs).

Table 1.4 lists the common fuel cell types and their respective operating temperatures, efficiencies and electrolytes.

Table 1.4: The five types of fuel cell devices and their respective parameters [9].

	Electrolyte	**Cathode**	**Anode**	**Operating Temperature**
AFC	Liquid – KOH	Pt/Au	Pt/Pd	25-100°
PEMFC	Polymer	Polytetrafluoroethylene-Pt-C		80-100°C
PAFC	H_3PO_4	Polytetrafluoroethylene-Pt-C		200°C
MCFC	Li_2CO_3	Ni	Li-NiO	650°C
SOFC	YSZ (Y_2O_3-ZrO_2) SDC ($Sm_xCe_{1-x}O_2$) GDC ($Ga_xCe_{1-x}O_2$)	LSM ($LaSrMnO_3$) LSCF ($LaSrCoFeO_3$)	Ni-YSZ	500-1000°C

Solid oxide fuel cells are a topic of focus for this thesis and will therefore be discussed in detail. SOFCs take their name from the dense, solid ceramic electrolyte used in the fuel cell. The SOFC is operated at high temperatures, typically 500-1000°C, due to the low ionic conductivity of the ceramic electrolyte at ambient temperatures. Historically speaking, research into solid ceramic fuel cells began with Nernst in the late 1800s with his discovery of high temperature ionic conductivity in doped zirconia [8,10,11]. Today, yttria stabilized zirconia (YSZ) remains the most common electrolyte material for high temperature SOFCs whereas doped ceria materials are used for low temperature operation. Baur and Preis were the first to demonstrate a functional SOFC in the 1930s using a YSZ electrolyte, although the cell current output was quite low [12]. Nevertheless, this work illustrated the concept of a solid ceramic fuel cell operating at high temperatures. A schematic of a SOFC operating on H_2 fuel is shown in Figure 1.2. The fuel, H_2, is oxidized at the anode in the presence of oxygen dianions, releasing electrons to an external circuit. At the cathode, electrons reduce O_2 in air to produce oxygen dianions that then migrate through the electrolyte, thus completing an electronic circuit. The electrode half reactions and overall cell reaction are shown in Equations 1.7 to 1.9.

Cathode $$\frac{1}{2}O_2 + 2e^- \rightarrow O^{2-} \quad [1.7]$$

Anode $$H_2 + O^{2-} \rightarrow H_2O + 2e^- \quad [1.8]$$

Overall $$H_2 + \frac{1}{2}O_2 \rightarrow H_2O \quad [1.9]$$

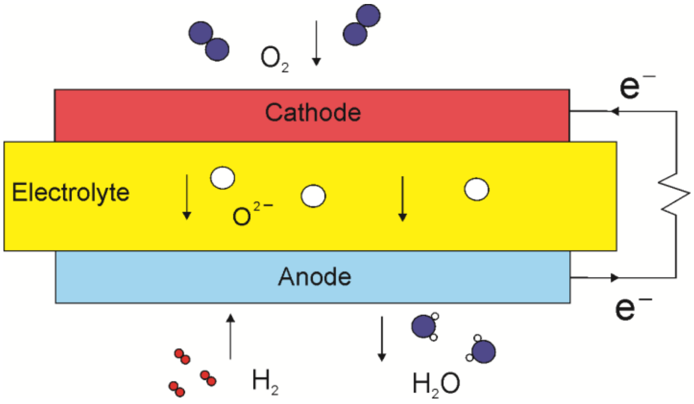

Figure 1.2: Schematic showing the principal operation of a SOFC with H_2 fuel

SOFCs offer several advantages when compared to other fuel cell devices. The operation at high temperature allows SOFCs to oxidize several types of fuel, not relying solely on pure H_2. For example, the SOFC can utilize fuel sources such as natural gas (methane, carbon monoxide), liquid hydrocarbon fuels (biodiesel, ethanol etc) and also sour fuels containing sulfides. This fuel flexibility is derived not only from the facility of direct oxidation at high temperature, but also from the high temperature internal reforming at the anode, readily converting the natural fuels into available hydrogen or methane. High temperature operation also allows for the use of non-noble metal catalysts for cathode and anode materials, drastically reducing overall costs. Along with being fuel flexible, SOFCs have the advantage of a solid, thermally and mechanically stable electrolyte. Other fuel cell types rely on liquid or polymer electrolytes that suffer from poisoning and thermal degradation, limiting the device applications [13,14]. Despite these advantages, SOFCs have failed to find commercial success, mainly due to high materials costs resulting from the high temperature operation. In order to increase their commercial viability, an intense area of research focuses on optimizing the materials to reduce the overall cost of the SOFC device.

1.3.2 SOFC Materials

Electrolyte

The SOFC electrolyte plays the key role in conducting ionic species between the electrodes, completing the electrical circuit. The material should have sufficiently high ionic and low electronic conductivity to avoid a short circuit across the cell. Additionally, the material must be stable in both oxidizing and reducing atmospheres at the operating temperature, and capable of forming a thin, dense film. Currently, 8-mol% Y doped ZrO_2 is the electrolyte of choice for high temperature fuel cells due to its ionic conductivity, stability and compatibility with other cell components. However, YSZ is limited to high temperature operation due to its poor ionic conductivity at temperatures below 800°C. A target temperature for SOFC operation is 500°C, reducing the requirement for high temperature materials and lowering the cost. As well, this improves the balance of plant so that the generation of heat may be used for further energy production, therefore maximizing efficiency of the device. These factors have led to the development of several other materials for intermediate and low temperature SOFC electrolytes. Promising candidates include doped-ceria materials as well as perovskites such as lanthanum gallate and calcium titanate. Table 1.5 lists the most common SOFC electrolytes and their ionic conductivities at 800°C in air [15].The electrolyte material used in this thesis work is 20 mol% samarium doped ceria(SDC, $(CeO_2)_{0.80}(Sm_2O_3)_{0.20}$), a doped ceria material with fluorite-type structure. SDC functions well at intermediate to low temperatures, with an ionic conductivity of 5×10^{-3} S/cm at 500°C, but suffers from partial instability under the reducing atmosphere of the anode [8,16]. The partial reduction of SDC in H_2 at the anode side of the cell leads to current leakage and an overall reduced open circuit voltage[16–18]. This is unfavorable however the advantage of high ionic conductivity at low temperatures led the choice of SDC for this work. In general, the electrolyte materials of today are adequately established, and are cheap enough to be scaled for SOFC commercialization.

Table 1.5: Common electrolyte materials and their ionic conductivities at 800°C in air [15].

Electrolyte Material	**σ_i at 800°C (S/cm)**
$(Y_2O_3)_{0.08}(ZrO_2)_{0.92}$	0.03
$(ScO_3)_{0.08}(ZrO_2)_{0.92}$	0.013
$Ce_{0.8}Gd_{0.2}O_{1.9}$	0.053
$Ce_{0.8}Sm_{0.2}O_{1.9}$	0.095
$La_{0.9}Sr_{0.1}Ga_{0.8}Mg_{0.2}O_{2.85}$	0.1

Cathode

Materials for SOFC cathodes have been well established over the past 50 years, with extensive work done to optimize conductivity, thermal stability and facilitating the oxygen reduction reaction. Cathode materials should be chemically compatible with the electrolyte system and also have sufficiently high conductivities (typically > 100 S/cm) to enhance reactivity [5,8,15]. The combination of ionic and electronic conductivity is required to enhance the size of the triple phase boundary (TPB), the reactive sites at the cathode where oxygen is reduced and transferred to the electrolyte. Figure 1.3 illustrates the TPB reaction taking place at the cathode side of a SOFC. In a purely electronic conducting cathode, such as $La_{0.8}Sr_{0.2}MnO_3$ (LSM), the TPB sites are limited to the interface between cathode-electrolyte.

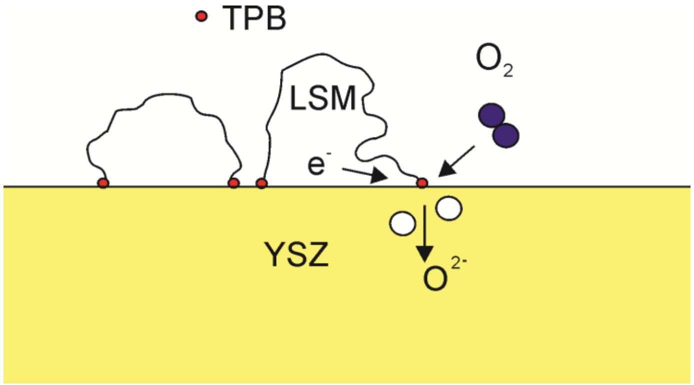

Figure 1.3: Triple Phase Boundary (TPB) reactive sites at the SOFC cathode when using pure LSM.

Today, the convention is to use an electronically conductive perovskite material mixed with the electrolyte of choice, thus extending the TPB throughout the electrode and drastically improving performance. For example, high temperature SOFCs typically use 50% w/w $La_{0.8}Sr_{0.2}MnO_3$/YSZ; a composite cathode to provide electronic conductivity from the perovskite and ionic conductivity from YSZ. At lower temperatures a composite cathode is also employed, using 50% w/w $La_{0.6}Sr_{0.4}Co_{0.2}Fe_{0.8}O_3$ (LSCF) and SDC. A complication arises from the use of chromium containing interconnect materials, where the cathode can undergo Cr poisoning at high temperatures in the oxidizing atmosphere [19]. Although the development of Cr tolerant cathode materials is currently an area of interest, composite anodes of LSM and LSCF generally have adequate performance for SOFC device applications.

Anode

The anode of the SOFC encounters the most rigorous conditions and requirements, and is therefore a limiting factor in the commercialization of the device. The anodes crucial role lies in providing reactive sites for fuel oxidation to occur in the presence of oxide anions delivered by the electrolyte. The anode must be stable at high temperatures in reducing atmospheres consisting of H_2 to gaseous hydrocarbons, depending on the fuel source used. As well, the anode must satisfy the same requirements as cathode materials, i.e. chemically compatible with the electrolyte, thermally stable, and sufficiently high ionic and electronic conductivities at the operating temperature. This must also be matched by maintaining fuel tolerance; the anode material must be highly tolerant to carbon poisoning from hydrocarbon fuels and resistant to sulfur in sour fuels. Clearly, the development of a cheap, suitable material for the SOFC anode is a non-trivial task.

The conventional anode material used in high temperature SOFCs is a Ni-YSZ cermet. Here, Ni provides reactivity for fuel oxidation and electronic conductivity whereas YSZ is used to provide ionic conductivity and increase compatibility with the electrolyte. Similar to the cathode, fuel oxidation occurs at the anode TPB where H_2, and oxide anions react on the metal catalyst to release electrons. In the case of Ni-YSZ cermets, YSZ extends the ionic conductivity throughout the anode to allow for drastically increased area of the TPB. This is illustrated in Figure 1.4.

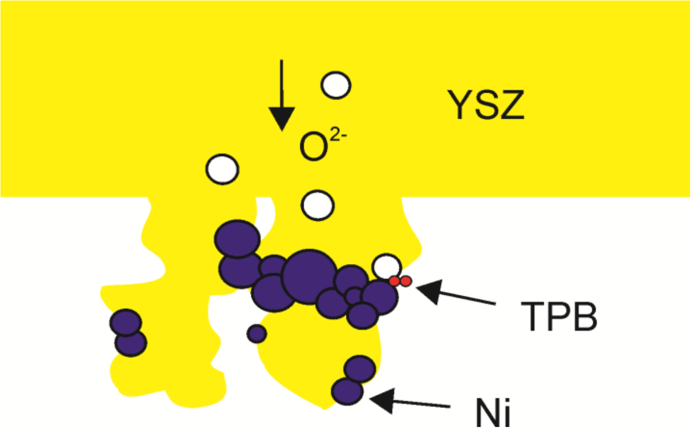

Figure 1.4: Ni-YSZ cermet anode with enhanced TPB reaction sites.

Ni-YSZ anode materials perform quite well at temperatures greater than 800°C when utilizing H_2 fuels. For example, as of 2013 several companies currently market SOFC devices utilizing Ni based anodes such as Bloom Energy (CA, USA) and Delphi (International). Ni-YSZ cermet anodes are relatively cheap and effective but suffer from severe carbon and sulfur poisoning when exposed to hydrocarbon or sour gas fuels [20–23]. Also, the low ionic conductivity of YSZ restricts its use as an electrolyte to high operating temperatures. This complicates the SOFC device from a commercialization standpoint; the restriction on fuels limits the device to pure H_2 or to the engineering of external fuel reformers, and the high temperature operation requires the use of expensive ceramic supports.

The sulfur tolerance of several anode materials is investigated in this thesis work, therefore the sulfur poisoning effect of an SOFC anode will be discussed more in depth than coking. Ni-YSZ cermet anodes suffer severely when exposed to even ppm levels of sulfur, normally hydrogen sulfide, in the fuel stream. This is a serious issue for SOFC commercialization since the world's current natural gas sources contain anywhere from 50 ppm to >1% H_2S, as is shown in Table 1.6.

Table 1.6: Typical concentrations of H_2S in natural gas [24].

Fuel type	Typical composition	H_2S concentration
Syngas	H_2, CO, CO_2, H_2O, N_2	100–300 ppm
Biogas	H_2, CO, CO_2, CH_4, H_2O, N_2	50–200 ppm
Sour Gas	H_2, CO_2, N_2, C_2H_6, CH_4	>1%

The high sensitivity of Ni-YSZ to sulfur containing fuels is due to the affinity of the Ni catalyst to undergo side reactions at elevated temperatures. At the operating temperature of a Ni-based SOFC, H_2S undergoes rapid adsorption and chemisorption at the TPB active sites on the anode surface [20,22–24]. Many potential decomposition pathways for H_2S have been hypothesized, most of which involve the deposition of sulfur and formation of a nickel sulfide species. A few commonly reported reactions for H_2S are illustrated below [24]. The first reaction involves direct oxidation of H_2S, a favorable mechanism for the durability of the anode. The second, however, leads to the formation of elemental sulfur at the TPB of the anode, ultimately blocking the reactive sites. The third reaction involves high temperature reforming of H_2S, producing H_2 fuel but also sulfur in the process.

$$H_2S + 3O^{2-} \rightarrow H_2O + SO_2 + 6e^- \qquad [1.10]$$

$$H_2S + O^{2-} \rightarrow H_2O + S + 2e^- \qquad [1.11]$$

$$H_2S \rightarrow H_2 + S \qquad [1.12]$$

As well, H_2S can react directly with Ni to produce a nickel sulfide species, forming large crystalline materials that may detrimentally alter the anode microstructure, conductivity and performance [22,25]. A few of these possible reactions are listed below. The Ni-S materials may also agglomerate and eventually lead to anode delamination. Interestingly, some studies have shown that partial sulfidation of the Ni to nickel sulfide actually improves anode performance, with higher power outputs and lower charge transfer resistances in 10% H_2S than in pure H_2 [26–29]. This effect will be discussed further in Chapter 3.

$$Ni + H_2S \rightarrow H_2 + NiS \qquad [1.13]$$

$$3Ni + xH_2S \rightarrow xH_2 + Ni_3S_x \qquad [1.14]$$

Evidently, Ni cermets have many drawbacks as SOFC anode materials; therefore the main area of SOFC research to date has been in the development of alternative anode materials, with an emphasis on low temperature operation and coke/sulfur tolerance. The development of a novel, catalytically active, fuel flexible anode material could allow SOFCs to operate on today's natural gas sources while maintaining a reasonable materials cost for commercialization.

Perovskite Anodes

Perovskites offer unique advantages over traditional metal-cermet type anodes and, in the past decade, have been an area of extensive research in the SOFC field. The high temperature stability, MIEC behavior and elemental flexibility of the perovskite structure are attractive attributes for SOFC anode research.

One of the first and most widely studied perovskite anode materials is a doped chromate, LSCM ($La_{0.75}Sr_{0.25}Cr_{0.5}Mn_{0.5}O_3$), based the success of the $LaCrO_3$ interconnect material. In 2003, Tao and Irvine studied the *p*-type conductivity of LSCM and its stability in both oxidizing and reducing atmospheres [30]. It was demonstrated as both an anode and cathode material for symmetrical SOFCs with a suitable thermal expansion coefficient (TEC) for ceria and yttria based electrolytes [31,32]. Unfortunately, its catalytic activity was deemed too low for practical use. Nevertheless, the redox stability and high conductivity of LSCM in reducing atmospheres led to a spur of research into perovskite type anodes. Many variants of lanthanum chromate have been investigated that show promising performance, as listed in Table 1.7. For example, Sauvet et al. investigated the effect of Sr and Ru concentrations in a $La_{1-x}Sr_xCr_{1-y}R_yO_3$ perovskite system. The optimum performance was obtained when x=0.30 (Ru concentration had little effect), with R_{ct} values of 3.7 Ω cm^2 in H_2[33]. The inclusion of B site Ni was also investigated and led to an anode material with high stability in methane that showed no carbon deposition after testing. A wide range of chromium based systems have been investigated, all of which exhibit high conductivities and R_{ct} values comparable to Ni-YSZ, however their stability in sulfur containing fuels is open to question.

Table 1.7: Performance of some Cr and Ti perovskite anodes in H_2 and CH_4.

Anode	Fuel	Temp. (°C)	R_{ct} (Ω*cm^2)	Ref.
$La_{0.75}Sr_{0.25}Cr_{0.5}Mn_{0.5}O_3$	H_2	900	0.26	[30]
	CH_4	900	0.87	
$La_{0.7}Sr_{0.3}Cr_{0.95}Ru_{0.05}O_3$/YSZ	H_2	750	3.7	[33]
	CH_4	750	40	
$La_{0.75}Sr_{0.25}Cr_{0.5}Mn_{0.5}O_3$/GDC	CH_4	800	0.44	[34]
$La_{0.5}Sr_{0.5}Ti_{0.5}Ce_{0.5}O_3$	H_2	850	0.2	[23]
	CH_4	700	1.3	

Another family of perovskites heavily investigated for SOFC anodes are the strontium titanates. A and B site doped $SrTiO_3$ materials have been demonstrated to have impressive conductivities as well as high stabilities in a reducing atmosphere [23,35–38]. For example, Hui et al. studied the effect of yttria and cobalt doping in $SrTiO_3$ and found that $Sr_{0.85}Y_{0.10}Ti_{0.95}Co_{0.05}O_{3-\delta}$ has a total conductivity of 45 S/cm at 800°C with a large contribution of ionic conductivity [37]. Marina et al. have employed heavily doped $SrTiO_3$ based anodes utilizing H_2 fuels with polarization resistances as low as 0.2 Ω*cm^2 at 850°C [23]. The strontium titanates clearly display MIEC behavior and good catalytic performance although are only partially tolerant to sulfur and carbon poisoning.

Currently, materials research has expanded beyond the chromates and titanates to more diverse perovskite families. Two systems of interest for this thesis work are the ferrites and molybdates. The inclusion of Fe at the B site has been shown to increase the conductivity and catalytic activity in several perovskites [23,35,39,40]. As well, previous work in our group has focused on the effect of A site Ce and B site transition metal doping in $SmFeO_3$ [41–44]. The inclusion of 5% Ce at the A site changes the material from a *p* to *n* type semiconductor and stabilizes the perovskite in a reducing atmosphere. The inclusion of low level (3%) transition metal doping at the B site makes these perovskites catalytically active for the oxidation of H_2 and CH_4 and show high tolerance to coking. The performance of these materials as SOFC anodes is summarized in Table 1.8. Although these anode materials function well in H_2, no work has been done on their tolerance to sulfur containing fuels.

Table 1.8: Performance summary for $SmFeO_3$ anode materials in H_2 and CH_4.

Anode	Fuel	Temp. (°C)	R_{ct} (Ω*cm^2)	Ref.
$Sm_{0.95}Ce_{0.05}FeO_3$	H_2	500	0.65	[44]
	CH_4	550	15.85	
$Sm_{0.95}Ce_{0.05}Fe_{0.97}Ni_{0.03}O_3$	H_2	500	~4.5	[42]
	CH_4	500	61.1	
$Sm_{0.95}Ce_{0.05}Fe_{0.97}Co_{0.03}O_3$	H_2	500	0.97	[41]
	CH_4	500	53.49	

Recently, Mo based perovskites have shown very impressive performances as SOFC anode materials [45–48]. As mentioned previously, the molybdates are some of the most conductive perovskites found to date and Mo has also been shown to be catalytically active for the oxidation of hydrogen as well as hydrocarbons and alcohols [45,48,49]. Perovskites utilizing Mo at the B site are also typically regenerative anode materials; Mo readily undergoes a two electron redox from Mo^{4+}/Mo^{6+}, useful for the removal of coke and sulfur impurities from the anode [45]. In addition to high conductivities and catalytic reactivity, molybdates have similar thermal expansion coefficients of several common electrolytes for intermediate temperature solid oxide fuel cells (IT-SOFCs), making them even more attractive as anode materials [47]. The doping of transition metals has also been shown to increase the ionic conductivity and anode performance in several Mo perovskites [50]. For example, Zhao et al. investigated the effect of B site Ni doping in the $Sr_2TiMo_{1-x}Ni_xO_{3-\delta}$ perovskite system, yielding high power densities and polarization resistances as low as $0.305\Omega*cm^2$ at 800°C [47]. The high performance of these materials arises from the introduction of oxygen defects, hence increasing the ionic conductivity of the perovskite. The optimization of ionic conductivity and catalytic activity of molybdenum based perovskites may offer a new route to developing a fuel flexible IT-SOFC anode material.

1.4 Electrochemical Gas Sensors

1.4.1 Introduction and Description

The increasing population of our planet has directly led to the increase in manufacturing and production of food and materials to meet our daily needs. This increase in manufacturing also leads to more pollutants entering our atmosphere and reducing the quality of breathable air. The control and monitoring of hazardous gases in industrial work places is becoming more and more stringent. As well, the majority of our transportation methods rely on the operation of lean-burn internal combustion engines. These engines require a constant monitoring of O_2

concentration. This has led to the development of sensor materials for the detection of various gases. Semi-conductor gas sensors, also known as conductometric sensors, function by a change in material conductivity when exposed to various gases. These sensors are currently used in many industrial facilities for detecting reducing and oxidizing gases as well as in the exhaust manifolds of our vehicles.

Doped tin oxide, SnO_2, is the main sensor material currently employed for the detection of reducing gases such as H_2, CO, CH_4 etc. However SnO_2 sensors suffer from poor stability in a reducing atmosphere as well as poor reproducibility. TiO_2 semi-conducting sensors have been investigated as alternatives although these too have considerable drawbacks; TiO_2 has a very low sensitivity above 400°C, therefore limiting the operating temperature, and Ti also suffers from oxidation issues in an oxidizing atmosphere [51,52]. Perovskites have been employed as alternative materials for solid state gas sensors for the detection of oxidizing and reducing gases [53]. The application of doped $SmFeO_3$ sensors for the detection of reducing gases has been investigated within our group [54,55]. The use of perovskites for the detection of oxygen is a topic of interest for this thesis and is therefore discussed in detail in the following section.

1.4.2 Oxygen Sensors

Today's automobiles typically operate on lean burn combustion engines in which the concentration of O_2 in the exhaust must be constantly monitored. A highly sensitive sensor is required due to the constantly changing ratio of air to fuel (lambda value) injected into the combustion engine. The concentration of oxygen is currently monitored using a zirconia based material working as a lambda probe [56]. This probe functions by a change in material conductivity when exposed to various concentrations of oxygen in the fuel exhaust. These zirconia sensors have several drawbacks such as high cost and high temperature dependent sensitivity. Therefore, much research in the past decade has focused on the development of alternative O_2 sensing materials for lean-burn exhaust systems. Metal oxides such as SnO_2 and TiO_2 show promising sensitivity but maintain a temperature dependent sensitivity as well as long term stability issues [57].

Perovskites of the type ABO_3 are an excellent alternative to the zirconia sensors currently employed. Several perovskites have been demonstrated to have impressive conductivities that are also highly sensitive to the atmospheric concentration of O_2. Some of these perovskites also show a low temperature dependent sensitivity, making them attractive for conductometric exhaust sensors [53,57,58]. The most commonly demonstrated perovskite sensor material is $SrTiO_3$, which shows typical n-type behavior at low partial oxygen pressure (pO_2) and p-type behavior at high pO_2. $SrTiO_3$ materials have demonstrated low temperature dependent O_2 sensitivity through the incorporation of transition metal and rare earth metal dopants [59–62]. Specifically, the incorporation of B site Fe plays a key role in increasing the conductivity of these materials, improving the operating range of pO_2 as well as lowering the temperature dependence of sensitivity [61,63–65]. Other alkali-earth titanates, such as $CaTiO_3$ and $BaTiO_3$, have also been investigated as semi-conductor oxygen sensors. The defect structure of $BaTiO_3$ is very similar to $SrTiO_3$ and it therefore behaves similarly but with a higher conductivity and improved sensitivity [53,66,67]. Examples of some perovskite oxygen sensors are listed in Table 1.9.

Table 1.9: Examples of perovskite oxides investigated for the detection of oxygen.

Perovskite	Ref.
$SrTiO_3$	[53]
$LaFe_{1-x}Cu_xO_3$	[68]
$La_{0.05}Sr_{0.95}Ti_{0.65}Fe_{0.35}O_{3-\delta}$	[69]
$BaTi_{0.99}Nb_{0.01}O_3$	[65]
$SrTi_{1-x}Fe_xO_{3-\delta}$	[61]
$SrFeO_{2.5+x}$	[58]

Aside from the titanates, ferrites have recently been shown to have impressive response times and low temperature dependent sensitivities [61,69–72]. Un-doped alkali earth ferrites such as $SrFeO_3$ have been shown to have rapid equilibration with oxygen at relatively low temperatures, indicating that these materials should have fast response times as resistive oxygen sensors [58,61]. This work clearly demonstrates the potential of Fe based perovskites as temperature independent O_2 sensors.

1.5 References

[1] V. Goldschmidt, Naturwissenschaften 21 (1926) 477.

[2] C. Shinzer, Distortion of Perovskites (1998) URL: .http://www.ccp14.ac.uk/ccp/web-mirrors/pki/uni/pki/members/schinzer/stru_chem/perov/di_gold.html

[3] A.S.B. Ruyan, G. Rustum, Mater. Res. Innov. (2000) 3.

[4] H. Iwahara, in:, T. Ishihara (Ed.), Perovskite Oxide Solid Oxide Fuel Cells, Springer US, Boston, MA, 2009, pp. 45–63.

[5] J.T.S. Irvine, Perovskite Oxide for Solid Oxide Fuel Cells, Springer US, Boston, MA, 2009.

[6] I. Nagai, N. Shirakawa, S. Ikeda, R. Iwasaki, H. Nishimura, M. Kosaka, Appl. Phys. Lett. 87 (2005) 024105.

[7] S.C. Singhal, J. Mizusaki, Solid Oxide Fuel Cells IX, 2nd ed., The Electrochemical Society, Pennington, New Jersey USA, 2005.

[8] S.C. Singhal, K. Kendall, High Temperature Solid Oxide Fuel Cells, Elsevier Ltd, New York, USA, 2003.

[9] R.M. Ormerod, Chem. Soc. Rev. 32 (2003) 17.

[10] W. Nernst, Electrical Incandescent Lamp, US906550 A, 1897.

[11] W. Nernst, Glower for Electric Lamps, US 685 730, 1899.

[12] E. Baur, H. Preis, Ztschr. Elektrochem. 43 (1937) 727.

[13] G.F. Mclean, T. Niet, N. Djilali, Int. J. Hydrogen Energy 27 (2002) 507.

[14] E.H. Yu, U. Krewer, K. Scott, Energies 3 (2010) 1499.

[15] C. Sun, R. Hui, J. Roller, J. Solid State Electrochem. 14 (2009) 1125.

[16] H. Shi, W. Zhou, R. Ran, Z. Shao, J. Power Sources 195 (2010) 393.

[17] T. Miyashita, ECS Trans. 28 (2010) 39.

[18] T. Miyashita, Electrochem. Solid-State Lett. 14 (2011) B66.

[19] J. Richter, P. Holtappels, T. Graule, T. Nakamura, L.J. Gauckler, Monatshefte Für Chemie - Chem. Mon. 140 (2009) 985.

[20] W.. Zhu, S.. Deevi, Mater. Sci. Eng. 362 (2003) 228.

[21] Y. Matsuzaki, I. Yasuda, Solid State Ionics 132 (2000) 261.

[22] Z. Cheng, J.-H. Wang, Y. Choi, L. Yang, M.C. Lin, M. Liu, Energy Environ. Sci. 4 (2011) 4380.

[23] C. Sun, U. Stimming, J. Power Sources 171 (2007) 247.

[24] M. Gong, X. Liu, J. Trembly, C. Johnson, J. Power Sources 168 (2007) 289.

[25] M. Lo Faro, V. Antonucci, P.L. Antonucci, a. S. Aricò, Fuel 102 (2012) 554.

[26] J.S. O'Brien, J.B. Giorgi, J. Power Sources 200 (2012) 14.

[27] C.M. Grgicak, J.B. Giorgi, J. Phys. Chem. C 111 (2007) 15446.

[28] C.M. Grgicak, R.G. Green, J.B. Giorgi, J. Power Sources 179 (2008) 317.

[29] C.M. Grgicak, M.M. Pakulska, J.S. O'Brien, J.B. Giorgi, J. Power Sources 183 (2008) 26.

[30] S. Tao, J.T.S. Irvine, Nat. Mater. 2 (2003) 320.

[31] S. Tao, J.T.S. Irvine, J. Electrochem. Soc. 151 (2004) A252.

[32] D.M. Bastidas, S. Tao, J.T.S. Irvine, J. Mater. Chem. 16 (2006) 1603.

[33] A. Sauvet, J. Fouletier, Electrochem. Commun. 47 (2001) 987.

[34] S.P. Jiang, X.J. Chen, S.H. Chan, J.T. Kwok, J. Electrochem. Soc. 153 (2006) A850.

[35] D.P. Fagg, V. V Kharton, A. V Kovalevsky, A.P. Viskup, J. Eur. Ceram. Soc. 21 (2001) 1831.

[36] S. Hui, A. Petric, J. Eur. Ceram. Soc. 22 (2002) 1673.

[37] S. Hui, A. Petric, Mater. Res. Bull. 37 (2002) 1215.

[38] S. Suthirakun, G. Xiao, S.C. Ammal, F. Chen, H.-C. zur Loye, A. Heyden, J. Power Sources 245 (2014) 875.

[39] O. Paper, J. Solid State Electrochem. 3 (1998) 7.

[40] A. Sin, E. Kopnin, Y. Dubitsky, A. Zaopo, A.S. Aricò, L.R. Gullo, D. La Rosa, V. Antonucci, J. Power Sources 145 (2005) 68.

[41] S.M. Bukhari, J.B. Giorgi, ECS Trans. 33 (2011) 81.

[42] S.M. Bukhari, J.B. Giorgi, ECS Trans. 35 (2011) 1539.

[43] S.M. Bukhari, J.B. Giorgi, Solid State Ionics 180 (2009) 198.

[44] S.M. Bukhari, J.B. Giorgi, J. Power Sources 198 (2012) 51.

[45] Q. Liu, D.E. Bugaris, G. Xiao, M. Chmara, S. Ma, H.-C. zur Loye, M.D. Amiridis, F. Chen, J. Power Sources 196 (2011) 9148.

[46] T.G. Howell, C.P. Kuhnell, T.L. Reitz, a. M. Sukeshini, R.N. Singh, J. Power Sources 231 (2013) 279.

[47] B. He, Z. Wang, L. Zhao, X. Pan, X. Wu, C. Xia, J. Power Sources 241 (2013) 627.

[48] Y.-H. et al. Huang, Science (80-.). 312 (2006) 254.

[49] J. Kubo, W. Ueda, Mater. Res. Bull. 44 (2009) 906.

[50] R. Martínez-Coronado, J. a. Alonso, a. Aguadero, M.T. Fernández-Díaz, Int. J. Hydrogen Energy (2013) 1.

[51] H.-S. Kim, W.-T. Moon, Y.-K. Jun, S.-H. Hong, Sensors Actuators B Chem. 120 (2006) 63.

[52] C. Lu, Z. Chen, Sensors Actuators B Chem. 140 (2009) 109.

[53] J.W. Fergus, Sensors Actuators B Chem. 123 (2007) 1169.

[54] S.M. Bukhari, J.B. Giorgi, J. Electrochem. Soc. 158 (2011) J159.

[55] S.M. Bukhari, J.B. Giorgi, Sensors Actuators B Chem. 181 (2013) 153.

[56] P.T. Moseley, Sensors Actuators B Chem. 6 (1992) 149.

[57] R. Moos, F. Rettig, A. Hürland, C. Plog, Sensors Actuators B Chem. 93 (2003) 43.

[58] M.L. Post, B.W. Sanders, P. Kennepohl, Sensors Actuators B Chem. 14 (1993) 13.

[59] C. Yu, Y. Shimizu, H. Arai, Sensors and Actuators 14 (1988) 309.

[60] W. Menesklou, K.H. Hardtl, E. Ivers-tiffee, Sensors Actuators B Chem. 59 (1999) 184.

[61] A. Rothschild, S.J. Litzelman, H.L. Tuller, W. Menesklou, T. Schneider, E. Ivers-Tiffée, Sensors Actuators B Chem. 108 (2005) 223.

[62] R. Moos, W. Menesklou, K.H. Hardtl, Sensors Actuators B Chem. (2000) 178.

[63] J. Gerblinger, H. Meixner, Sensors Actuators B Chem. 6 (1992) 231.

[64] F. Rettig, R. Moos, C. Plog, J. Electroceramics (2004) 733.

[65] U. Lampe, J. Gerblinger, H. Meixner, Sensors Actuators B Chem. 7 (1992) 787.

[66] J. Jeong, E.J. Lee, Y.H. Han, J. Eur. Ceram. Soc. 27 (2007) 1159.

[67] T. Ishihara, K. Kometani, Y. Nishi, Y. Takita, Sensors Actuators B Chem. 28 (1995) 49.

[68] R. Moos, F. Rettig, Resistiver Sauerstoffsensor, DE 10114645 C1, 2003.

[69] K. Sahner, R. Moos, N. Izu, W. Shin, N. Murayama, Sensors Actuators B Chem. 113 (2006) 112.

[70] A. Rothschild, W. Menesklou, H.L. Tuller, E. Ivers-tiffe, Chem. Mater. (2006) 3651.

[71] J.J. Tunney, M.L. Post, J. Electroceramics 51 (2000) 63.

[72] J.J. Tunney, M.L. Post, X. Du, D. Yang, J. Electrochem. Soc. 149 (2002) H113.

Chapter 2
Experimental Considerations

2.1 Summary

This chapter aims to cover the general methodologies and experimental techniques utilized throughout this thesis work. The majority of techniques were universal throughout each chapter/for each material and will therefore be covered in a general sense, however detailed descriptions of materials and methods used are available at the beginning of Chapters 3-5.

2.2 Synthetic Route

Generally, the synthesis of perovskites is a straightforward procedure with few chemical steps. Several synthetic routes are utilized throughout the literature however the solid state and sol-gel methods are most commonly used. The solid state method is sometimes referred to as the ‘shake and bake’ synthetic route; solid, metal oxide precursors are thoroughly mixed and then calcined to high temperature to form the perovskite phase. This synthetic route is facile, however it requires a high temperature calcination, typically >1500°C, leading to large crystal/particle sizes and therefore a lower surface area for the perovskite [1,2]. As well, metal evaporation from the sample can alter the desired stoichiometry of the perovskite and the high temperature calcination requires sophisticated equipment and immense energy. Additionally, several intermediate grindings/calcinations may be required to adequately combine precursor materials and obtain a single phase perovskite.

All perovskites investigated in this work were prepared via a sol-gel route. The sol-gel method utilizes a homogeneous mixing of precursor solutions followed by solvent evaporation and finally calcination to obtain the perovskite phase. This method allows for complete mixing of starting materials with the help of a binding agent, requiring a lower temperature calcination to obtain the perovskite in single phase [3]. This ultimately leads to a material with smaller crystallite size and higher surface area.

Precursor materials are conventionally hydrated nitrates of the A and B site metals as well as a binding agent, citric acid in this case. Nitrates are used as opposed to anionic salts to avoid the incorporation of impurities that may remain in the perovskite structure following calcination. The general procedure involves individual dissolution of precursor metal nitrates in ~ 100 mL distilled H_2O followed by combination with aqueous citric acid under vigorous stirring. The ratio of citric acid to total metal ion is 1:1 to ensure adequate binding of precursors. The solution is then stirred overnight with heating at ~100°C to evaporate the solvent, resulting in a gelatinous citrate precursor. The gel precursor is then ground with a mortar and pestle, placed in a crucible and calcined in a high temperature furnace to remove the organic binder. Calcination temperatures required for obtaining the perovskite phase varied depending on the materials used. Typically a temperature of 600-950°C was adequate. Post calcination, the perovskite is thoroughly ground and structurally/electrochemically characterized.

2.3 Material Characterization Techniques

2.3.1 X-Ray Diffraction

X-Ray diffraction is one of the most commonly used characterization techniques in solid-state materials chemistry. All perovskite samples prepared in this thesis were characterized via powder X-ray Diffraction (p-XRD). p-XRD is a valuable tool for the quantitative determination of the crystalline parameters for each sample as well as providing qualitative evidence regarding the purity of the perovskite. XRD works on the principle of Bragg’s Law, where incident X-Rays diffract within a crystal lattice to form a constructive interference pattern. The interference pattern witnessed from a sample is directly related to the wavelength of radiation used and the path length, as is shown in Equation 2.1. Here, d_{hkl} refers to the interspaced distance of lattice planes within the crystal structure, n is and integer, θ is the incident photon angle and λ is the radiation wavelength. Crystallite sizes were calculated according to the Scherrer equation (Equation 2.2). Here, τ is the crystallite size, K is a peak shape factor, λ is the radiation wavelength, β is the peak broadening at half maximum and θ is the Bragg angle.

$$n\lambda = 2d_{hkl}sin\theta \qquad [2.1]$$

$$\tau = \frac{K\lambda}{\beta cos\theta} \qquad [2.2]$$

A Philips PW 1830 powder diffractometer was used to determine the phase composition of the perovskite powders in this work. The instrument used CuK_{α} radiation (λ=1.54 Å) and the scattering angle, 2θ, was scanned between 13-90° at a rate of 0.02°/s. The resulting diffractogram was then completely analyzed using the Panalytical X'PertHighscore Plus software. This software allows for phase indexing to the ICDD Powder Diffraction File database (PDF-4+, 2012) as well as refinement of the diffractogram to determine the lattice parameters of the perovskite unit cell. The refinement was performed using the Reitveld method, where a calculated diffraction pattern is mathematically fit to the experimental spectrum. The Reitveld method utilizes a least-squares fitting procedure, altering specific profile parameters to minimize the residual difference between calculated and experimental patterns [4,5].

2.3.2 Scanning Electron Microscopy

Scanning electron microscopy (SEM) is employed to a large degree in this thesis work. SEM was used to image the as-prepared powders, sintered pellets for conductivity and sensor experiments, as well as fuel cell anode morphologies before and after testing. Coupled to the SEM, energy dispersive spectroscopy (EDS) was used to qualitatively determine the elemental composition of samples. The electron microscope model used is a JEOL JSM-7500 Field Emission SEM with an EDS X-sight attachment.

Samples were prepared on graphite paste or with carbon tape, and no additional coating was applied in order to maintain original microstructure. For fuel cell samples, the button cell was mechanically cracked and mounted horizontally for cross sectional imaging. Imaging was primarily performed in LEI mode, collecting both secondary and backscattered electrons to maximize topographical detail. Acceleration voltage and probe current were adjusted accordingly to avoid sample charging while optimizing resolution. Typical conditions for perovskite powders were: acceleration voltage between 1-2.0 kV, probe current of 8 mA, and a working distance between 7-9 mm. Image exposure time was normally set to 12 seconds. These conditions generally gave adequate resolution up to ~100 000x magnification. For EDS analysis, acceleration voltage was increased to 15-20.0 kV and spectra were recorded in the INCA software. Due to the requirement of 15-20 kV acceleration voltage, EDS measurements are generally performed at magnifications less than 10 000X. This is due to the increased beam spot size when using higher acceleration voltage on the sample. Single spot EDS analysis was generally performed however line analyses were sometimes employed to probe a larger area.

2.4 Conductivity Measurements

2.4.1 4-Point Conductivity

Electronic conductivities of all perovskite materials were measured using a 4-point method on dense, sintered pellets. The 4-point method was chosen in order to avoid contact resistance issues, thereby improving measurement accuracy [6]. Pellets of the perovskites were prepared by weighing between 4-6 grams of sample into a 1 inch die press and pressing to 10 000 – 20 000 lbs using a Carver laboratory press. Masses and pressures specific to each material are included in respective Experimental sections of Chapters 3-5. The perovskites were pressed for ~2 minutes and then placed on individual zirconia discs for sintering. Sintering was performed in a Thermolyne 46100 high temperature furnace to temperatures between 1200-1400°C for 4 hrs. Heating and cooling ramp rates were kept low, usually 2°C/min, in order to avoid cracking the pellet.

Following sintering, the pellets were mechanically cut using a high-speed Dremel equipped with a diamond cutting blade. A rectangular shape, with dimensions generally 12 mm x 6 mm x 1 mm, was chosen to simplify electrode placement. Four small, evenly spaced grooves were cut into the exterior of the pellet followed by wrapping with Pt wire. Each section of Pt wire was tightly bound to the pellet surface and subsequently painted over with Pt paste to ensure a good electrode contact. The pellet was then fired at 800°C for 1 hr with heating/cooling ramp rates of 2°C/min to remove the organic binder from the Pt paste. Figure 2.1 shows a schematic of a pellet prepped for conductivity measurement.

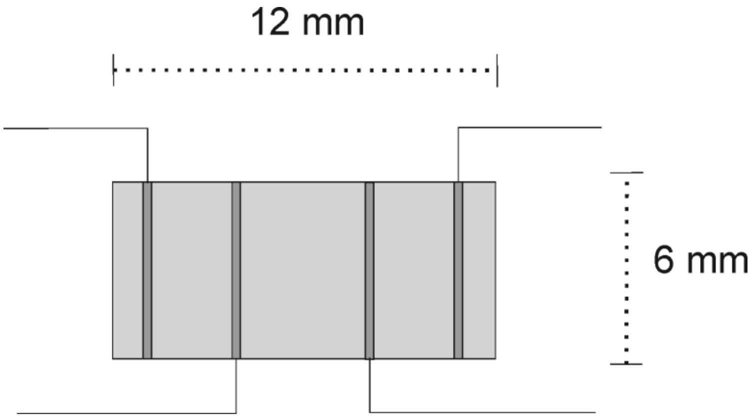

Figure 2.1: Pellet setup for 4-point conductivity measurement.

The pellet is then mounted inside a quartz tube, with 4 lengths of Pt wire serving as leads to the pellet electrodes. The quartz tube is contained within a horizontal tube furnace controlled by a Barber-Colman temperature controller with K-type thermocouple. The quartz tube is sealed on either end with rubber septa, with one end providing a gas inlet and the other an exhaust tube. The atmosphere within the quarts sample chamber was controlled using Alicat Mass flow controllers attached to a 2-way Swagelok fitting allowing for the mixing of gases. The gas flow rate over the pellet was kept a constant 50 sccm. The 4 Pt leads extend from the quartz tube, with 2 attached to a power supply and 2 to a digital multi-meter. The power supply provided a constant current of 100 mA to the outer electrodes and the multi-meter measured the voltage drop across the inner 2 electrodes. Figure 2.2 shows a pellet mounted inside the tube furnace, ready for measurement. Rubber septa and gas lines are omitted from the figure for simplicity.

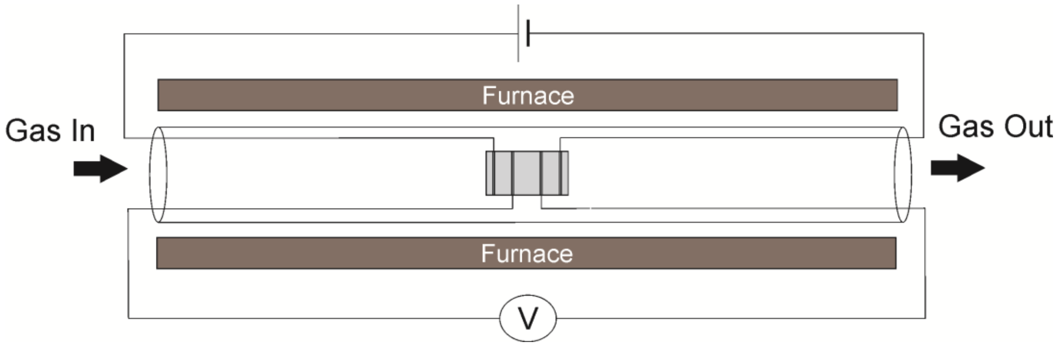

Figure 2.2: Sample setup for 4-point conductivity measurement.

The gases used for conductivity measurements were typically compressed air or oxygen for oxidizing atmospheres and H_2 or 5% H_2/95%N_2 for a reducing atmosphere. Before recording conductivity measurements, the pellets were ramped to 1000°C in the gas of interest for approximately 4 hours and then cooled to room temperature. This pre-heating of the sample leads to more reliable measurements for the following ramp cycles and checks for possible changes upon initial exposure. The temperature was ramped in 50 or 100°C increments and the sample was allowed to equilibrate for at least 30 mins at each temperature. To ensure reproducibility, measurements were made on multiple cycles of both heating and cooling of the furnace. The average voltage drop across the sample was then used to calculate the material resistivity according to Ohm's law and the dimensions of the pellet. Finally, the conductivity in units of S/cm is calculated from the inverse of resistivity.

2.4.2 Ionic vs. Electronic Conductivity Measurements

The contributions of ionic and electronic conductivity to the total conductivity were measured using a 2-point contact method with an Al blocking electrode. The Al blocking electrode stops the flow of O^{2-} species through the sample therefore the measured conductivity is purely electronic. The ionic conductivity is then inferred from the difference between total and electronic conductivities as is shown in Equation 2.3.

$$\sigma_{ionic} = \sigma_{total} - \sigma_{electronic} \qquad [2.3]$$

Similar to the 4-point measurements, 2-point conductivities were measured on dense, sintered pellets of the perovskites. To make the pellets, ~2 grams of sample was weighed into a die and pressed to 15 000 lbs using a Carver laboratory press. The pellets were then sintered on zirconia discs to 1200°C for 4 hrs with heating/cooling ramp rates of 2°C/min. For total conductivity measurements, Pt mesh current collectors (Alfa Aesar, 99.9%) were painted onto either side of a pellet using Pt paste followed by removal of the organic binder at 800°C for 1 hr. For the use of Al blocking electrodes, a similar procedure was followed on two separate perovskite pellets along with the insertion of a thin film of Al. The entire 'sandwiched' array is then heated to 660°C to partially soften the Al film and ensure good contact between the pellets. Figure 2.3 illustrates the pellet setups for 2-point measurements (b) with and (a) without Al blocking electrodes. The Pt leads in this case are attached directly to a power supply providing a constant current of 100 mA and measuring the voltage across the sample.

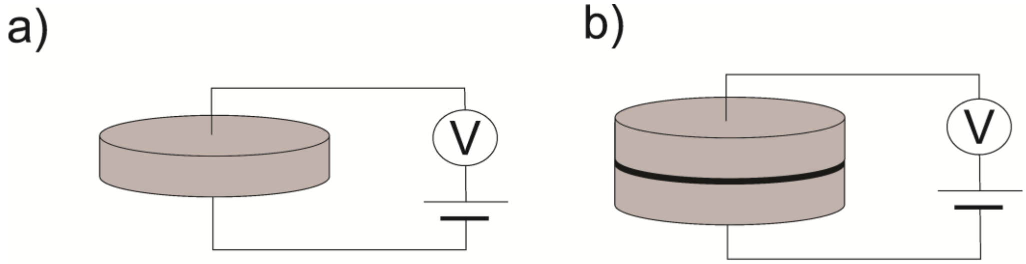

Figure 2.3: Pellet setup for 2-point conductivity measurements.

The volume resistivity, ρ, of the material is calculated according to Equation 2.4. Here, R is the electrical resistance as calculated from Ohm's law, l is the sample thickness and A is the cross sectional area of the pellet. The conductivity, σ, is then calculated as the inverse of resistivity, shown in Equation 2.5. Similar to the 4-point method, samples were pre-heated and cooled in the atmosphere of interest followed by measurement on multiple heating and cooling cycles to ensure reproducibility.

$$\rho = R\frac{A}{l} \qquad [2.4]$$

$$\sigma = \frac{1}{\rho} \qquad [2.5]$$

2.5 Sensor Experiments

Sensor experiments were performed on sintered pellets of perovskites using a 4-point contact method. The experimental setup was identical to that of the 4-point conductivity measurements described in section 2.4.1. The conductivity of the material was recorded at 1 min intervals while changing the concentration of test gas flowing through the quartz sample tube. The total gas flow rate was a constant 50 sccm, maintained with a balance of compressed air.

The sensor response, S, was calculated from the ratio of relative conductivity change according to Equation 2.6.

$$S = 100\% \times \left(\frac{\sigma_{gas} - \sigma_{air}}{\sigma_{air}}\right) \qquad [2.6]$$

2.6 Fuel Cell Testing and Considerations

2.6.1 Button Cell Fabrication

The fuel cells fabricated in this thesis work used a thick, electrolyte supported button cell with a 3 electrode design. The anode and cathode are positioned symmetrically on either side of a ~2 mm SDC-20 disc with a Pt wire wrapped horizontally around the electrolyte to serve as a reference electrode. The button cell configuration is outlined in Figure 2.4.

The main area of focus for this work is in the comparison of anode performance, therefore it is critical to measure anode specific processes separate from the full cell [7,8]. This is made possible by using a reference electrode, Pt in this case. Computational and experimental studies have shown that, when using a reference electrode, cell geometry must meet several requirements in order to produce reliable data [9,10]. For instance, the alignment of cathode and anode is a crucial parameter when fabricating button cells with electrolytes less than ~200 µm. Misalignment of anode and cathode electrodes must not exceed ± 0.1 'electrolyte thicknesses', in order to avoid overpotential errors. In this work, the thick electrolyte allows for more error in alignment; however the electrode alignment is still controlled to the highest degree possible by the use of pre-fabricated masks. As well, the reference electrode is positioned ~ 3 'electrolyte thicknesses' away from both the cathode and anode, reducing cross talk and ensuring electrical isolation. The use of a thick electrolyte, however, necessarily limits the maximum current and power output of the fuel cell. As mentioned, this work focuses on a comparison of anode performances, therefore the relative power densities are considered more important than the absolute value of peak cell power.

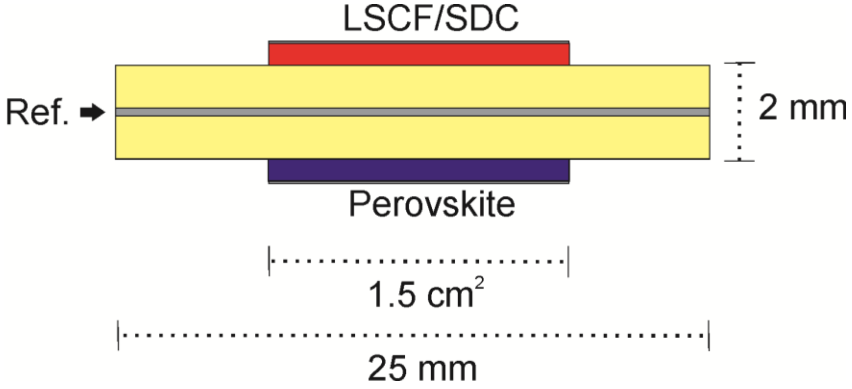

Figure 2.4: Schematic of the SOFC button cell geometry used in this work.

To make the electrolyte, 6 grams of SDC-20 were weighed into a 1 inch die and pressed to 10 000 lbs using a Carver laboratory press. The pellets were then sintered on zirconia discs to 1400°C for 4 hrs with ramp rates of 2°C/min, resulting in an electrolyte thickness of 2 mm. To form the anode, a slurry of perovskite powder was prepared in an emulsion consisting of 20% v/v Triton X-100 and 80% H_2O. The slurry was then painted on one side of the SDC electrolyte in a cast area of 1.5 cm^2 using a mask of the appropriate dimensions and fired at 1400°C for 4 hrs with heating/cooling ramp rates of 2°C/min. In the case of co-sintered anodes, the slurry is prepared in an identical manner but cast painted before sintering the electrolyte. A Pt mesh current collector was then added with additional perovskite slurry and fired again at 1400°C in a similar manner. This leads to a well adhered anode ~100 µm in thickness.

The cathode consists of 50% w/w LSCF (fuelcellmaterials.com) and 50% SDC-20. The addition of SDC forms a composite cathode to increase performance as outlined in Chapter 1. To form the cathode, a slurry was prepared in an emulsion of Triton X-100 and H_2O (same ratios as anode) and painted in a cast area of 1.5 cm^2 on the electrolyte opposite the anode. The cell was sintered at 1400°C with heating/cooling ramp rates of 2°C, followed by addition of a Pt mesh current collector and additional slurry/re-firing. The cathode thickness is also ~100 µm.

The reference electrode consists of Pt wire wrapped around the circumference of the SDC electrolyte. The Pt wire is tightly bound and painted over with Pt paste followed by removal of the organic binder at 800°C for 1 hr with heating/cooling ramp rates of 2°C/min. This completes the button cell fabrication.

2.6.2 Fuel Cell Setup and Electrochemical Considerations

The setup used for fuel cell testing is depicted in Figure 2.5. The apparatus consists of a stainless-steel Ultra-Torr fitting sealed to an alumina support tube with a Viton o-ring. The Ultra-Torr fitting is custom-fit to a Swagelok manifold allowing for the mixing of up to 3 gases. Extending from the manifold (not shown), Swagelok lines connect to MKS mass flow controllers for various gases including; H_2, N_2 and H_2S. The alumina support tube is ~ 30 cm tall, atop of which sits the button cell. Within the support tube, a smaller diameter alumina tube carries fuel gas to the anode side of the button cell. The exhaust travels back down the outer alumina support tube to an exhaust port, venting to the back of the fume hood. Atop the alumina support, the button cell is attached via a Pyrex glass seal to ensure isolation from air. A short section of alumina tube was used as a weight to facilitate the sealing of the cell. The cathode side of the cell is open to air. This entire setup is mounted vertically in a tube furnace controlled by a Barber-Colman temperature controller with K-type thermocouple. Inside the furnace, a Faraday cage is wrapped around a quartz sample tube, inside of which the fuel cell is centered. Three lengths of Pt wire serve as the leads for the anode, cathode and reference electrode respectively.

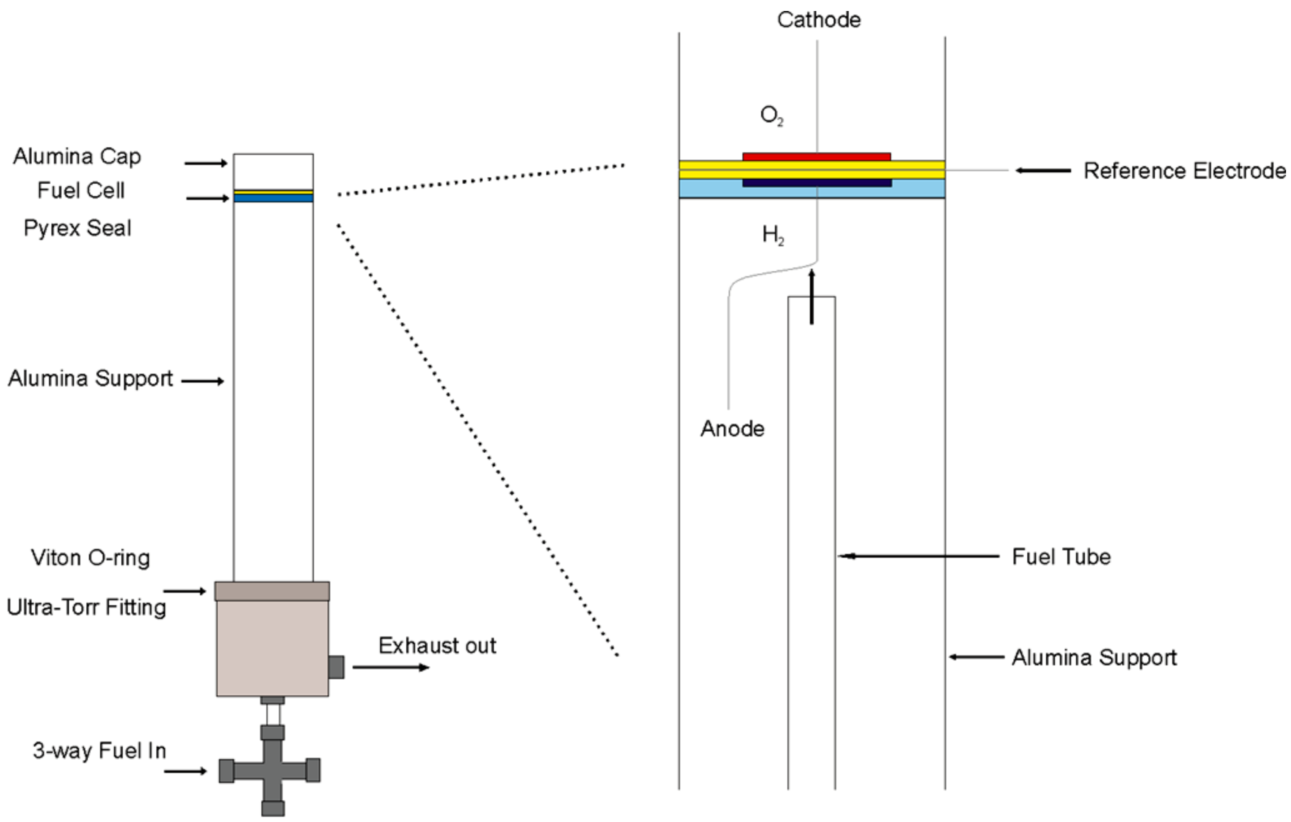

Figure 2.5: Fuel cell test apparatus. The right portion of the figure is blown-up to show the button cell mounted for testing.

Before heating, the entire setup was checked with a digital multi-meter to ensure electrical isolation of electrode leads as well as isolation from the clamps and furnace. The heating is performed slowly, ramp rates of ~5°C/min, to avoid thermal cracking of the cell. The furnace was heated to 950°C for 1 hr to soften the Pyrex ring and seal the button cell followed by cooling at 5°C/min to the operating temperature. The anode was then reduced slowly in H_2, initially with concentrations of 5% H_2 scaling to 100% over the course of 2 hrs. The total flow rate was maintained a constant 50 sccm with a balance of N_2.

2.6.3 Electrochemical Testing

Data Collection

The 3 electrode leads (anode, cathode and reference) are attached to a potentiostat (VoltaLab, 40 PGZ301) for electrochemical measurements. The VoltaLab is controlled via a computer, running VoltaMaster 4 electrochemistry program. The VoltaMaster software allows for the collection of data from various programs that may be sequenced and repeated multiple times.

Electrochemical experiments performed include: open circuit voltage (OCV), electrochemical impedance spectroscopy (EIS) and current amperometry experiments (CA) at various overpotentials. The OCV experiment measures cell potential between anode and cathode vs. time under no applied load. OCV values in this work are low due to the electrolyte used in fabricating the button cells. As discussed previously, the cells constructed for this work use an SDC-20 electrolyte. SDC is known to undergo partial reduction when in a reducing atmosphere at the anode side of the fuel cell. This partial reduction leads to current leakage across the electrolyte and a lower OCV value [11,12]. As well, SDC has issues of low densification, further affecting the OCV of the cell [13]. These drawbacks of using an SDC electrolyte are outweighed by its high ionic conductivity at low temperatures, making it the electrolyte of choice for SOFCs studied in this work. As well, these issues do not affect the results obtained in the following work since the focus is on anode performance comparison, where impedance of the anode versus reference electrode is the most relevant experiment.

Before running a programmed sequence, the cell was checked to ensure both an adequate sealing of the Pyrex and a good electrode contact. To gauge the quality of seal obtained, an OCV experiment was performed for ~2 mins at the operating temperature. If the OCV value was stable, and above 0.95 V, the cell was deemed to be adequately sealed. As well, a single impedance spectrum was collected at OCV at the operating temperature to check the serial resistance (R_s) of the cell. If the R_s value was acceptable, $< 50\ \Omega*\text{cm}^2$ at 500°C, the anode was deemed to have an adequate interfacial contact with the electrolyte and the cell was run for a full battery of experiments. A general programmed sequence of tests involved 20 mins OCV, 6 repeated impedance spectra at OCV in frequencies of 100 kHz to 100 mHz with AC amplitude of 50 mV, and CA experiments at overpotentials of 1000 mV to 0 mV in 50 mV increments. This entire sequence was repeated 7 times for a total experiment time of ~ 14 hrs. In this period it is possible to avoid any changes due to microstructural/poisoning effects. Performance after this time is typically stable therefore values obtained after 14 hrs are typically compared.

Analysis

The 20 mins of OCV data recorded every 2 hours were averaged and plotted versus time. Power density plots were calculated according to $P = I \times V$ where V is the applied overpotential and I is the average current density recorded.

Impedance spectra were collected as Nyquist plots and analysed in the ZView2 software (Scribner Associates). An equivalent circuit model, shown in Figure 2.6, was chosen to fit the high frequency arc of the Nyquist plot. This equivalent circuit model can be abbreviated as ($L_1R_S[R_{CT}CPE_1]$) where L_1 is an inductor to account for impedance of electrode leads and CPE_1 is a constant phase element. The constant phase element is arbitrarily developed to fit typical Nyquist plots of SOFC anodes, primarily the characteristic depressed semi-circle arc. The depressed semi-circle is caused from several overlapping processes, mainly an electrode surface with high roughness and inhomogeneous microstructure [14–16]. The anodes prepared in this work have a porous, rough microstructure where reaction rates are expected to vary slightly throughout the material. These variations in reaction rates as well as the use of a mesh current collector can lead to small variations in the current distribution throughout the anode, thus leading to the characteristic depressed semi-circle. R_s is the serial resistance, corresponding to the high frequency x-intercept on the EIS Nyquist plot. The R_s corresponds to the high electrical resistance from the electrolyte as well as the bulk resistance of the anode material derived from its conductivity. R_{ct} is the charge transfer resistance corresponding to the low frequency x-intercept in the Nyquist plot. The R_{ct} in this case is assumed to be equal to the anode polarization resistance; the area specific resistance directly corresponding to the fuel oxidation reaction occurring at the anode TPB. The anodes studied in this work also exhibited a low frequency 'tail' associated with Warburg diffusion limitations. This element was omitted from the reported analysis in order to minimize errors associated with circuit fitting parameters.

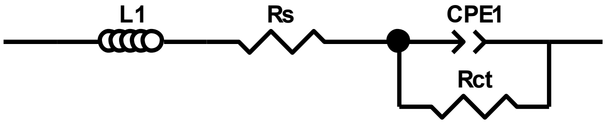

Figure 2.6: Equivalent circuit model used to fit EIS Nyquist plots.

The R_{ct} value obtained from equivalent circuit fitting was further used to calculate the exchange current density, i_0, according to the low field approximated Butler-Volmer equation (Equation 2.7) [17,18]. Here, F is the Faraday constant, R is the universal gas constant, n is the number of electrons involved in the process and T is the temperature. The exchange current density values were calculated for all anode materials and tabulated with the EIS data.

$$i_0 = \frac{RT}{nFR_{ct}} \qquad [2.7]$$

2.7 References

[1] A. Feldhoff, M. Arnold, J. Martynczuk, T.M. Gesing, H. Wang, Solid State Sci. 10 (2008) 689.

[2] H. Taguchi, M. Nagao, K. Tanihata, J. Am. Ceram. Soc. 202 (1992) 201.

[3] M. Niederberger, N. Pinna, J. Polleux, M. Antonietti, Angew. Chemie 43 (2004) 2270.

[4] H.M. Rietveld, J. Appl. Crystallogr. 2 (1969) 65.

[5] H.M. Rietveld, Aust. J. Phys. 41 (1988) 113.

[6] T.R. Kuphaldt, in:, Lessons Electr. Circuits, Fifth Edit, 2006, p. 282.

[7] V. Krishnan, Solid State Ionics 166 (2004) 191.

[8] S. McIntosh, J.M. Vohs, R.J. Gorte, J. Electrochem. Soc. 150 (2003) A1305.

[9] S. Crystal, Solid State Ionics 67 (1994) 215.

[10] J. Rutman, I. Riess, Electrochim. Acta 52 (2007) 6073.

[11] T. Miyashita, ECS Trans. 28 (2010) 39.

[12] T. Miyashita, Electrochem. Solid-State Lett. 14 (2011) B66.

[13] H. Shi, W. Zhou, R. Ran, Z. Shao, J. Power Sources 195 (2010) 393.

[14] S. Koch, M. Mogensen, P. V. Hendriksen, N. Dekker, B. Rietveld, Fuel Cells 6 (2006) 117.

[15] S. Gewies, W.G. Bessler, J. Electrochem. Soc. 155 (2008) B937.

[16] T. Nakamura, T. Kobayashi, K. Yashiro, A. Kaimai, T. Otake, K. Sato, J. Mizusaki, T. Kawada, J. Electrochem. Soc. 155 (2008) B563.

[17] D. a. Noren, M. a. Hoffman, J. Power Sources 152 (2005) 175.

[18] D.R. Peterson, J. Winnick, J. Electrochem. Soc. 145 (1998) 1449.

Chapter 3

Conductivity of Cerium Doped $BaFeO_{3-\delta}$ and Applications for the Detection of Oxygen

The contents of this chapter have been published as:
W.D. Penwell, J.B. Giorgi, Sensors Actuators B Chem. 191 (2014) 171.

Abstract

The effect of Ce doping on the structure and the conductivity of $BaFeO_3$ perovskite materials is investigated and the resulting materials are applied as oxygen sensors. The new perovskite family, $Ba_{1-x}Ce_xFeO_{3-\delta}$ (x=0, 0.01, 0.03, and 0.05), was prepared via a sol-gel method. Powder XRD indicates a hexagonal structure for $BaFeO_3$ with a change to a cubic perovskite upon Cerium doping at the A site. The solubility limit of Ce at the A site was experimentally determined to be between 5-7 mol %. Bulk, electronic and ionic conductivities of $BaFeO_{3-\delta}$ and $Ba_{0.95}Ce_{0.05}FeO_{3-\delta}$ were measured in air at temperatures up to 1000˚C. Cerium doping increases the conductivity throughout the entire temperature range with a more pronounced effect at higher temperatures. At 800˚C the conductivity of $Ba_{0.95}Ce_{.05}FeO_{3-\delta}$ reaches 3.3 S/cm. Pellets of $Ba_{0.95}Ce_{.05}FeO_{3-\delta}$ were tested as gas sensors at 500 and 700˚C and show a linear, reproducible response to O_2.

3.1 Introduction

Perovskites of the type ABO_3 where A=lanthanide and B=transition metal have been demonstrated for a range of applications such as catalysis, anode/cathode materials for solid oxide fuel cells (SOFCs) and electrochemical gas sensors [1–4]. Substitution of various cations into the A and B sites allows for fine tuning of the material properties to better suit the application. The inclusion of alkaline earth metals at the A site has shown to produce oxides with high electronic as well as ionic conductivity [5,6]. These mixed electronic and ionic conductors (MIECs) are of current interest as cathode materials for SOFCs due to their stability and conductivity in high temperature oxidizing atmospheres.

These parameters are equally important in the field of electrochemical gas sensors, where p-type semiconductors are used for the detection of oxidizing gases such as O_2, NO_2 and ozone [3,7]. In particular, the development of temperature independent O_2 sensors is an area of intense research for the automobile industry. The measurement of pO_2 in automobile exhaust systems is currently performed using expensive zirconia based lambda sensors [8]. To reduce manufacturing costs, several groups have focused on semiconducting oxides that show resistivity dependency towards pO_2. Materials based on TiO_2 and CeO_2 have been investigated along with several perovskite materials that show promising temperature independent O_2 sensor behavior [9–11]. For example, perovskite materials $LaCu_{0.3}Fe_{0.7}O_{3-\delta}$ and $La_{0.05}Sr_{0.95}Ti_{0.65}Fe_{0.35}O_{3-\delta}$ have been demonstrated as O_2 sensors with low temperature dependency and fast response times [12]. Also, a previous study showed that doping $BaFeO_3$ with Ta increases its sensitivity towards pO_2 while maintaining a temperature independent response [13]. Post et al. explored the non-stoichiometric $SrFeO_{3-x}$ system showing that not only is the equilibrium between the oxide ions and the gas phase directly related to sensor sensitivity, but also intrinsic phase transitions resulting from rearrangement and changes in the oxidation state of the iron ions produce drastic changes in sensitivity at specific oxygen partial pressures and temperatures. These non-stoichiometric perovskites show extremely high values of sensitivity when tested as conductometric O_2 sensors [14–16]. It is evident in the literature that Fe based perovskites exhibit many of the ideal material properties for O_2 sensing.

Recent studies within our group have shown that doped samarium ferrites have favourable characteristics such as high conductivity and stability in reducing atmospheres, making them useful for SOFC anode materials and gas sensors [4,17–19]. The increased conductivity in the Sm ferrites arises from Cerium doping at the A site, changing the material from a p to n-type semiconductor [19]. The majority of Fe based perovskites utilize a trivalent A site cation (lanthanide) leading to a Fe^{3+} oxide. Less common are Fe^{4+} oxides that contain a divalent A site cation, despite several studies demonstrating enhanced properties such as ferromagnetism and metallic conductivity [20–22]. Combining the stability and conductivity enhancing properties of A site Cerium doping with an oxygen deficient Fe^{4+} oxide should produce a material with high electronic and ionic conductivity.

Here we report on the synthesis, characterization and electrochemical properties of $Ba_{1-x}Ce_xFeO_{3-\delta}$ (x = 0, 0.01, 0.03, and 0.05). Dopant levels greater than 5% were investigated but led to phase segregation; we estimate the solubility of Ce at the A site to be between 5-7 mol %. The x = 0.05 sample showed the most promising results and therefore $Ba_{0.95}Ce_{0.05}FeO_{3-\delta}$ is the focus of this work. The following includes a study of the electronic and ionic conductivity as well as applications as a gas sensor for O_2 at various temperatures.

3.2 Experimental

3.2.1 Synthesis

Powders of $Ba_{1-x}Ce_xFeO_{3-\delta}$ (x=0, 0.01, 0.03, and 0.05) were prepared by decomposition of citrate precursors via a conventional sol-gel method. Barium nitrate ($Ba(NO_3)_2$, AlfaAesar, 99.9%), cerium nitrate hexahydrate ($Ce(NO_3)_3\cdot6H_2O$, AlfaAesar, 99.5%) and iron nitrate nonahydrate($Fe(NO_3)_3\cdot9H_2O$, AlfaAesar, >98%) were weighed according to the desired stoichiometry (Ba_{1-x} + Ce_x : Fe = 1:1) and dissolved in de-ionized water. The metal nitrate solutions were combined and added to aqueous citric acid monohydrate (AlfaAesar, 99%) so that the ratio of citric acid to total metal ion was 1:1. The resulting solution was dried at 120°C for 24 h to form a citrate gel that was then ground and calcined at 950°C for 24 h using heating/cooling ramp rates of 5°C/min.

3.2.2 Characterization

Powder X-Ray Diffraction (XRD, Philips PW 1830) was used to determine the phase composition and lattice parameters of the perovskite powders. The instrument used CuK_α radiation (λ=1.54 Å) and the scattering angle, 2θ, was scanned between 13-90° at a rate of 0.02°/s. Panalytical X'PertHighscore Plus software was used for profile refinement and phases were indexed to the Powder Diffraction File database (JCPDS, 2012).

Scanning electron microscopy (SEM, JEOL JSM-7500F) with an energy dispersive x-ray spectroscopy (EDS X-Sight) attachment was used to image the surface morphology of $Ba_{1-x}Ce_xFeO_{3-\delta}$ (x=0, 0.05) powders/pellets and provide qualitative elemental composition.

3.2.3 Total, Ionic and Electronic Conductivity Measurements

The total conductivity (σ_T) of the materials was measured on circular pellets using the 2 point contact method at temperatures 25-1000°C in air. Pellets (diameter = 6 mm, thickness = 2 mm) of $Ba_{1-x}Ce_xFeO_{3-\delta}$ (x=0, 0.05) were made by pressing 2 grams of powder to 15000 lbs and sintering in air at 1200°C for 4 h with ramp rates of 2°C/min. Platinum mesh (AlfaAesar, 99.9%) was added as a current collector on each face of the circular pellet by adhesion with platinum paste followed by removal of the organic binder at 800°C for 1h. The test chamber setup used a quartz tube heated inside a tube furnace as described previously for sensor experiments [23].

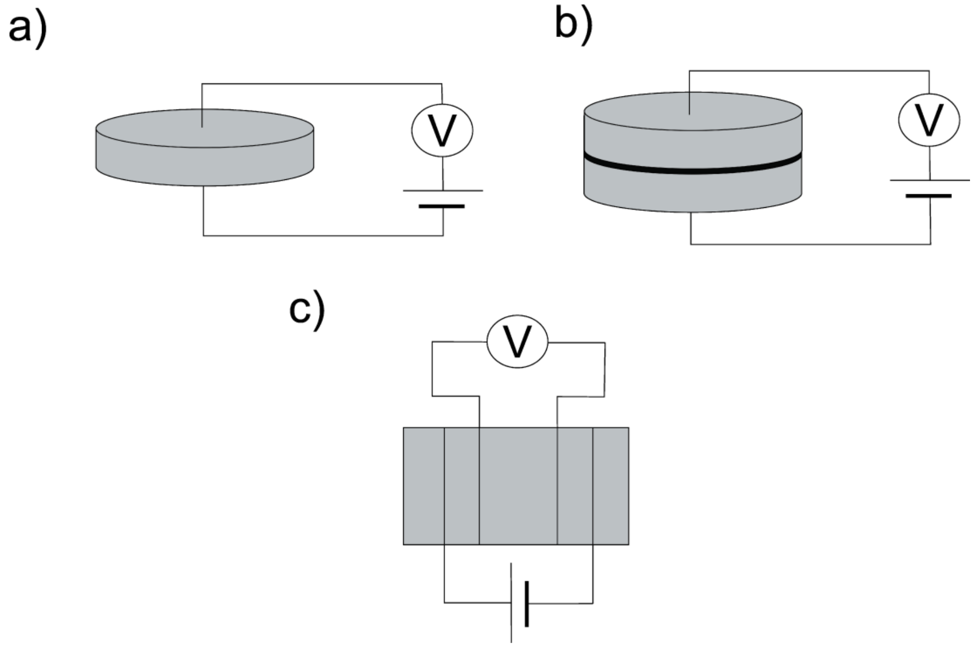

Figure 3.1: Experimental setups for sensor and conductivity tests showing the 2-point (a.b) and 4-point (c) methods used. The power supply provided a constant current of 100 mA.

To determine the contributions of ionic and electronic conductivity to the total conductivity, an Al blocking electrode was used. The Al electrode blocks the flow of O_2^{2-}

species, therefore $\sigma = \sigma_E$. The ionic conductivity was inferred from the difference between σ_T and σ_E. To measure σ_E, two pellets of $Ba_{1-x}Ce_xFeO_{3-\delta}$ (x = 0, 0.05) were made as previously described and a thin film of Aluminum was added between pellets. The "sandwiched" pellets were heated to 660°C for 4 h with ramp rates of 2°C/min to soften the aluminum and minimize contact resistance. Platinum mesh was added as a current collector on each side of the combined pellets and electronic conductivity measurements were recorded at temperatures 25-1000°C in air. A schematic view of the different conductivity setups is shown in Figure 3.1. To ensure reproducibility, multiple trials of each measurement (with and without blocking electrodes) were performed under both heating and cooling cycles. The 2-point conductivity measurements were repeated 3 to 6 times for the various samples yielding errors between 2 and 11%, shown with the appropriate error bars in the relevant figures.

3.2.4 Sensor Experiments

Sensor experiments were performed by 4 point conductivity measurements in various atmospheres. To form the sensor, 4 grams of $Ba_{0.95}Ce_{.05}FeO_{3-\delta}$ powder was uniaxially pressed at 15000 lbs to form a circular pellet which was subsequently sintered at 1200°C for 4 h with heating/cooling ramp rates of 2°C/min. The pellet was cut into a rectangular shape with dimensions 12 × 6 × 1 mm and electrical contacts were made by wrapping 4 platinum wires around the sensor. Platinum paste was applied to ensure electrode contact and the organic binder was removed by heating to 800°C for 1h. The sensor was contained in a hollow quartz tube sealed on each end by rubber septa and heated to the desired temperature using a tube furnace. Mass flow controllers (MFC) allowed for the mixing of gases to create the desired atmosphere that is then flowed through the quartz tube and over the sensor [23]. Figure 3.1c shows the 4 point measurement used for conductivity where the two exterior contacts supplied DC current (100 mA) and the inner two electrodes monitored voltage drop with a digital multimeter. The response of each sensor was calculated according to Equation 3.1. Here, the sensor response, S, is defined as the ratio of the relative conductivity change and allows for the comparison of sensors in various atmospheres.

$$S = 100\% \times \left(\frac{\sigma_{gas} - \sigma_{air}}{\sigma_{air}}\right) \tag{3.1}$$

The conductivity of the material was recorded at 1 minute intervals and the flow of test gas through the test chamber was varied from 2.5-15 sccm with a balance of air so that the total gas flow rate was 50 sccm.

3.3 Results and Discussion

3.3.1 Characterization

The effect of Cerium doping on surface morphology was investigated with scanning electron microscopy (SEM). Figure 3.2 a,b shows low magnification images of un-doped $BaFeO_{3-\delta}$ and $Ba_{0.95}Ce_{0.05}FeO_{3-\delta}$ respectively. Both samples have an inhomogeneous dispersion of particle sizes, ranging from less than 500 nm to over 1 μm. Higher magnification imaging reveals a similar trend in grain boundary sizes (Figure 3.2 c,d). Similar particle and grain sizes for doped and undoped materials indicate that Ce doping has little effect on morphology, however the $BaFeO_{3-\delta}$ sample shows signs of phase separation. Higher magnification imaging of $BaFeO_{3-\delta}$ (Figure 3.2 c) depicts a uniform particle coated in a porous, powder-like material. This could be indicative of a second phase present in the un-doped sample as is visible through further characterization with x-ray diffraction.

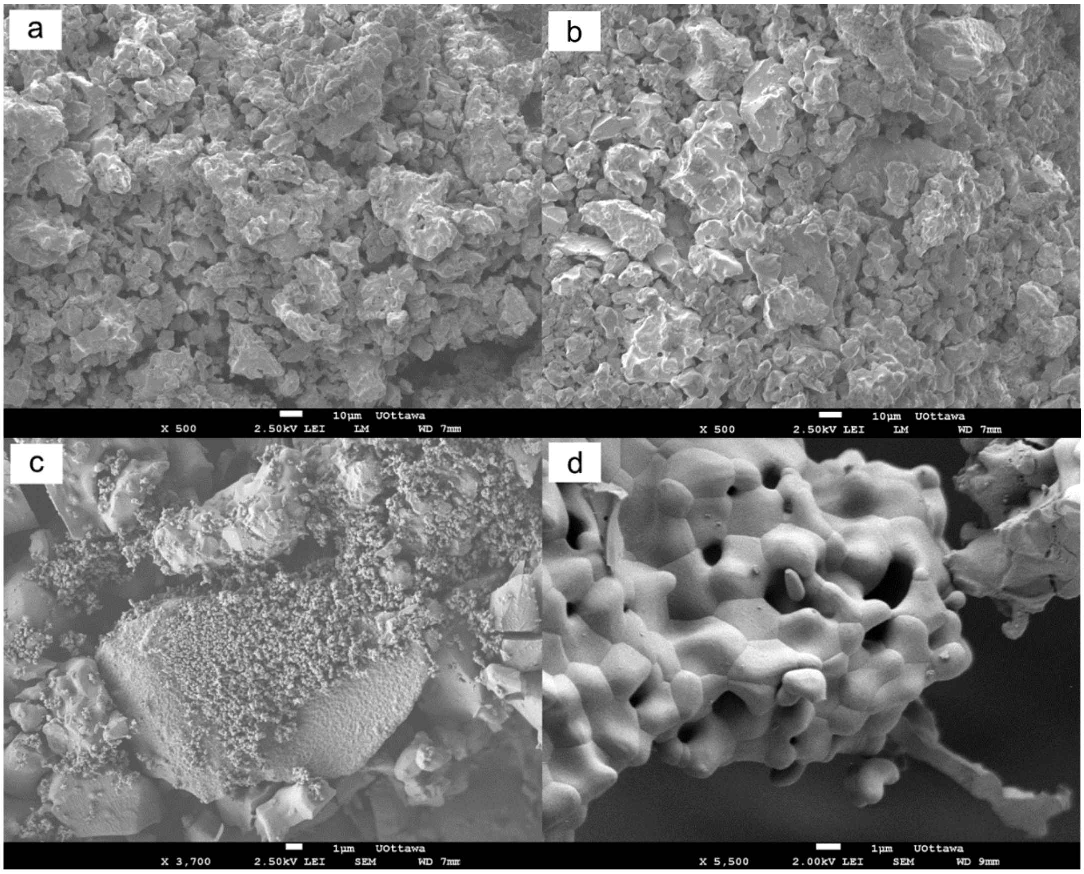

Figure 3.2: SEM images of $BaFeO_{3-\delta}$ (a,c) and $Ba_{0.95}Ce_{0.05}FeO_{3-\delta}$ (b,d) as-prepared powders.

X-Ray diffraction was used to determine the phase composition of the Ce doped perovskites. Figure 3.3 shows the p-XRD spectra for the calcined powders of $Ba_{1-x}Ce_xFeO_{3-\delta}$ (x=0, 0.01, 0.03, 0.05). Spectra are in order of decreasing Cerium content: x = 0.05, 0.03, 0.01, and 0 corresponding to a, b, c, and d, respectively. The spectrum for $BaFeO_{3-\delta}$ (Figure 3.3 d) shows a combination of phases resulting from the varying degrees of oxygen vacancies present. This is a result of the preparation method, namely high temperature calcination in air. The synthesis of stoichiometric $BaFeO_3$ has been reported by further treatment in pressurized O_2 environments and heating in ozone [21]. The prominent phase can be indexed to $BaFeO_{3-\delta}$ (PDF: 00-023-1024) in a hexagonal structure with lattice constants *a,b* = 5.66 and *c* = 13.83. Other less prominent phases are visible including a cubic $BaFeO_{3-\delta}$. The multiple phases visible are consistent with SEM imaging. Doping the material with Ce (Figure 3.3 a,b,c) leads to a structural shift from hexagonal to cubic. The $Ba_{0.95}Ce_{0.05}FeO_{3-\delta}$ sample (Figure 3.3 a) shows the cleanest spectrum with a prominent phase that fits to a cubic perovskite (*Pm*-3*m* space group) with lattice constants a = b = c = 4.035 Å. Rietveld refinement of the powder spectra, along with calculations of the Goldschmidt tolerance factors, conclude that Ce replaces Ba at the A site in the perovskite structure. Cerium doping has shifted the material from a hexagonal structure to a cubic perovskite.

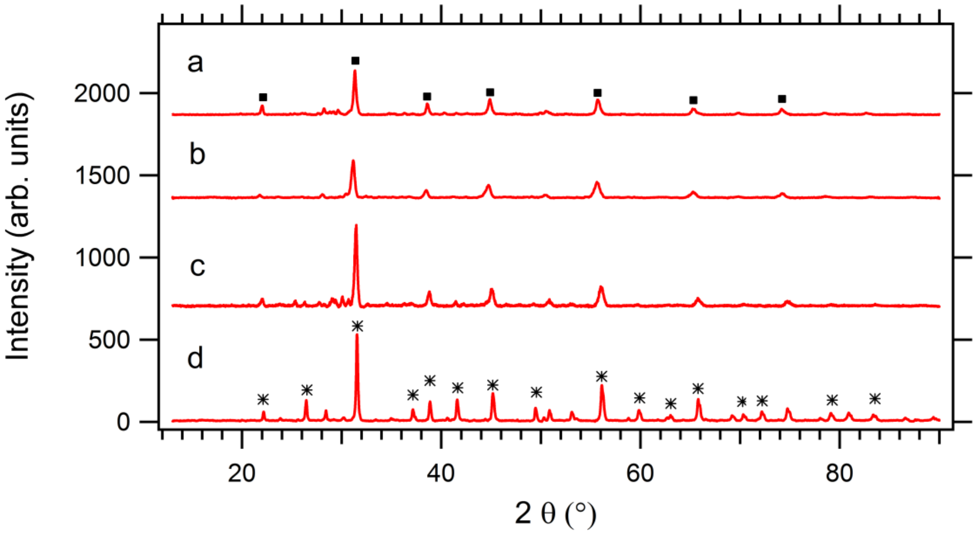

Figure 3.3: p-XRD of $Ba_{1-x}Ce_xFeO_{3-\delta}$ x = 0-0.05. Spectra are in order of decreasing Cerium content: x = 0.05, 0.03, 0.01, and 0 corresponding to a, b, c, and d respectively. Phase labels: hexagonal = asterisk, cubic = square.

3.3.2 Conductivity Properties

The total conductivity of each sample was measured in various atmospheres and at temperature intervals from 25-1000°C. Both $BaFeO_{3-\delta}$ and $Ba_{0.95}Ce_{0.05}FeO_{3-\delta}$ show p-type semiconductor behavior namely higher conductivities in oxidizing than reducing atmospheres.

Tests under a reducing atmosphere (5% H_2 in N_2, 500°C) led to decomposition of the perovskite phase and the formation of several phases, including Fe^0. This indicates that these materials are unstable in reducing atmospheres at elevated temperatures. Similar tests performed under air and O_2 indicate complete stability of these materials in oxidizing atmospheres up to 1200°C. The total conductivities in air from 25-1000°C are shown in Figure 3.4 with the appropriate error bars at each temperature. Cerium doping increased the conductivity of the perovskite throughout the entire temperature range with a more pronounced effect at higher temperatures. At 800°C the conductivity of $Ba_{0.95}Ce_{0.05}FeO_{3-\delta}$ reaches 3.3 S/cm. This value falls well in the range of other perovskites containing Ba and Fe [24,25]. Figure 3.4.b shows an Arrhenius type plot of the conductivity values between 600-1000°C and the calculated activation energies. Both samples exhibit similar changes in conductivity with respect to temperature including a dramatic increase in ionic conductivity at 800°C. This is indicative of a change in the dominant conduction type. Both samples are p-type semiconductors where the prominent charge carriers are electron holes [2]. As is shown in Equation 3.2, the replacement of Ba^{+2} with Ce^{+3} at the A site in the perovskite structure decreases the number of oxygen vacancies and increases the number of electron holes. The greater number of electron holes leads to an increased conductivity for the Cerium doped material.

$$Ce^{+3} + \frac{1}{2}O_2 + V_o^{\bullet\bullet} \longrightarrow Ce_{Ba}^{\bullet} + O_o^{x} + h^{\bullet} \qquad [3.2]$$

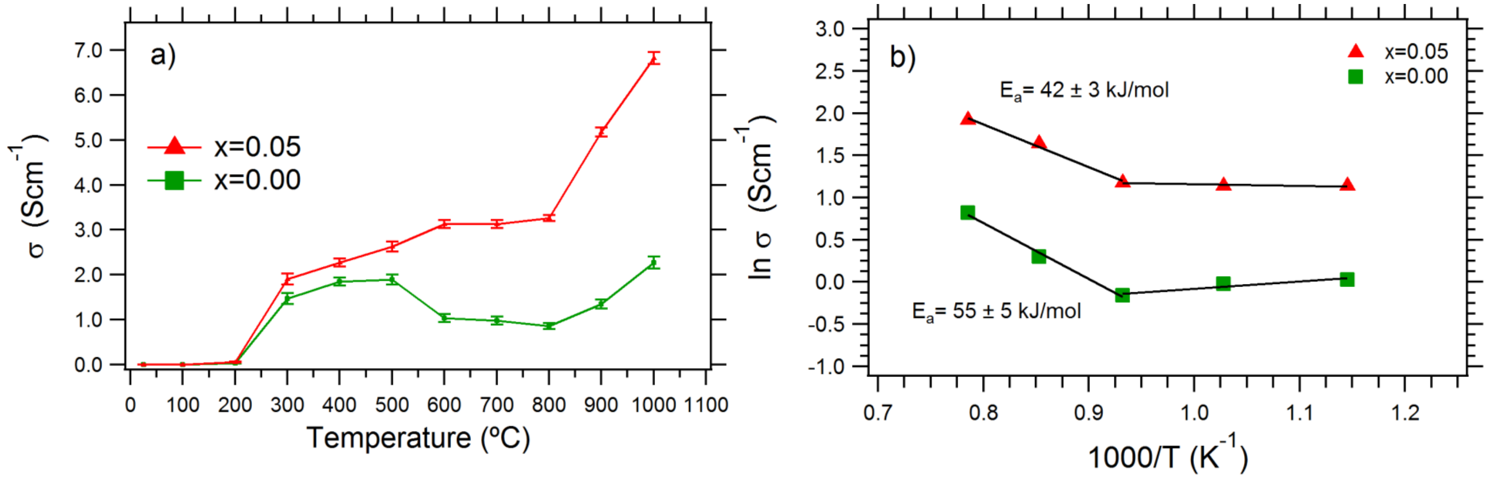

Figure 3.4: a) Conductivity of $Ba_{1-x}Ce_xFeO_{3-\delta}$ (x=0, 0.05) between 25-1000˚C. b) Arrhenius plot of conductivities between 600-1000˚C (activation energies calculated between 800-1000°C)

The Barium ferrite perovskite family was expected to be capable of ionic as well as electronic conduction. It is therefore of interest to determine the individual contributions of ionic (σ_I) and electronic conductivity (σ_E) to the total conductivity (σ_T) of the material. To measure the electronic conductivity exclusively, an Al electrode was used as an ionic blocker. This forms a gradient of oxygen anions on either side of the Al electrode through which only electronic current can flow. Here it is assumed that $\sigma_T = \sigma_E + \sigma_I$ therefore subtracting the electronic conductivity from the total conductivity gives an estimate of the ionic conductivity. The electronic conductivities of $BaFeO_{3-\delta}$ and $Ba_{0.95}Ce_{0.05}FeO_{3-\delta}$ were measured in the temperature range of 25-1000˚C (shown in Figure 3.5.a with the appropriate error bars as measured) and were subtracted from the bulk values to give the ionic conductivities (Figure 3.5.b). Both $BaFeO_{3-\delta}$ and $Ba_{0.95}Ce_{0.05}FeO_{3-\delta}$ are largely ionic conductors throughout the temperature range. The addition of 5% Ce increased the electronic conductivity by an order of magnitude, from 0.04 to 0.56 S/cm at 800˚C. The ionic conductivity for doped and un-doped $BaFeO_{3-\delta}$ increases in a similar manner until 600˚C at which point the value for $Ba_{0.95}Ce_{0.05}FeO_{3-\delta}$ increases whereas $BaFeO_{3-\delta}$ decreases. This indicates that 5% Ce doping has increased both σ_E and σ_I. Previous work has attributed the increased resistance of $BaFeO_{3-\delta}$ above 200 K to the Verwey transition (ferromagnetic to antiferromagnetic transition) [21,26]. However, this explanation has been debated and is beyond the scope of this work.

3.3.3 Gas Sensing Properties

The $Ba_{0.95}Ce_{0.05}FeO_{3-\delta}$ perovskite has shown relatively high ionic conductivity and is therefore of interest as a gas sensor, in this case for the detection of oxidizing gases. Semiconducting gas sensors must have a porous microstructure with high surface area in order to maximize response[27]. The measured response, conductivity in this case, is directly related to grain size and separation. Here, sensor experiments were carried out as 4 point conductivity measurements on a sintered pellet of $Ba_{0.95}Ce_{0.05}FeO_{3-\delta}$. The surface morphology of the sensor was imaged with SEM (Figure 3.6). The sensor has a porous microstructure with well defined grain boundaries and surface structures are apparent with sizes in the 100 nm range.

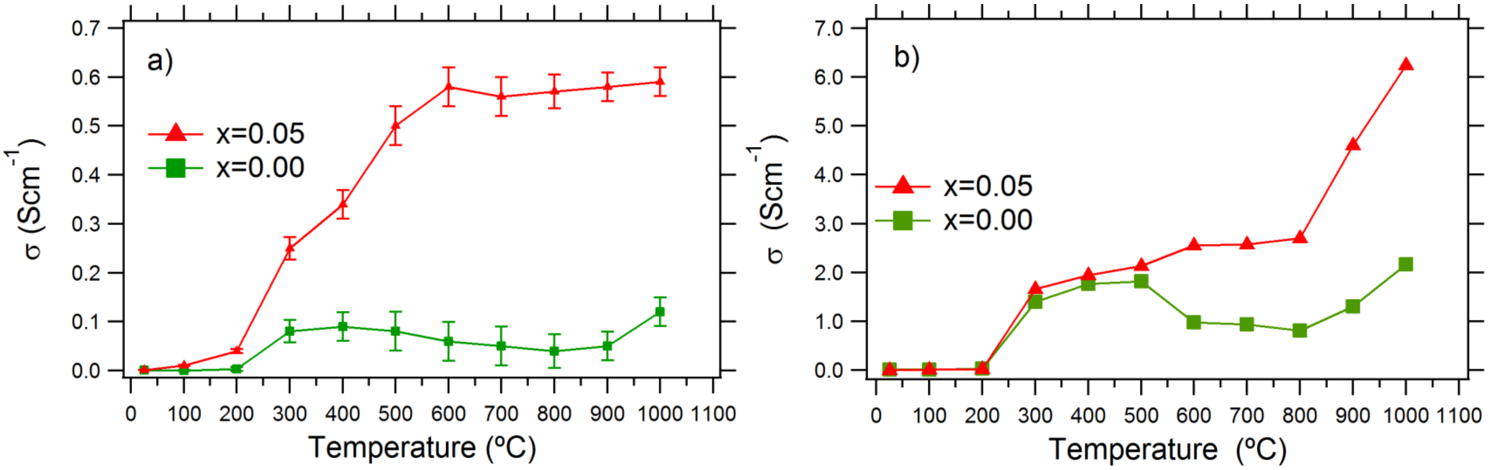

Figure 3.5: a) Electronic and **b)** Ionic conductivities of $Ba_{1-x}Ce_xFeO_{3-\delta}$ (x=0, 0.05).

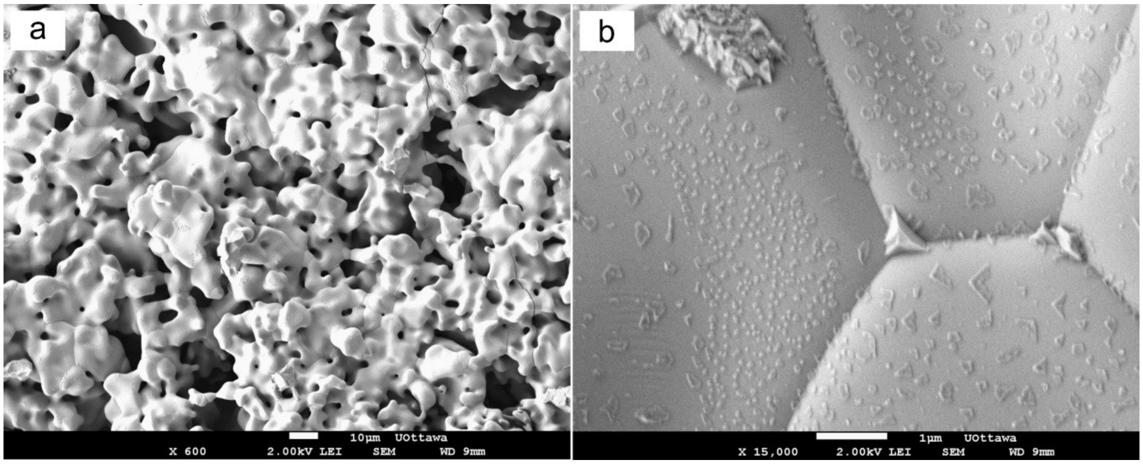

Figure 3.6: Low (a) and high (b) magnification SEM images of $Ba_{0.95}Ce_{0.05}FeO_{3-\delta}$ sensor.

The sensor signal toward O_2 was tested at 500˚C and 700˚C with a carrier gas of air. The operating temperatures were chosen based on the conductivity measurements previously discussed. A solid state sensor should aim to maximize sensor response at reduced temperatures. The $Ba_{0.95}Ce_{0.05}FeO_{3-\delta}$ material exhibited a sharp increase in conductivity under oxidizing atmospheres above 500°C, therefore temperatures of 500°C and higher should result in a greater sensor response. The sensor maintained a baseline conductivity in air and a range of O_2 concentrations were introduced through the test chamber to determine sensor response. The concentration of O_2 through the test chamber is calculated from a base of compressed air containing 20.95% O_2 by volume. The sensor response to a range of O_2 concentrations (25-45%) is shown in Figure 3.7. The sensor shows a completely reversible response to O_2 at both 500˚C and 700˚C. The time required for the sensor to achieve 99% of the stable response values (response time) and for it to recover its original conductivity upon removal of the target gas (recovery time) is an important measure in the design of sensors. Response and recovery times for the $Ba_{0.95}Ce_{0.05}FeO_{3-\delta}$ sensor are listed in Table 3.1. The sensor response to O_2 increases with temperature as expected and the response and recovery times at 700˚C are greater than those at 500˚C. At 500°C it is assumed that the sensor response is dependent upon adsorbed oxygen species on the material surface [28,29]. This temperature is a typical switchover point below which not only the cations, but also the oxygen non-stoichiometry can be considered to be frozen and therefore the sensing mechanism is dominated by surface effects [30–33]. As previously mentioned, the dominant charge carriers for p-type semiconductors are electron holes. Increasing the concentration of O_2 leads to a more oxidative atmosphere where electrons are more readily removed from the conduction band. This increases the number of electron holes and in turn the conductivity. This is shown in Equation 3.3.

$$O_{ads} + 2e^{-} \rightarrow O^{2-} + 2\dot{\dot{h}} \qquad [3.3]$$

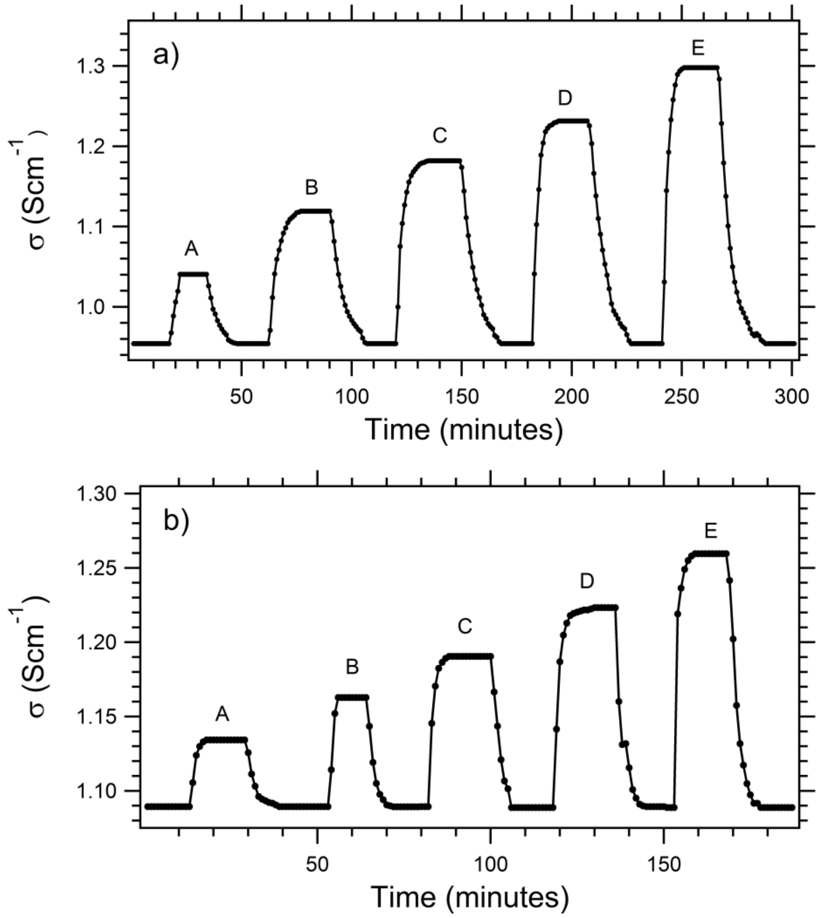

Figure 3.7: Sensor conductivity in O_2 at temperatures of a) 700˚C and b) 500˚C. Features are labelled by their O_2 concentration: 25, 29, 33, 37 and 45 % O_2 for A, B, C, D and E, respectively.

Table 3.1: Response and recovery times for $Ba_{0.95}Ce_{0.05}FeO_{3-\delta}$ O_2 sensor at 500˚C and 700˚C.

		Response Time (min)		Recovery Time (min)	
Peak	Oxygen Content %	T= 500°C	T = 700°C	T = 500°C	T = 700°C
A	25	6	9	10	14
B	29	4	17	8	19
C	33	7	17	7	21
D	37	10	14	9	23
E	45	8	10	12	22

At temperatures higher than 500°C it is known that oxygen equilibration within the p-type ferrites occurs rapidly [12,28,34]. Therefore at 700°C it is assumed that sensor response is dependent on bulk transport of oxygen into the perovskite. This sensing mechanism also decreases the number of oxygen vacancies in the material and increases the conductivity. Here it is useful to compare the values of S as plotted in Figure 3.8. It is important to note that because these measurements were performed with a 4-point setup, the error bars are smaller than the symbols in the figure. At 500°C, the sensor shows a linear response to O_2 concentration until approximately 40% O_2. Beyond this concentration a deviation from linearity is observed. At 700°C the sensor has a greater response due to bulk oxygen equilibration, however the saturation effect is more pronounced.

Whereas at low temperatures the surface and bulk of the perovskite may not be in equilibrium, at higher temperatures equilibration results in a change in the number of oxygen vacancies concurrent with the reduction of Fe from +4 to +3. The fast equilibration observed in ferrites is partly due to the affinity of Fe ions to achieve the +3 state [14,16,34]. The equilibrated perovskite stoichiometry for the undoped material can then be written as $BaFe^{+4}_{1-x}Fe^{+3}_{x}O_{3-x/2}$ [32]. The difference in conductivity modes at low vs. high temperature results in different sensitivity of the sensors under each condition as can be derived from Figures 3.7 and 3.8. One would expect this dependency to decrease significantly in the higher temperature region (T > 500°C) where bulk equilibration dominates the sensing mechanism [35]. Figure 3.9 shows a plot of $\log(\sigma)$ vs $\log(pO_2)$ for the BCF sensor at 500 and 700°C. The slope, M, is a measurement of sensitivity for the material at each temperature. Although the pO_2 range is limited, the 5% Ce doped material shows an extremely high sensitivity of M=0.38 at T=700°C. The high pO_2 sensitivity and low E_a for conductivity are promising attributes [33]. These materials may demonstrate temperature independent O_2 response at elevated temperatures in the bulk equilibration range.

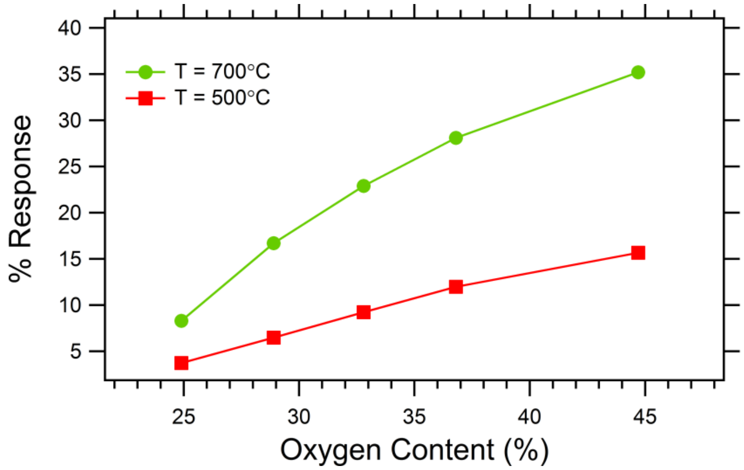

Figure 3.8: Sensor Response vs. O_2 concentration for $Ba_{0.95}Ce_{0.05}FeO_{3-\delta}$ sensor at 500˚C and 700˚C.

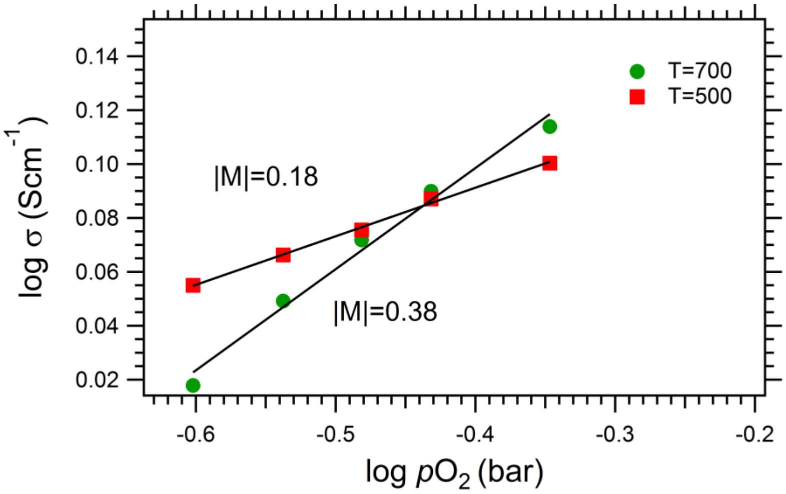

Figure 3.9: log(σ) vs log(pO_2) plot for $Ba_{0.95}Ce_{0.05}FeO_{3-\delta}$ sensor at 500 and 700°C.

3.4 Conclusion

The $Ba_{1-x}Ce_xFeO_{3-\delta}$ (x=0, 0.01, 0.03, and 0.05) perovskite family was prepared via a sol-gel method. Ce doping at the A site leads to a structural shift from hexagonal to a cubic perovskite. The incorporation of Ce substantially increases the electronic and ionic conductivity of these materials, making the perovskites suitable as electrochemical gas sensors. A $Ba_{0.95}Ce_{0.05}FeO_{3-\delta}$ solid state gas sensor exhibited a completely reproducible response to O_2 at 500 and 700°C. The sensing mechanism is consistent with a surface process at 500°C and a bulk process at 700°C.

3.5 References

[1] Y. Niu, W. Zhou, J. Sunarso, F. Liang, Z. Zhu, Z. Shao, A single-step synthesized cobalt-free barium ferrites-based composite cathode for intermediate temperature solid oxide fuel cells, Electrochemistry Communications. 13 (2011) 1340–1343.

[2] S.P. Jiang, L. Liu, K.P. Ong, P. Wu, J. Li, J. Pu, Electrical conductivity and performance of doped LaCrO3 perovskite oxides for solid oxide fuel cells, Journal of Power Sources. 176 (2008) 82–89.

[3] Y. Itagaki, M. Mori, Y. Hosoya, H. Aono, Y. Sadaoka, O3 and NO2 sensing properties of SmFe1−xCoxO3 perovskite oxides, Sensors and Actuators B: Chemical. 122 (2007) 315–320.

[4] S.M. Bukhari, J.B. Giorgi, Chemically stable and coke resistant Sm1−xCexFeO3−δ perovskites for low temperature solid oxide fuel cell anode applications, Journal of Power Sources. 198 (2012) 51–58.

[5] J. Matsuno, T. Mizokawa, a. Fujimori, Y. Takeda, S. Kawasaki, M. Takano, Different routes to charge disproportionation in perovskite-type Fe oxides, Physical Review B. 66 (2002) 1–4.

[6] D. Rembelski, J.P. Viricelle, L. Combemale, M. Rieu, Characterization and Comparison of Different Cathode Materials for SC-SOFC: LSM, BSCF, SSC, and LSCF, Fuel Cells. 12 (2012) 256–264.

[7] H. Aono, E. Traversa, M. Sakamoto, Y. Sadaoka, Crystallographic characterization and NO2 gas sensing property of LnFeO3 prepared by thermal decomposition of LnFe hexacyanocomplexes, Ln[Fe(CN)6]·nH2O, Ln = La, Nd, Sm, Gd, and Dy, Sensors and Actuators B: Chemical. 94 (2003) 132–139.

[8] K.H. Friese, F. Stanglmeier, H.M. Wiedenmann, Electrochemical sensor to determine the oxygen concentration in gas mixtures, U.S. Patent WO 95/25276, 1995.

[9] N. Izu, W. Shin, I. Matsubara, N. Murayama, The effects of the particle size and crystallite size on the response time for resistive oxygen gas sensor using cerium oxide thick film, Sensors and Actuators B: Chemical. 94 (2003) 222–227.

[10] A. Takami, Development of titania heated exhaust-gas oxygen sensor, Ceramic Bulletin. (1988) 1956–1960.

[11] R. Moos, W. Menesklou, K.H. Hardtl, Materials for temperature independent resistive oxygen sensors for combustion exhaust gas control, Sensors and Actuators B: Chemical. (2000) 178–183.

[12] K. Sahner, R. Moos, N. Izu, W. Shin, N. Murayama, Response kinetics of temperature-independent resistive oxygen sensor formulations: a comparative study, Sensors and Actuators B: Chemical. 113 (2006) 112–119.

[13] P.T. Moseley, D.E. Williams, Gas sensors based on oxides of early transition metals, Polyhedron. 8 (1989) 1615–1618.

[14] M.L. Post, B.W. Sanders, P. Kennepohl, Thin films of non-stoichiometric perovskites as potential oxygen sensors, Sensors and Actuators B: Chemical. 14 (1993) 13–14.

[15] D. Wang, J.J. Tunney, X. Du, M.L. Post, R. Gauvin, Thermal stability of SrFeO3/Al2O3 thin films: Transmission electron microscopy study and conductometric sensing response, Journal of Applied Physics. 104 (2008) 023530.

[16] J.J. Tunney, M.L. Post, The Electrical Conductance of SrFeO2.5+x Thin Films, Journal of Electroceramics 5:1. (2000) 63–69.

[17] S.M. Bukhari, J.B. Giorgi, Redox Stability of Sm0.95Ce0.05Fe1-xCrxO3-δ Perovskite Materials, Journal of The Electrochemical Society. 158 (2011) H1027.

[18] S.M. Bukhari, J.B. Giorgi, Surface and redox chemistry of Sm0.95Ce0.05Fe1−xNixO3−δ perovskites, Solid State Ionics. 194 (2011) 33–40.

[19] S.M. Bukhari, J.B. Giorgi, Tuneability of Sm(1−x)CexFeO3±λ perovskites: Thermal stability and electrical conductivity, Solid State Ionics. 180 (2009) 198–204.

[20] J.B. MacChesney, J.F. Potter, R.C. Sherwood, H.J. Williams, Oxygen Stoichiometry in the Barium Ferrates; Its Effect on Magnetization and Resistivity, The Journal of Chemical Physics. 43 (1965) 3317.

[21] N. Hayashi, T. Yamamoto, H. Kageyama, M. Nishi, Y. Watanabe, T. Kawakami, et al., BaFeO3: a ferromagnetic iron oxide., Angewandte Chemie (International Ed. in English). 50 (2011) 12547–50.

[22] T. Takeda, R. Kanno, Y. Kawamoto, M. Takano, Metal – semiconductor transition, charge disproportionation, and low-temperature structure of Ca1–xSrxFeO3 synthesized under high-oxygen pressure, Solid State Sciences. 2 (2000) 673–687.

[23] S.M. Bukhari, J.B. Giorgi, Cobalt Doped Sm0.95Ce0.05FeO3-δ for Detection of Reducing Gases, Journal of The Electrochemical Society. 158 (2011) J159.

[24] H. Choi, A. Fuller, J. Davis, C. Wielgus, U.S. Ozkan, Ce-doped strontium cobalt ferrite perovskites as cathode catalysts for solid oxide fuel cells: Effect of dopant concentration, Applied Catalysis B: Environmental. 127 (2012) 336–341.

[25] A.K. Azad, A. Khan, S.-G. Eriksson, J.T.S. Irvine, Synthesis, structure and magnetic properties of Sr2Fe1−xGaxMoO6 (0≤x≤0.6) double perovskites, Materials Research Bulletin. 44 (2009) 2181–2185.

[26] H. Kronmuller, F. Walz, J. Rivas, D. Martinez, Influence of Ba Content on the Magnetic After-Effect Spectra in Barium Ferrites, Physica Status Solidi (A). 137 (1994) 137–148.

[27] N. Barsan, D. Koziej, U. Weimar, Metal oxide-based gas sensor research: How to?, Sensors and Actuators B: Chemical. 121 (2007) 18–35.

[28] W. Gopel, New materials and transducers for chemical sensors, Sensors and Actuators B: Chemical. 19 (1994) 1–21.

[29] H. Iwahara, Ionic Conduction in Perovskite-Type Compounds, in: T. Ishihara (Ed.), Perovskite Oxide for Solid Oxide Fuel Cells, Springer US, Boston, MA, 2009: pp. 45–63.

[30] R. Moos, K.H. Hardtl, Defect Chemistry of Donor-Doped and Undoped Strontium Titanate Ceramics between 1000° and 1400°C, Journal of the American Ceramic Society. 10 (1997) 2549–2562.

[31] B. Boukamp, M. Pham, D. Blank, H. Bouwmeester, Ionic and electronic conductivity in lead–zirconate–titanate (PZT), Solid State Ionics. 170 (2004) 239–254.

[32] A. Rothschild, W. Menesklou, H.L. Tuller, E. Ivers-tiffe, Electronic Structure, Defect Chemistry, and Transport Properties of SrTi1-xFexO3-y Solid Solutions, Chemistry of Materials. (2006) 3651–3659.

[33] P.T. Moseley, Materials selection for semiconductor gas sensors, Sensors and Actuators B: Chemical. 6 (1992) 149–156.

[34] J.J. Tunney, M.L. Post, X. Du, D. Yang, Temperature Dependence and Gas-Sensing Response of Conduction for Mixed Conducting SrFeyCozOx Thin Films, Journal of The Electrochemical Society. 149 (2002) H113.

[35] R. Moos, N. Izu, F. Rettig, S. Reiss, W. Shin, I. Matsubara, Resistive oxygen gas sensors for harsh environments., Sensors (Basel, Switzerland). 11 (2011) 3439–65.

Chapter 4

Enhanced Performance of Transition Metal Doped $Sm_{0.95}Ce_{0.05}FeO_{3-\delta}$ SOFC Anodes in H_2S

Contributions from this chapter have been published in:
S.M. Bukhari, W.D. Penwell, J.B. Giorgi, ECS Trans. 57 (2013) 1507.

Abstract

Promising perovskite anodes have been tested in high sulfur fuel feeds. A series of perovskite solid oxide fuel cell (SOFC) anode materials: $Sm_{0.95}Ce_{0.05}FeO_{3-\delta}$, $Sm_{0.95}Ce_{0.05}Fe_{0.97}Ni_{0.03}O_{3-\delta}$ and $Sm_{0.95}Ce_{0.05}Fe_{0.97}Co_{0.03}O_{3-\delta}$ have been tested for sulfur tolerance at 500°C. The introduction of the extreme 5% H_2S enhances the performance of these anodes, verified by EIS and CA experiments. Post mortem analyses indicate that the performance enhancement arises from the partial sulfidation of the anode, leading to the formation of FeS_2, Sm_3S_4 and S on the perovskite surface. Testing in lower concentrations of sulfur, more common in sour fuels, 0.5% H_2S, also enhances the performance of these materials. The SCF-Co anode shows promising stability and an increase in exchange current density, i_o, from 13.72 to 127.02 mA/cm^2 when switching from H_2 to 0.5% H_2S/99.5% H_2 fuel composition. Recovery tests performed on the SCF-Co anode conclude that the open cell voltage (OCV) and power density of these cells recover within 4 hours of H_2S removal. We conclude that the formation of metal sulfide species is only partially reversible, yielding an anode material with an overall lower R_{ct} upon switching back to pure H_2. Combining their performance in sulfur containing fuels with their previously reported coke tolerance makes these perovskites especially attractive as low temperature SOFC anodes in sour fuels.

4.1 Introduction

Solid oxide fuel cells (SOFCs) are an attractive power source technology since they offer the ability to directly convert chemical energy to electricity with low emissions and high efficiency [1–3]. The commercial viability of SOFCs is currently limited by several factors, mainly their high operating temperatures and material instability in carbon and sulfur containing fuels. Ni-YSZ, the current state of the art SOFC anode material, performs well in H_2 but suffers from severe coke and sulfur poisoning when exposed to carbon and sulfur containing fuels [4,5]. Therefore, an active area of research focuses on the development of new, fuel flexible anode materials for low temperature SOFCs (LT-SOFC). A suitable anode material for fuel flexible LT-SOFC applications should be tolerant to CH_4 and H_2S, components of the current natural gas sources [4,6].

Perovskites of the type ABO_3 have unique structural and electronic properties making them suitable for SOFCs. In the perovskite structure, A and B are cations (typically alkali earth, rare earth, and transition metals) that can be tailored to suit the material needs. Many perovskites demonstrate excellent properties as cathode materials for SOFCs and several have promising anode performance in sulfur and carbon containing fuels [2,7]. Doped perovskite systems such as LSV (lanthanum strontium vanadate) have shown tolerance to both CH_4 and H_2 fuels containing up to 5% H_2S, although these studies were performed at high temperatures [8,9]. The development of coke and sulfur tolerant perovskite materials for LT-SOFC applications remains an area of high interest.

Recent work in our group has focused on the doping of $SmFeO_3$, leading to the development of LT-SOFC anode materials and gas sensors [10–14]. Specifically, A site Ce doping and B site transition metal doping makes these materials suitable as coke tolerant anodes for CH_4 fueled LT-SOFCs [13]. Although the performance of these anode materials in H_2 has been studied in depth, no work has been done on their tolerance to sulfur containing fuels.

The current study evaluates the sulfur tolerance of three recently developed and carbon tolerant anode materials, $Sm_{0.95}Ce_{0.05}FeO_{3-\delta}$, $Sm_{0.95}Ce_{0.05}Fe_{0.97}Ni_{0.03}O_{3-\delta}$ and $Sm_{0.95}Ce_{0.05}Fe_{0.97}Co_{0.03}O_{3-\delta}$. In depth electrochemical testing and post mortem analyses are performed to determine the effect of H_2S on anode performance and microstructure.

4.2 Experimental

4.2.1 Powder Synthesis

Perovskite powders with formulae $Sm_{0.95}Ce_{0.05}FeO_{3-\delta}$, $Sm_{0.95}Ce_{0.05}Fe_{0.97}Ni_{0.03}O_{3-\delta}$ and $Sm_{0.95}Ce_{0.05}Fe_{0.97}Co_{0.03}O_{3-\delta}$ were prepared by decomposition of citrate precursors via a sol-gel method. The preparation and characterization of these perovskites has been previously reported [10–16]. Starting materials included samarium nitrate $Sm(NO_3)_3{\cdot}6H_2O$, AlfaAesar, 99.9%), cerium nitrate hexahydrate ($Ce(NO_3)_3{\cdot}6H_2O$, AlfaAesar, 99.5%), iron nitrate nonahydrate ($Fe(NO_3)_3{\cdot}9H_2O$, AlfaAesar, >98%), cobalt nitrate hexahydrate ($Co(NO_3)_2{\cdot}6H_2O$, AlfaAesar, 99%), nickel nitrate hexahydrate ($Co(NO_3)_2{\cdot}6H_2O$, AlfaAesar, 99%) and citric acid monohydrate (AlfaAesar, minimum 99%). The nitrates were weighed according to the desired stoichiometry and dissolved separately in de-ionized water. The metal nitrate solutions were combined and added to aqueous citric acid so that the ratio of citric acid to total metal ion was 1:1. The solution was dried at 120°C for 24 hours resulting in a citrate gel precursor that was subsequently ground and calcined at 850°C for 24 hours using heating/cooling ramp rates of 5°C/min. For the remainder of the manuscript the perovskite materials $Sm_{0.95}Ce_{0.05}FeO_{3-\delta}$,

$Sm_{0.95}Ce_{0.05}Fe_{0.97}Ni_{0.03}O_{3-\delta}$ and $Sm_{0.95}Ce_{0.05}Fe_{0.97}Co_{0.03}O_{3-\delta}$ will be abbreviated as SCF, SCF-Ni and SCF-Co respectively.

4.2.2 Characterization

Powder X-Ray Diffraction (XRD, Philips PW 1830) was used to determine the phase composition of the perovskite powders before and after fuel cell testing. The instrument used CuK_α radiation (λ=1.54 Å) and the scattering angle, 2θ, was scanned between 13-90° at a rate of 0.02°/s. Panalytical X'PertHighscore Plus software was used for profile refinement and phases were indexed to the ICDD Powder Diffraction File database (PDF-4+, 2012).

Scanning electron microscopy (SEM, JEOL JSM-7500F) was used to image the perovskite anodes before and after testing. Elemental composition of the materials was determined with an energy dispersive x-ray spectroscopy (EDS X-Sight) attachment.

4.2.3 Button Cell Fabrication

Electrolyte supported cells were assembled following a general procedure used in our group [10,17]. To form the electrolyte, 2 grams of 20% samarium doped ceria (SDC-20, FuelCellMaterials.com) was uni-axially pressed in a 12 mm die to 15000 lbs for 2 minutes. The pellets were sintered at 1400°C for 4 hrs using heating/cooling ramp rates of 2°C/min yielding an electrolyte thickness of ~2 mm. To prepare the anode, a slurry was made consisting of the perovskite powder in an emulsion (20% Triton-X100 / 80% H_2O v/v). The slurry was painted on one side of the electrolyte disc and fired at 1400°C for 4 hours. A platinum mesh current collector (AlfaAesar, 99.9%) was embedded with additional anode slurry and fired again at 1400°C for 4 hours. The cathode consisted of 50% w/w LSCF (FuelCellMaterials.com)/SDC-20 with a Pt mesh current collector and was prepared in the same manner as the anode. The effective electrode areas were 1.5 cm^2. The reference electrode in this setup was a Pt wire wrapped horizontally around the electrolyte and coated in Pt paste that was subsequently heated to 800°C for 2 hrs to remove the organic binder.

4.2.4 Fuel Cell Setup and Electrochemical Tests

The fuel cell setup used has been previously described [14,18]. The apparatus consists of an alumina support tube attached to a custom made Ultra-Torr fitting with a Viton O-ring seal. The Ultra-Torr fitting is attached to a three-way Swagelok gas manifold for fuel mixing. The button cell sits atop the alumina support, inside of which a smaller diameter alumina tube carries fuel gas to the anode. The cell is sealed to the alumina support using a Pyrex ring. A short alumina tube placed on top of the cell provides weight to facilitate sealing of the Pyrex. The cathode side of the cell is open to air. This entire setup is placed inside a vertical tube furnace controlled by a Barber-Colman temperature controller using a K-type thermocouple. Three lengths of Pt wire served as the electrode leads. Before testing, the Pyrex ring was softened at 950°C for 1 hour to seal the button cell. In all tests the total gas flow rate was maintained at 50 sccm using MKS mass-flow controllers and the temperature was a constant 500°C.

Electrochemical tests were performed as outlined in Chapter 2. Briefly, data collection was performed using a Volta-Lab PGZ 301 (Radiometer Analytical) connected to a desktop computer running VoltaMaster 4 software. A general sequence of tests included open cell voltage (OCV), electrochemical impedance spectroscopy (EIS) at OCV (100 kHz to 100 mHz with an AC amplitude of 10 mA), and current amperometry (CA) experiments at overpotentials from 0 V to 1.0 V in increments of 50 mV. To ensure adequate sealing, only cells with initial OCVs in H_2 of 0.93 V at 500 °C and higher were accepted for complete electrochemical testing.

The analysis of EIS data was performed in the ZView program (Scribner Associates) by fitting impedance curves to an equivalent circuit model. All impedance experiments were performed in reference to the Pt reference electrode, therefore the resulting EIS data is representative of anode specific processes. This simplifies the analysis of the Nyquist plot because cathodic contributions are explicitly not part of the data collected in this fashion, leading to the use of a simple circuit model where anode processes may be accurately obtained. In the case of the SCF materials, only a single depressed semi-circle is apparent in impedance spectra therefore a simplified equivalent circuit model is used, abbreviated as ($L_1R_S[R_{CT}CPE_1]$). Here, L_1 is an inductor to account for impedance in electrode leads and CPE_1 is a constant phase element accounting for anode current variations (depressed Nyquist semi-circle). The circuit model also consists of a serial resistance (R_s), and a charge transfer resistance of the anode (R_{ct}) used to calculate the exchange current density (i_o) according to the low field approximated Butler-Volmer equation. This circuit model omits certain elements visible in the EIS data, such as Warburg diffusion parameters, in order to minimize error in the fitting of polarization resistances. In this study, and previous work on these SCF materials, the anode polarization resistance (R_p) is assumed to be equal to R_{ct} [10,13,14]. While the three electrode geometry is used to collect anode specific data, the cell power densities were calculated from chronoamperometry experiments at various overpotentials using both cathode and anode electrodes for data collection.

4.3 Results and Discussion

4.3.1 Performance under 5% H_2S / 95 % H_2

Three promising perovskite anode materials are being considered: $Sm_{0.95}Ce_{0.05}FeO_{3-\delta}$, $Sm_{0.95}Ce_{0.05}Fe_{0.97}Ni_{0.03}O_{3-\delta}$ and $Sm_{0.95}Ce_{0.05}Fe_{0.97}Co_{0.03}O_{3-\delta}$ abbreviated as SCF, SCF-Ni and SCF-Co, respectively. To compare the performance of the different anode compositions under H_2S containing fuels, it is pertinent to first obtain cell data under pure H_2. Performance in pure hydrogen allows us to assess the cell stability and account for slight differences in cell to cell values for initial OCV, R_{ct} and power density which arise from the fabrication process. Therefore in analyzing the data it is important to compare not only the quantitative values but also the degree to which each cell measurement changes when altering fuel composition. The performance of the three cells in pure H_2 at 500°C is compared first by considering the OCVs and power densities plotted in Figure 4.1 a and c, respectively. It is important to note that in this study we expect low values for power and current due to the very thick electrolyte used [10,14]. As is seen in Figure 4.1 a, all three anode materials have similar OCVs in pure H_2 ranging from 0.94-0.98 V. These values are lower than the theoretical Nernst potential at 500°C, a trend that is consistent with the use of SDC electrolytes for SOFCs. The low densification of the SDC electrolyte along with partial reduction at the anode lead to current leakage and reduced OCVs [19–21].

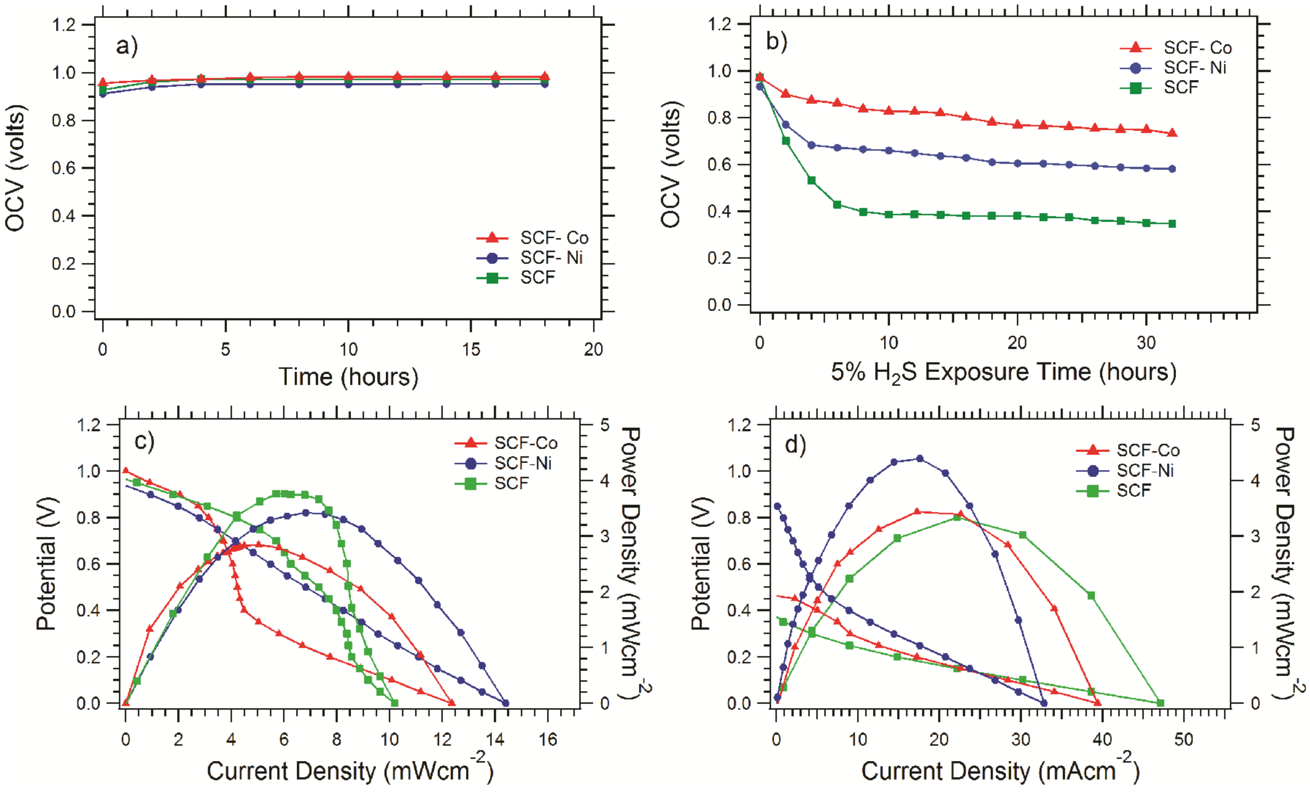

Figure 4.1: OCV's of SCF cells at 500°C in a) H_2 and b) 5% H_2S/95% H_2 and Power Density curves in c) H_2 and d) 5% H_2S/95% H_2.

The power density of each anode is plotted in Figure 4.1 c showing that all cells maintain similar outputs at 500°C when operating in pure H_2. After running each cell for 14 hours in H_2, 5% H_2S was introduced into the fuel stream and the same sequence of programmed experiments was performed in repetition for 30 hours. The resulting change in OCV for each cell versus sulfur exposure time is plotted in Figure 4.1 b. Clearly evident for all anodes is an immediate decrease in OCV upon introduction of sulfur to the fuel stream, with SCF having the largest decrease. After the initial 2-4 hr drop in OCV, the cells slightly stabilize and a moderately flat potential is seen for all anode materials. The OCVs continues to decrease within the measured time frame, however to a lesser extent. This is in contrast to trends observed in Ni-YSZ and other Ni containing SOFC anode materials, where the cell potential continues to drop drastically when

H_2S is maintained in the fuel stream. This is characteristic of poisoning/delamination of the anode from the electrolyte, ultimately leading to loss of the cell [4,5,22,23].

The I-P curves after 30 hours in H_2S indicate stable power from each anode material. The power density of each cell after 30 hours in 5% H_2S is shown in Figure 4.1 d. It is clear that each cell has had an increase in current density, representative of improved electrode-electrolyte contact, as will be shown later in the text. The peak power densities of the SCF and SCF-Ni cells have decreased slightly whereas the SCF-Co cell has increased from 2.8 to 4.5 $mWcm^{-2}$. This increased power density in H_2S containing fuels is uncommon; sulfur impurities are conventionally associated with performance drop [4,23]. We attribute this increased performance to the formation of metal sulfides that drastically increase the conductivity and connectivity of the anode. The formation of active sulfides was demonstrated with Ni-YSZ cermets under high sulfur conditions [17,18,24,25].The increase in power demonstrates the viability of the SCF cells to operate in high concentration H_2S fuel environments.

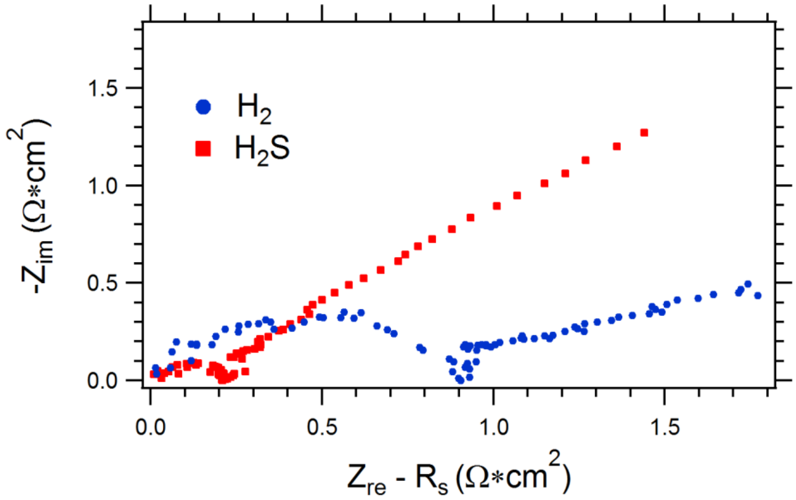

Figure 4.2: EIS spectra of SCF-Ni cell at 500°C in H_2 and 5% H_2S/95% H_2.

Analysis of the EIS data (Figure 4.2) also demonstrates the viable performance of these anodes in 5% H_2S. All cells exhibit a decreased serial resistance under 5% H_2S, indicative of an improvement in electrode-electrolyte contact and overall increased anode conductivity. The R_{ct}, determined as the difference between high and low frequency intercepts of a Nyquist plot, is used to calculate the i_0 for the charge transfer reaction taking place at the triple phase boundary of the anode. A lower R_{ct} leads to an increase in i_0, indicative of an improvement in anode performance for fuel oxidation. Figure 4.2 shows a typical EIS comparison of the SCF-Ni cell in H_2 and after 30 hours exposure to 5% H_2S. The impedance arc has reduced in size drastically, with a lower R_{ct} than in pure H_2. This is seen for all cells when exposed to 5% H_2S. These result are in drastic contrast with the poisoning observed in traditional Ni based anodes; state of the art Ni-YSZ anodes undergo a rapid increase in polarization resistance when exposed to low concentrations of H_2S (1-8 ppm) [26,27]. Typically, the extent of degradation is proportional to the concentration of H_2S in the fuel, however some studies have demonstrated improved performance of Ni-YSZ anodes when exposed to high concentrations (10%) of H_2S at temperatures >800°C [17,18,24]. The metal-sulfides produced in these anodes offer superior polarization resistances and current densities in H_2S than in pure H_2, similar to the results obtained in the current work however at much higher operating temperatures.

Table 4.1 summarizes the impedance data for the three anodes before and after introduction of 5% H_2S into the fuel stream. Here it is clear that all three anode materials have improved performance in 5% H_2S. A value of i_0 H_2S / i_0 H_2 greater than 1 indicates an increased exchange current density in H_2S containing fuels. The i_0 has increased in each case with the SCF-Co cell showing the greatest improvement from 53.29 to 302.77 mA/cm^2 upon introducing 5% H_2S. The improved performance of SOFC anodes in high concentrations of H_2S is an uncommon phenomenon however it is not unique to this work. For example; Liu et al. reported perovskite anodes of the type $La_{0.7}Sr_{0.3}VaO_3$ that exhibit improved performance in fuel compositions as high as 10% H_2S [28]. The improvement in that case is attributed to the formation of a highly conductive, sulfated perovskite anode that drastically reduces the anode-electrolyte interfacial resistance [28,29]. In comparison to the current work, the LSV anode exhibited an R_{ct} of ~5.5 Ωcm^2 at 900°C in 10% H_2S, an order of magnitude larger than the SCF anodes tested in this work at 500°C.

Table 4.1: AC Impedance data of SCF cells at 500 °C in H_2 and 5% H_2S / 95 % H_2.

Anode Material	**Fuel**	**OCV** (Volts)	**R_s** (Ω*cm^2)	**R_{ct}** (Ω *cm^2)	**i_0 H_2S / i_0 H_2**
$Sm_{0.95}Ce_{0.05}FeO_3$	H_2	0.971	39.16	0.83	
	5% H_2S	0.346	6.26	0.36	2.31
$Sm_{0.95}Ce_{0.05}Fe_{0.97}Ni_{0.03}O_3$	H_2	0.952	19.35	0.94	
	5% H_2S	0.584	9.25	0.24	3.92
$Sm_{0.95}Ce_{0.05}Fe_{0.97}Co_{0.03}O_3$	H_2	0.981	40.25	1.25	
	5% H_2S	0.748	11.63	0.22	5.68

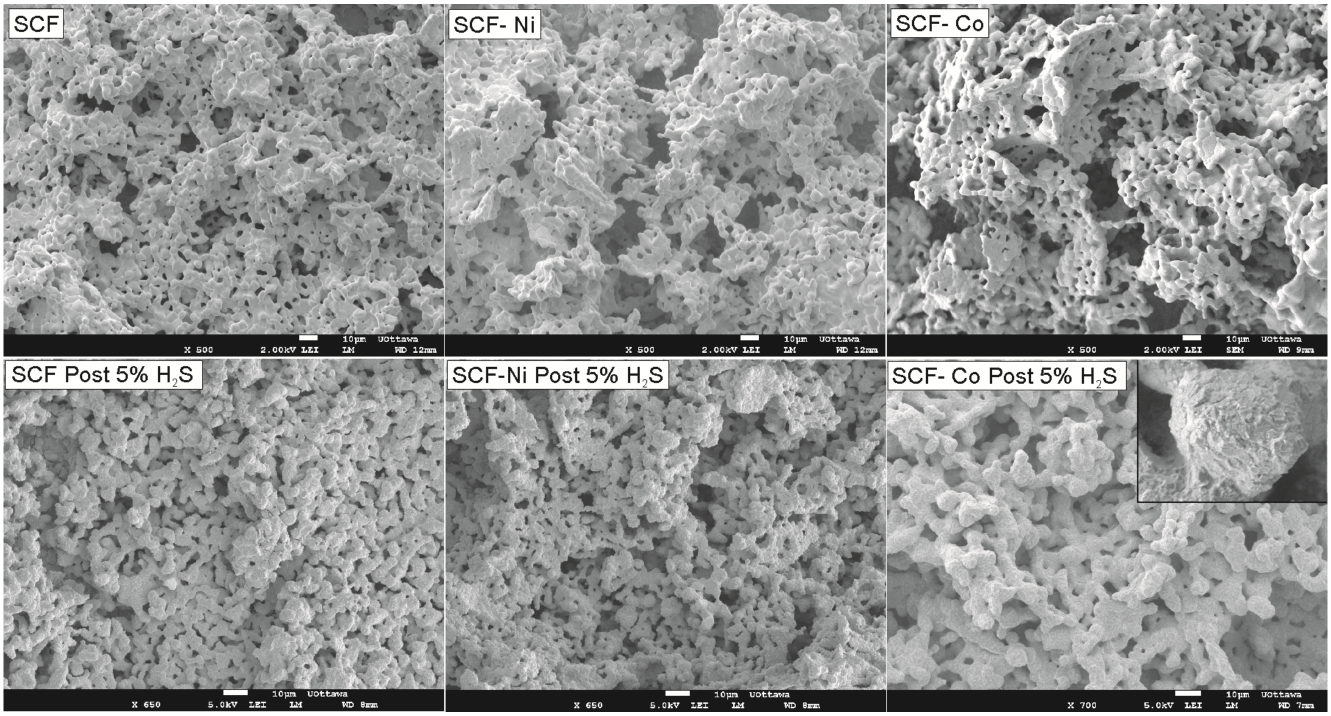

Figure 4.3: SEM images of SCF anodes pre (top row) and post (bottom row) testing in 5% H_2S / 95% H_2.

In an attempt to determine the active species responsible for the performance increase, in depth post mortem analyses are performed. The anode, after performance in H_2S, is rapidly quenched by complete removal of the fuel cell apparatus from the tube furnace. The anode atmosphere is maintained as 5% H_2S/ 95% H_2. in an effort to preserve the active species without further reaction. Once cooled, the anode is removed and characterized using SEM and p-XRD. The exact anode species present under operating conditions cannot be determined; nevertheless, post-mortem characterization of the quenched anodes provides an indication of what is happening during operation. Figure 4.3 shows the anode microstructures before and after testing in 5% H_2S. The perovskite microstructure has been maintained but with a roughening of the grain surfaces due to the production of sulfides and yielding an appearance similar to igneous rock. The anodes show different degrees of surface modification with the SCF cell affected to the greatest extent. The insert for the SCF-Co anode post 5% H_2S is a higher magnification image of the sulfur modified perovskite surface. The high concentration of H_2S seems to have little effect on the overall micro-structure of these anodes; a promising attribute.

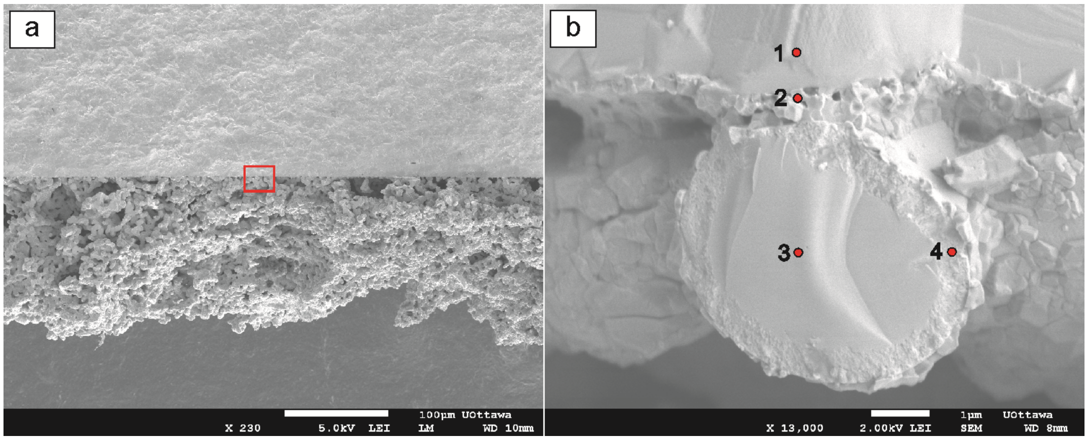

Figure 4.4: Cross sectional EDS analysis of SCF-Co cell after testing in 5% H_2S.

Table 4.2: Atomic percentages from EDS point analyses in Figure 4.

EDS Point	**Element**				
	Sm	**Ce**	**Fe**	**O**	**S**
1	8.64	37.72		53.64	
2			22.63	31.06	46.31
3	13.63	1.1	13.63	71.63	
4	17.23	1.8	6.62	51.02	23.33

Figure 4.4 shows an example of a post mortem cross sectional EDS experiment performed on the SCF-Co anode. Figure 4.4 a is a low magnification image showing the anode, approximately 100 µm in thickness, attached to the dense SDC electrolyte. The red square indicates the zoomed-in area for Figure 4.4 b. EDS point analysis was performed in Figure 4.4 b with the relative atomic percentages listed in Table 4.2. The first point corresponds to the dense SDC electrolyte and, as expected, shows no signs of sulfur, only the SDC components (Sm, Ce

and O) are visible. As well, the SDC electrolyte appears to be Sm rich and oxygen deficient, as expected for the anode side of a dense electrolyte. The second point analysis was performed on the thin layer interfacing the anode and electrolyte. Here we see large incorporation of S and Fe, an indication of FeS_2 segregation at the functional layer of the anode. Point 3 corresponds to the interior of the perovskite network and shows no sign of sulfur penetration., That is, the micrometer perovskite structures contain a core of pure perovskite (no sulfur) with approximately the nominal stoichiometry. EDS analysis of Point 4 in Figure 4.4 b represents the ~100 nm thick coating of the perovskite structure where large contributions of sulfide species are apparent, giving it an igneous rock-type appearance. These results strongly indicate that 5% H_2S poisoning of the SCF-Co anode has resulted in only a surface modification of the perovskite particles with the bulk perovskite microstructure remaining intact. The evolution of FeS_2 on the perovskite surface and at the interface between the anode and electrolyte is primarily responsible for the improved performance of these anodes in H_2S fuels. FeS_2 (Pyrite) is known for its high electronic conductivity and catalytic properties that make it especially applicable for Li battery electrodes [30–32]. Our work indicates that it may also be of interest for SOFC anodes in sulfur containing fuels.

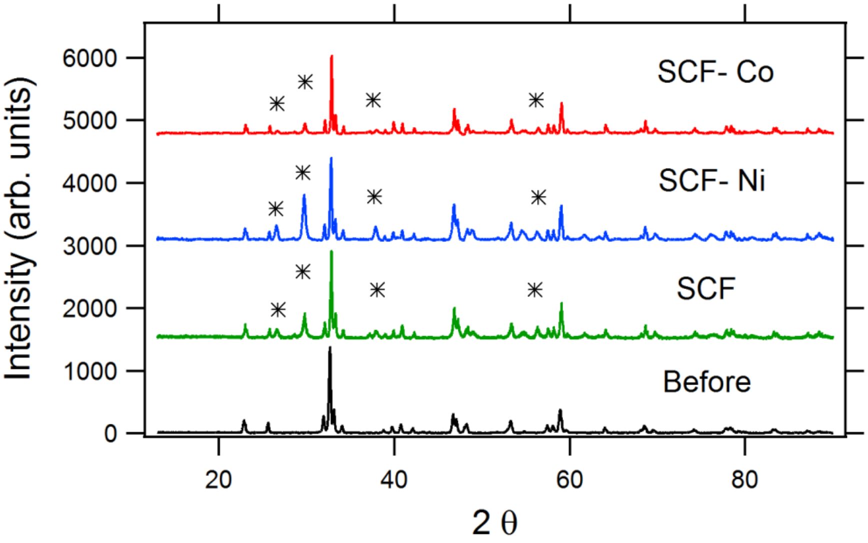

Figure 4.5: Powder XRD of anode materials before and after testing in 5% H_2S.

Post mortem p-XRD of the anode materials was performed in an attempt to identify the species responsible for the performance increase. The powder X-ray diffraction spectra for the post mortem anodes are shown in Figure 4.5. For comparison, the as prepared SCF perovskite spectrum is shown (Before spectrum). The bulk perovskite phase, $SmFeO_{3-\delta}$ (PDF # 39-1490), has been maintained in each anode after performance in 5% H_2S along with the evolution of additional peaks indicated by asterisks. No single material corresponds to the diffraction peaks, but rather multiple metal sulfide species along with elemental sulfur appear to be present in the quenched anode material. More specifically, the principal peaks of FeS_2 (PDF # 006-0710), Sm_3S_4 (PDF # 04-002-5993) and S (PDF # 04-007-2083) fit the additional peaks. Evolution of these materials is consistent with the hypothesis that H_2S leads to the partial sulfidation of the anode, responsible for the performance increase. These results are consistent with the elemental compositions from EDS analysis and reinforce the conclusion that even at 5% H_2S fuel concentration only a portion (the surface of the particles) of the anode material is sulfidated. The extent of poisoning, or formation of metal sulfide phase, can be qualitatively compared by the intensities of the newly formed peaks. The SCF-Co material shows very low levels of sulfide phase formation in comparison to the SCF and SCF-Ni anodes.

4.3.2 Performance under 0.5% H_2S / 99.5% H_2

The anode materials under study, particularly SCF-Co, have shown considerable tolerance to H_2S in the fuel stream and the increased performance of each anode in 5% H_2S is of great interest. This concentration of sulfur is extremely high, and while it has been used in the past to test accelerated poisoning, it is only applicable to highly sour fuel feeds [33]. To determine if this performance enhancement exists at a lower, more common sulfur concentration, and to explore the stability of the surface sulfide species, the three anodes were tested similarly in 0.5% H_2S / 99.5% H_2. The performance of the three cells in pure H_2 at 500°C is compared first by the OCVs and power densities plotted in Figure 4.6 a and c respectively. All three cells have OCVs in H_2 of 0.95-1.05 V and power densities on the order of 2 $mWcm^{-2}$. The resulting change in OCV for each cell versus sulfur exposure time is plotted in Figure 4.6 b. Clearly evident for all cells is an immediate decrease in OCV upon introduction of sulfur to the fuel stream. For the SCF and SCF-Co cells the OCV drop occurs rapidly in the first 2 hours and then begins to stabilize at a lower value than in H_2. The OCV of the SCF-Ni cell does not stabilize and continues to decrease throughout the entire measurement period. This is most likely due to changes in the microstructure and poisoning/delamination of the SCF-Ni material. All three anodes show increased current densities in H_2S fuel conditions along with increased power densities for the SCF and SCF-Co cells. The SCF-Ni cell shows almost an unchanged peak power density whereas that of the SCF and SCF-Co cells has increased by a factor of ~2. Again, we conclude that the increased current densities arise from the formation of conductive metal sulfide species on the anode surface.

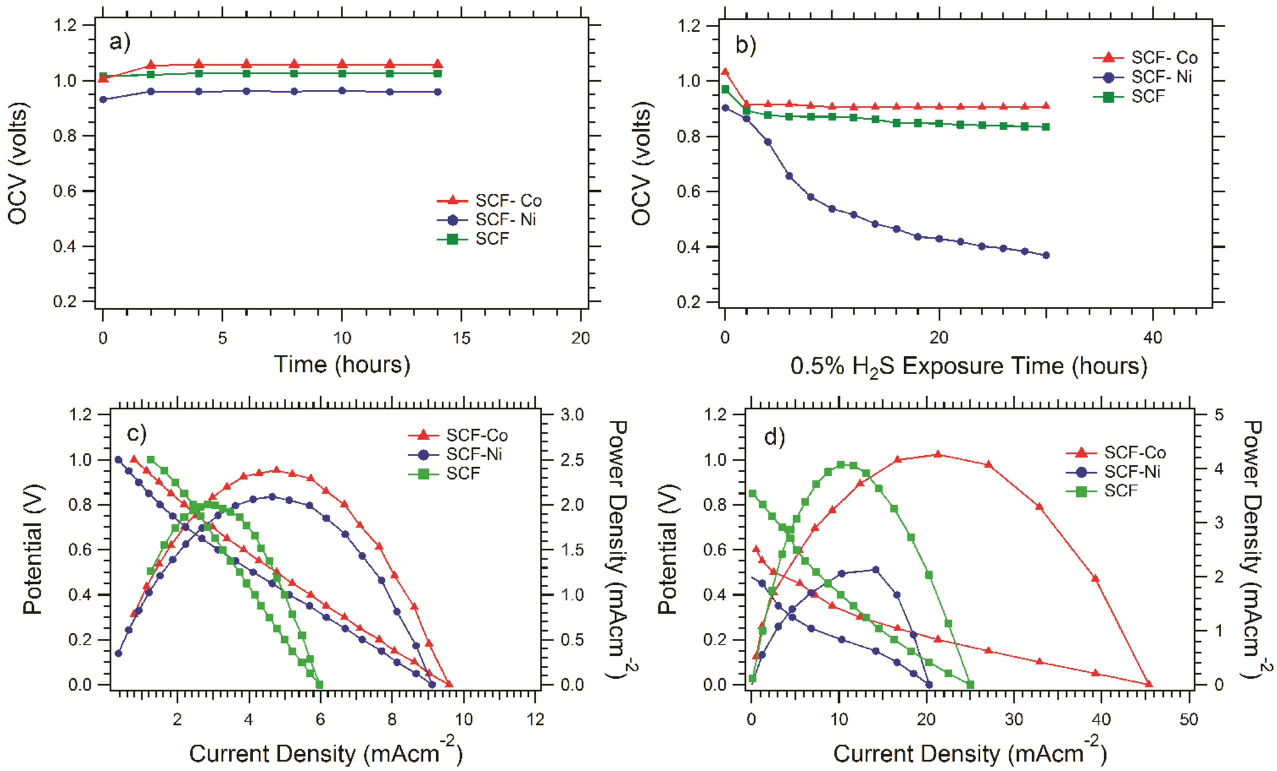

Figure 4.6: OCVs of SCF cells at 500°C in a) H_2 and b) 0.5% H_2S/95% H_2 and Power Density curves in c) H_2 and d) 0.5% H_2S/95% H_2.

Figure 4.7 shows a typical comparison of EIS data (Nyquist plots) of the SCF-Co cell in H_2 and after 30 hours in 0.5% H_2S. The R_s value has been subtracted from the x axis to facilitate comparison. The R_{ct} has decreased significantly after introducing H_2S into the fuel, evidence of the improvement in anode performance. Table 4.3 summarizes the EIS data obtained from impedance measurements and the calculated i_0 H_2S / i_0 H_2 values for the three anodes. The SCF-Ni anode material shows a performance drop, lower i_0, upon introduction of 0.5% H_2S. The EIS data for SCF-Ni, along with the drastically decreased OCV, allows us to conclude that the B site Ni dopant reacts unfavorably with 0.5% H_2S fuel concentrations. We hypothesize that at this temperature and sulfur concentration the affinity of nickel toward formation of nickel sulfide species leads to the severe micro-structural changes in the perovskite anode that ultimately lower performance. On the other hand, a decreased R_{ct} is seen for the SCF and SCF-Co cells when operating in 0.5% H_2S with the SCF-Co cell having the greatest improvement. The i_o of the SCF cell has increased by a factor of 1.9 whereas that of the SCF-Co has increased drastically, from 13.72 to 127.02 mA/cm^2. The R_{ct} and i_o of the SCF and SCF-Co cells before and after performance in H_2S are superior to other materials considered to be sulfur tolerant SOFC anodes [9,34–36]. For instance, sulfur tolerant LSV/GDC anodes at 800°C exhibit R_{ct} values of approximately 12 and 14 Ω*cm^2 in H_2 and syngas/H_2S, respectively [35].

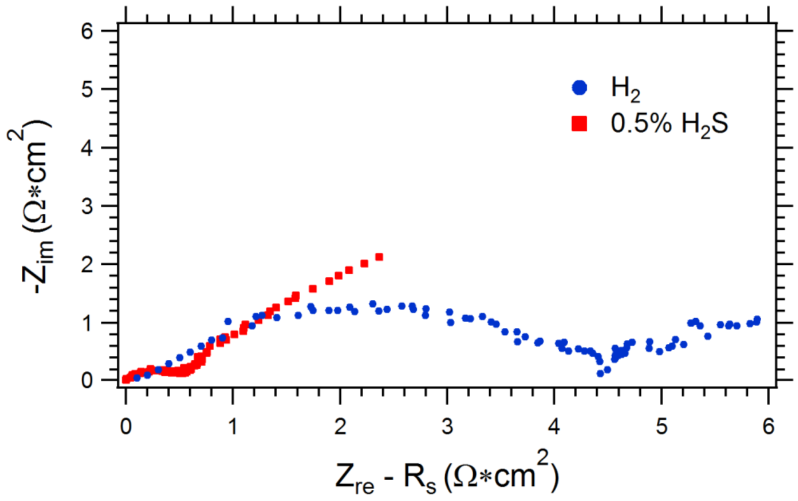

Figure 4.7: EIS spectra of SCF-Co cell at 500°C in H_2 and 0.5% H_2S/99.5% H_2.

Interestingly, the SCF-Ni material shows improved performance in 5% H_2S fuel in comparison to a reduced performance in 0.5% H_2S. This indicates that the concentration of H_2S is directly affecting the micro-structure, and hence performance of the SCF-Ni anode material. We hypothesize that in 5% H_2S fuels, the formation of FeS_2 and Sm_3S_4 on the perovskite surface occurs rapidly. This highly conductive metal sulfide layer may deter the further sulfidation of the anode and bypass the micro-structural changes observed under 0.5% H_2S.

Table 4.3: AC Impedance data of SCF cells at 500 °C in H_2 and 0.5% H_2S / 99.5% H_2.

Anode Material	**Fuel**	**OCV** (Volts)	**R_s** (Ω*cm^2)	**R_{ct}** (Ω *cm^2)	**i_0 H_2S / i_0 H_2**
$Sm_{0.95}Ce_{0.05}FeO_3$	H_2	1.026	53.71	2.28	
	0.5% H_2S	0.833	13.72	1.20	1.91
$Sm_{0.95}Ce_{0.05}Fe_{0.97}Ni_{0.03}O_3$	H_2	0.959	46.75	3.87	
	0.5% H_2S	0.369	34.58	4.51	0.86
$Sm_{0.95}Ce_{0.05}Fe_{0.97}Co_{0.03}O_3$	H_2	1.057	35.03	4.85	
	0.5% H_2S	0.908	8.846	0.52	9.26

Post mortem analyses were performed on the quenched anodes with SEM images of the anode surfaces before and after testing shown in Figure 4.8. The SCF and SCF-Co cells have maintained the perovskite microstructure but with the same igneous surface modification witnessed in the 5% tests. On the other hand, the SCF-Ni anode has a completely changed micro-structure with the appearance of large crystallites on the order of 10 µm in size. EDS analysis indicates that these crystals contain high concentrations of Fe and S. Cross sectional EDS analyses of the SCF and SCF-Co anodes confirm that the perovskite structure has been maintained but with a surface modification containing metal sulfides.

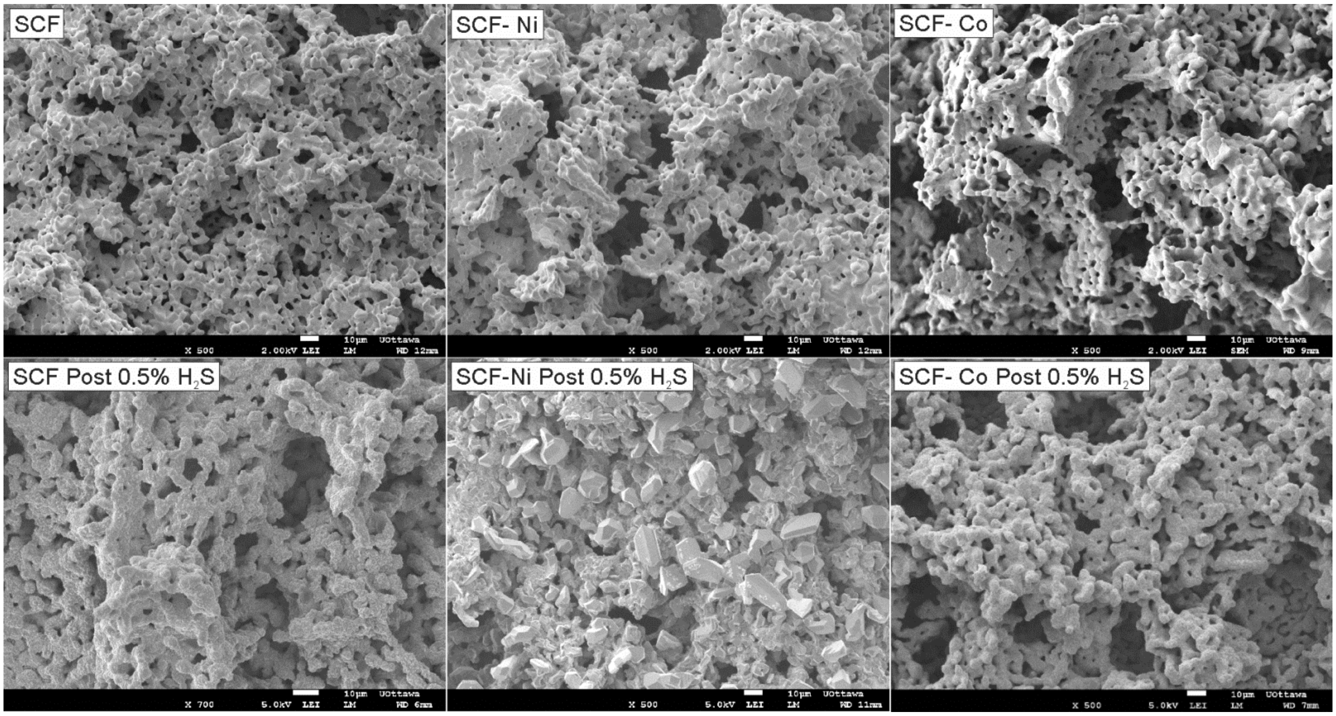

Figure 4.8: SEM images of SCF anodes pre (top row) and post (bottom row) testing in 0.5% H_2S / 99.5% H_2.

The p-XRD of anodes after performance in 0.5% H_2S are shown in Figure 4.9 with the as-prepared SCF spectrum for comparison. Again, the bulk orthorhombic $SmFeO_{3-\delta}$ phase is maintained but with varying degrees of sulfur modification to FeS_2, Sm_3S_4 and S. The SCF-Ni anode has prominent peaks for the sulfide phases and appears to be most affected by testing in 0.5% H_2S fuel. This is consistent with the post mortem SEM imaging of the anodes shown in Figure 4.8; concluding that the SCF-Ni cell has been severely poisoned, forming large crystals of metal sulfides.

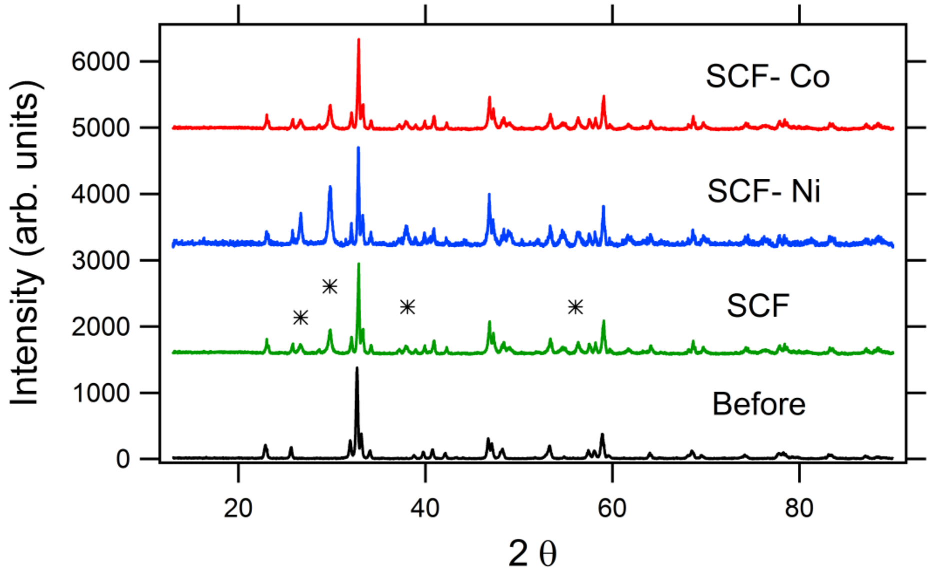

Figure 4.9: Powder XRD of anode materials before and after testing in 0.5% H_2S.

The post mortem analysis leads to a general conclusion that 0.5% H_2S exposure partially sulfidates the anode, predominantly on the perovskite surface, leading to improved performance (evident in the SCF and SCF-Co cells). This concentration is, however, detrimental to the SCF-Ni cell and leads to micro-structural changes that decrease performance. Combining its drastically improved performance in 0.5 and 5% H_2S with the previously reported coke tolerance makes the SCF-Co anode material attractive for LT-SOFC applications.

4.3.3 Sulfur Recovery Tests

The SCF-Co cell has shown promising stability and performance as a sulfur tolerant SOFC anode material. In order to study the reversibility of the metal sulfide layer formed, the SCF-Co cell was chosen for a trial of testing that involved performance in hydrogen at 500°C, then sulfidation in 0.5% H_2S, followed by removal of the H_2S to monitor the performance recovery. Figure 4.10 a shows the OCV versus time of the SCF-Co cell throughout the recovery testing. Arrows indicate the times at which H_2S is introduced/removed from the fuel stream. The

OCV decreases from 1.08 V in H_2 to 0.97 V at which point it stabilizes and does not decrease further. Removal of the H_2S from the fuel leads to recovery of the initial OCV value within 4 hours. This demonstrates the reversibility of the OCV with respect to sulfur containing fuels. Figure 4.10 b plots the R_s of the cell with respect to time. The R_s stabilizes in H_2 and then decreases rapidly upon introduction of 0.5% H_2S and does not reach a minimum in the 14 hour time frame. Removal of the H_2S leads to increased R_s that stabilizes after ~10 hours at a value greater than the initial R_s in H_2. This can be explained by the partial removal of sulfur from the anode when changing back to pure H_2. As mentioned earlier, the FeS_2 interfacial layer is largely responsible for the decreased R_s in H_2S; therefore partial removal of this layer would lead to decreased electrode-electrolyte contact and an increased resistance.

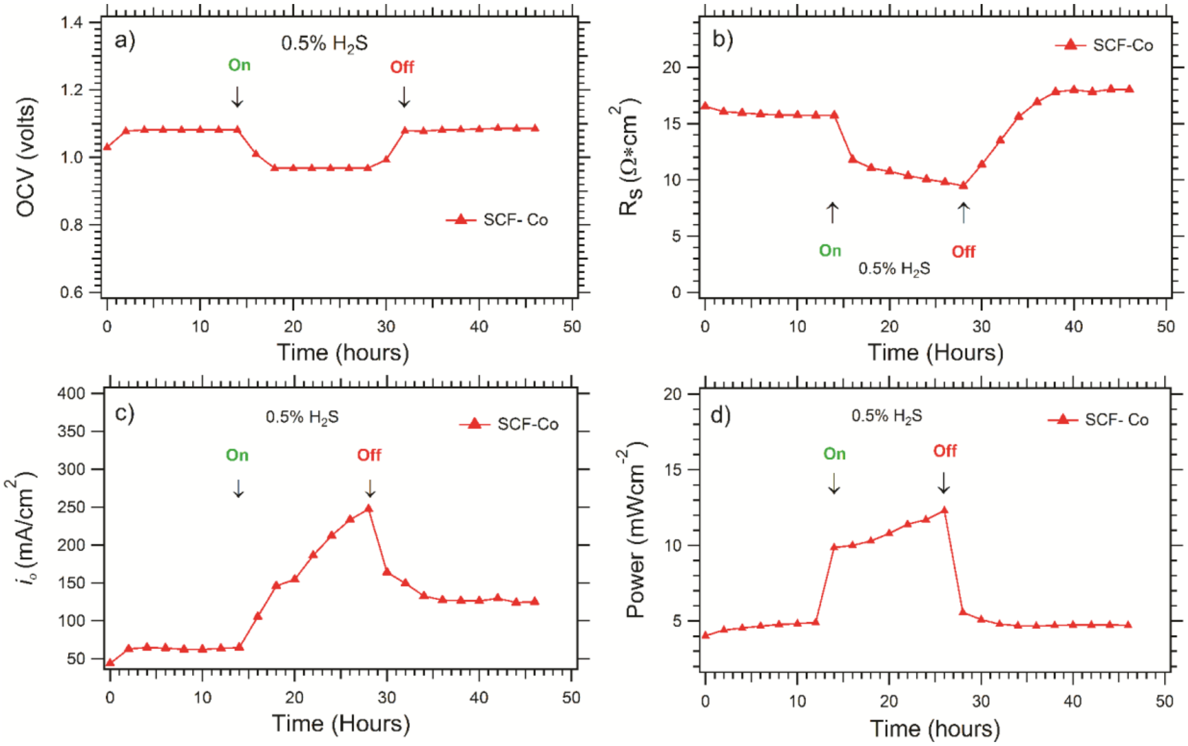

Figure 4.10: Recovery tests of SCF-Co cell versus time. 0.5% H_2S introduced at 14 hours and removed at 28 hours. a) OCV b) R_{ct} from EIS c) i_o from EIS d) power density at an overpotential of 450 mV.

Figure 4.10 c shows the i_o values from impedance measurements every 2 hours for the SCF-Co anode. Introducing 0.5% H_2S leads to increased exchange current density that does not stabilize within the measurement time frame. Removal of the H_2S leads to a decrease in i_o that stabilizes at a value greater than originally measured in H_2. This indicates that sulfidation of the anode leads to an irreversible change in the R_{ct}, improving the anode performance even when switching back to pure H_2. This is most likely representative of sulfide species remaining on the perovskite surface; the anode only partially returns to its initial composition and remains more active. Figure 4.10 d plots the power density of the SCF-Co at an overpotential of 450 mV versus cell operation time. This plot shows that the cell power output increases in sulfur containing fuels and then returns to the original power after removal of the H_2S. While these tests conclude that the sulfidation process is not completely reversible, the anode performance recovers and maintains an increased i_o when sulfur is removed from the fuel stream.

Post mortem SEM imaging of the SCF-Co cell (Figure 4.11 a) indicates that the anode microstructure is maintained, as expected. Figure 4.11 b is a higher magnification image of the anode after recovery and shows clusters of a separate phase on the perovskite surface. This indicates that formation of the metal sulfide layer is only partially reversible within the experimental time frame. This is also evident from the p-XRD shown in Figure 4.12; the phases for S, FeS_2 and Sm_3S_4 remain in the spectrum after recovery in H_2. The remnants of conductive metal sulfides on the anode surface are responsible for the increased i_o after recovery in H_2.

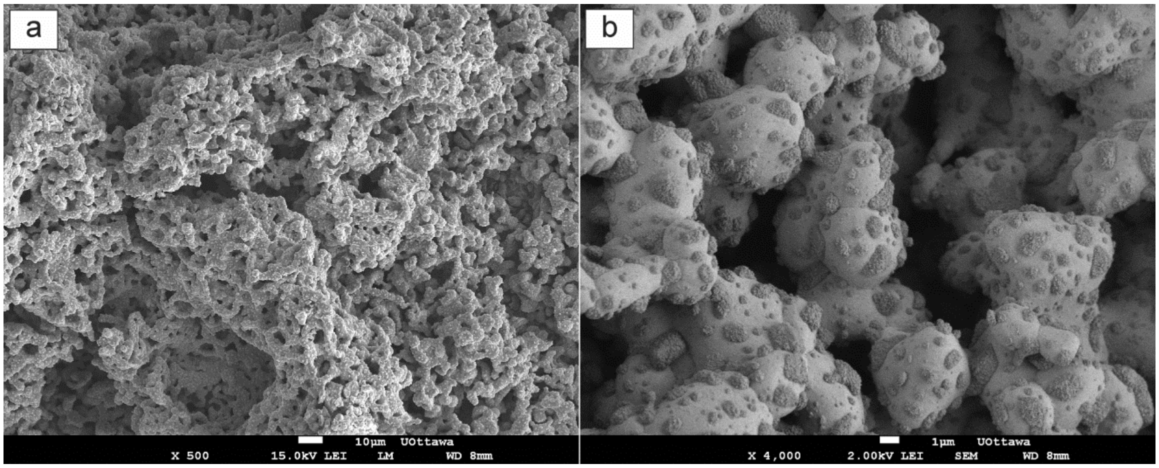

Figure 4.11: SEM images of SCF-Co anode post recovery testing.

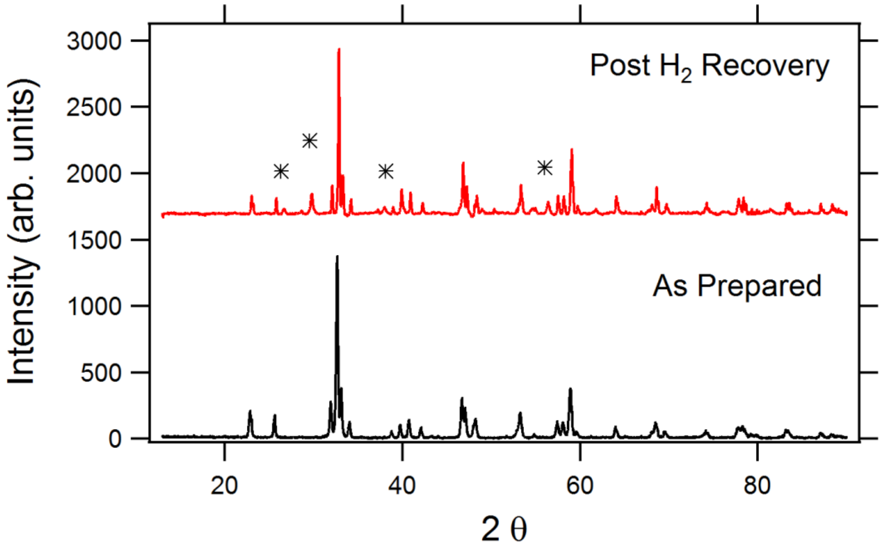

Figure 4.12: Powder XRD of SCF-Co material as prepared and post recovery testing.

4.4 Conclusions

A series of doped perovskite anode materials, SCF, SCF-Ni, SCF-Co, have been tested for sulfur tolerance at 500°C. Results indicate that the introduction of 5% H_2S enhances the performance of these anodes, verified by EIS and CA experiments. Post mortem analyses indicate that the performance enhancement arises from the partial sulfidation of the anode, leading to the formation of FeS_2, Sm_3S_4 and S on the perovskite surface. Testing in lower concentrations of sulfur, 0.5% H_2S, also enhances the performance of these anode materials. Specifically, the SCF-Co anode shows an increased i_o from 13.72 to 127.02 mA/cm^2 when switching to 0.5% H_2S/99.5% H_2 fuel composition. Recovery tests performed on the SCF-Co anode conclude that the OCV and power density of these cells are reversible within 4 hours of removal of sulfur fuel. Also, we conclude that the formation of metal sulfide species is only partially reversible, yielding an anode material with an overall lower R_{ct} upon switching back to pure $H_{2.}$ Combining their performance in sulfur containing fuels with their previously reported coke tolerance makes these perovskites especially attractive as LT-SOFC anodes in sour fuels.

4.5 References

[1] E.D. Wachsman, K.T. Lee, Science 334 (2011) 935.

[2] J.T.S. Irvine, Perovskite Oxide for Solid Oxide Fuel Cells, Springer US, Boston, MA, 2009.

[3] S.C. Singhal, K. Kendall, High Temperature Solid Oxide Fuel Cells, Elsevier Inc., New York, USA, 2003.

[4] Z. Cheng, J.-H. Wang, Y. Choi, L. Yang, M.C. Lin, M. Liu, Energy Environ. Sci. 4 (2011) 4380.

[5] W.. Zhu, S.. Deevi, Mater. Sci. Eng. 362 (2003) 228.

[6] A. Atkinson, S. Barnett, R.J. Gorte, J.T.S. Irvine, a J. McEvoy, M. Mogensen, S.C. Singhal, J. Vohs, Nat. Mater. 3 (2004) 17.

[7] A. Ovalle, J. Ruizmorales, J. Canalesvazquez, D. Marrerolopez, J. Irvine, Solid State Ionics 177 (2006) 1997.

[8] Z. Cheng, S. Zha, L. Aguilar, D. Wang, J. Winnick, M. Liu, Electrochem. Solid-State Lett. 9 (2006) A31.

[9] L. Aguilar, S. Zha, Z. Cheng, J. Winnick, M. Liu, J. Power Sources 135 (2004) 17.

[10] S.M. Bukhari, J.B. Giorgi, J. Power Sources 198 (2012) 51.

[11] S.M. Bukhari, J.B. Giorgi, J. Electrochem. Soc. 158 (2011) J159.

[12] S.M. Bukhari, J.B. Giorgi, Sensors Actuators B Chem. 181 (2013) 153.

[13] S.M. Bukhari, J.B. Giorgi, ECS Trans. 35 (2011) 1539.

[14] S.M. Bukhari, J.B. Giorgi, ECS Trans. 33 (2011) 81.

[15] S.M. Bukhari, J.B. Giorgi, Solid State Ionics 180 (2009) 198.

[16] S.M. Bukhari, J.B. Giorgi, Solid State Ionics 194 (2011) 33.

[17] C.M. Grgicak, R.G. Green, J.B. Giorgi, J. Power Sources 179 (2008) 317.

[18] C.M. Grgicak, J.B. Giorgi, J. Phys. Chem. C 111 (2007) 15446.

[19] H. Shi, W. Zhou, R. Ran, Z. Shao, J. Power Sources 195 (2010) 393.

[20] T. Miyashita, ECS Trans. 28 (2010) 39.

[21] T. Miyashita, Electrochem. Solid-State Lett. 14 (2011) B66.

[22] Z. Cheng, S. Zha, M. Liu, J. Electrochem. Soc. 153 (2006) A1302.

[23] Y. Matsuzaki, I. Yasuda, Solid State Ionics 132 (2000) 261.

[24] C.M. Grgicak, M.M. Pakulska, J.S. O'Brien, J.B. Giorgi, J. Power Sources 183 (2008) 26.

[25] J.S. O'Brien, J.B. Giorgi, J. Power Sources 200 (2012) 14.

[26] S. Zha, Z. Cheng, M. Liu, J. Electrochem. Soc. 154 (2007) B201.

[27] L. Yang, Z. Cheng, M. Liu, L. Wilson, Energy Environ. Sci. 3 (2010) 1804.

[28] L. Aguilar, S. Zha, S. Li, J. Winnick, M. Liu, Electrochem. Solid-State Lett. 7 (2004) A324.

[29] S. Zha, P. Tsang, Z. Cheng, M. Liu, J. Solid State Chem. 178 (2005) 1844.

[30] Y. Shao-Horn, S. Osmialowski, Q.C. Horn, J. Electrochem. Soc. 149 (2002) A1499.

[31] M. Morsli, A. Bonnet, L. Cattin, A. Conan, S. Fiechter, Les Ed. Phys. (1995) 699.

[32] R. Schieck, A. Hartmann, S. Fiechter, R. Konenkamp, H. Wetzel, J. Mater. Res. 5 (1990) 1567.

[33] Environmental Protection Agency, Federal Air Quality Control Regions, Research Triangle Park, NC, 1972.

[34] L. Zhang, S.P. Jiang, H.Q. He, X. Chen, J. Ma, X.C. Song, Int. J. Hydrogen Energy 35 (2010) 12359.

[35] M. Cooper, K. Channa, R. De Silva, D.J. Bayless, J. Electrochem. Soc. 157 (2010) B1713.

[36] Z. Xu, J. Luo, K.T. Chuang, J. Electrochem. Soc. 154 (2007) B523.

Chapter 5:
Conductivity of Y doped $BaMoO_3$ perovskites and applications as IT-SOFC anode materials

Abstract

A new perovskite family $Ba_{1-x}Y_xMoO_3$ (x=0-0.05) has been investigated in regards to electrical conductivity and performance as IT-SOFC anode materials for the oxidation of H_2. Refinement of p-XRD spectra as well as SEM imaging conclude that the solubility limit of Y doping at the A site is 5 mol%, beyond which Y_2O_3 segregation occurs. The undoped $BaMoO_3$ sample has a colossal room temperature conductivity of 2500 S/cm in dry H_2. All materials maintain metallic conductivity in the temperature range of 25-1000°C with resistance increasing with Y doping. The $Ba_{1-x}Y_xMoO_3$ (x=0, 0.05) materials exhibit good performance as SOFC anode materials between 500-800°C, with R_{ct} values at 500°C in dry H_2 of 3.15 and 6.33 ohm*cm^2 respectively. The catalytic performance of these perovskite anodes is directly related to electronic conductivity, as concluded from composite anode performance.

5.1 Introduction

The solid oxide fuel cell (SOFC) is a promising device capable of direct chemical to electrical energy conversion with high efficiencies and low emissions. However, the commercial viability of SOFCs is limited by several factors, one of which is the extremely high operating temperatures (>800°C) required for adequate performance [1–4]. This has led to a spur of research into new materials for low and intermediate temperature solid oxide fuel cells (IT-SOFCs) in an attempt to reduce the material costs and facilitate the balance of plant. Perovskites of the type ABO_3, where A and B are metal cations, have been extensively reported in the past decade as promising alternative SOFC anode materials due to their low cost, simple fabrication, and high catalytic performance at reduced temperatures [3,5–9].

Molybdenum based perovskites (ABO_3 where B = Mo) have long been known to exhibit metallic like behavior with impressive electronic conductivities, as well as high stability in reducing atmospheres at elevated temperatures [10–12]. Additionally, alkali earth molybdates such as $AMoO_3$ (A= Sr,Br) have been reported with high catalytic activity for the direct oxidation of alcohols [13]. The catalytic activity of Mo and high electronic conductivity make these materials attractive as SOFC anode materials.

Recently, the performance of several Mo perovskites as SOFC anode materials has been reported in the literature [14–20]. For example, $SrMo_{1-x}Fe_xO_3$ and $SrMo_{1-x}Cr_xO_3$ perovskites have been demonstrated as SOFC anodes with impressive power densities in H_2 at 800-850°C, however the low temperature performance has not been investigated [15,16]. As well, double perovskites such as Sr_2MgMoO_6 and Ba_2MgMoO_6 have been shown to have higher tolerance to H_2S (140 ppm) in comparison to traditional Ni-YSZ cermet anodes [19]. In all cases, the catalytic performance is said to arise from the B site Mo in these perovskites.

Here we report on the synthesis, structural and electronic characterization of a new family of perovskites with formulae $Ba_{1-x}Y_xMoO_3$ (x=0-0.05). The effect of Y doping on electronic conductivity is investigated, in an attempt to increase the ionic conductivity in these materials. As well, the application of these materials as SOFC anodes for the oxidation of H_2 at 500-800°C is reported.

5.2 Experimental

5.2.1 Powder Synthesis

The preparation of alkali-earth molybdate perovskites is generally performed by high temperature reduction of the corresponding scheelite phase. Scheelite-type materials of formulae $Ba_{1-x}Y_xMoO_4$ (x=0-0.07) were prepared by decomposition of citrate precursors using the sol-gel method. Starting materials included: Barium nitrate ($Ba(NO_3)_2$, AlfaAesar, 99.9%), yttrium nitrate hexahydrate ($Y(NO_3)_3 \cdot 6H_2O$), AlfaAesar, 99.9%), ammonium molybdate tetrahydrate ($(NH_4)_6Mo_7O_{24} \cdot 4H_2O$, AlfaAesar, 99.9%) and citric acid monohydrate (AlfaAesar, minimum 99%). Solids were weighed according to the desired stoichiometry and dissolved separately in de-ionized water. The resulting precursor solutions were combined and added to aqueous citric acid so that the ratio of citric acid to total metal ion was 1:1. The solution was dried at 120°C for 24 hours resulting in a citrate gel precursor that was subsequently ground and calcined at 700°C for 24 hours using heating/cooling ramp rates of 5°C/min.

The resulting white powder (Scheelite phase) was thoroughly ground and reduced in a tube furnace at 700°C for 16 hours in an atmosphere of H_2. The total gas flow rate of H_2 was 50 sccm, maintained with an Alicat mass flow controller. Complete reduction to the perovskite phase with formulae $Ba_{1-x}Y_xMoO_3$ (x=0-0.07) was indicated by a color change to dark red/black, verified by XRD.

5.2.2 Electrical Conductivity

The electrical conductivities of $Ba_{1-x}Y_xMoO_3$ (x=0-0.07) perovskites were measured using a 4-point contact method on sintered pellets as outlined in Chapter 2. To prepare pellets for conductivity measurement, 3.5 grams of precursor scheelite phase was weighed into a die and pressed to 15000 lbs for 2 minutes using a Carver laboratory press. The scheelite pellets were sintered to 1100°C for 4 hours with heating/cooling ramp rates of 2°C/min. The resulting discs were cut into rectangular pellets followed by the addition of 4 Pt wire electrodes. The Pt wire electrodes were wrapped and subsequently painted over with Pt paste to ensure electrical contact. The pellet was then fired at 800°C for 1 hr to remove the organic binder. The prepped pellet was then contained in a quartz sample tube sealed on either end with rubber septa and placed in a tube furnace controlled by a Barber-Colman temperature controller. 4 lengths of Pt wire served as electrode leads, extending from the quartz sample tube.

The scheelite pellet was reduced at 700°C for 16 hours in flowing H_2 at 50 sccm, maintained with Alicat mass-flow controllers. Following reduction, the outer 2 electrodes were connected to a power supply set to 100 mA constant current and the voltage drop across the inner 2 electrodes was monitored with a digital multi-meter. The temperature was ramped in increments of 100°C with voltage measurements recorded after 30 mins of equilibration at each temperature. The electrical conductivity of the sample was calculated from Ohm's law and the dimensions of the pellet.

5.2.3 Characterization

Powder X-Ray Diffraction (XRD, Philips PW 1830) was used to determine the phase composition and lattice parameters of the perovskite powders. The instrument used CuKα radiation($\lambda = 1.54$ Å) and the scattering angle, 2θ, was scanned between 13° and 90° at a rate of 0.02°/s. Panalytical X'Pert Highscore Plus soft-ware was used for profile refinement and phases were indexed to the Powder Diffraction File database (JCPDS, 2012).

Scanning electron microscopy (SEM, JEOL JSM-7500F) with an energy dispersive X-ray spectroscopy (EDS X-Sight) attachment was used to image the surface morphology of the powders/pellets and provide qualitative elemental composition.

5.2.4 Button Cell Testing

Electrolyte supported cells were assembled following a general procedure used in our group [21,22]. To form the electrolyte, 2 grams of 20% samarium doped ceria (SDC-20, FuelCellMaterials.com) was uni-axially pressed in a 12 mm die to 15000 lbs for 2 minutes. The pellets were sintered at 1400°C for 4 hrs using heating/cooling ramp rates of 2°C/min yielding an electrolyte thickness of ~2 mm. To prepare the anode, a slurry was made consisting of the perovskite powder in an emulsion (20% Triton-X100 / 80% H_2O v/v). The slurry was painted on one side of the electrolyte disc and fired at 1400°C for 4 hours. A platinum mesh current collector (AlfaAesar, 99.9%) was embedded with additional anode slurry and fired again at 1400°C for 4 hours. The cathode consisted of 50% w/w LSCF (FuelCellMaterials.com)/SDC-20 with a Pt mesh current collector and was prepared in the same manner as the anode. The effective electrode areas were 1.5 cm^2. The reference electrode in this setup was a Pt wire wrapped horizontally around the electrolyte and coated in Pt paste that was subsequently heated to 800°C for 2 hrs to remove the organic binder.

Electrochemical tests were performed using a Volta-Lab PGZ 301 (Radiometer Analytical) connected to a desktop computer running VoltaMaster 4 software. The programmed sequence of tests included open cell voltage (OCV), electrochemical impedance spectroscopy (EIS) at OCV (100 kHz to 100 mHz with an AC amplitude of 10 mA), and chrono amperometry (CA) experiments at overpotentials from 0 V to 1.0 V in increments of 50 mV. To ensure adequate sealing, only cells with initial OCVs in H_2 of 0.93 V at 500°C and higher were accepted for complete electrochemical testing.

The analysis of EIS data was performed in the ZView program (Scribner Associates) by fitting impedance curves to an equivalent circuit model ($L_1R_S[R_{CT}CPE_1]$). Only a single depressed semi-circle is apparent in impedance spectra of these materials, therefore a simple circuit model is used. Here, L_1 is an inductor to account for impedance in electrode leads and CPE_1 is a constant phase element accounting for anode current variations (depressed Nyquist semi-circle). The circuit model also consists of a serial resistance (R_s), and a charge transfer resistance of the anode (R_{ct}) used to calculate the exchange current density (i_o) according to the low field approximated Butler-Volmer equation. This circuit model omits certain elements, such as Warburg diffusion parameters, and the anode polarization resistance (R_p) is assumed to be equal to R_{ct}. The cell power densities were calculated from chronoamperometry experiments at various overpotentials.

5.3 Results and Discussion

5.3.1 Characterization

Precursor scheelite materials of formulae $Ba_{1-x}Y_xMoO_4$ (x=0-0.07) were structurally characterized using p-XRD, shown in Figure 5.1. The undoped material, $BaMoO_4$, can be indexed to previously prepared barium molybdate spectra in the literature (PDF: 04-007-8397). The inclusion of Y leads to a slight shift in peak position due to the smaller ionic size of Y^{3+} compared to Ba^{2+}.

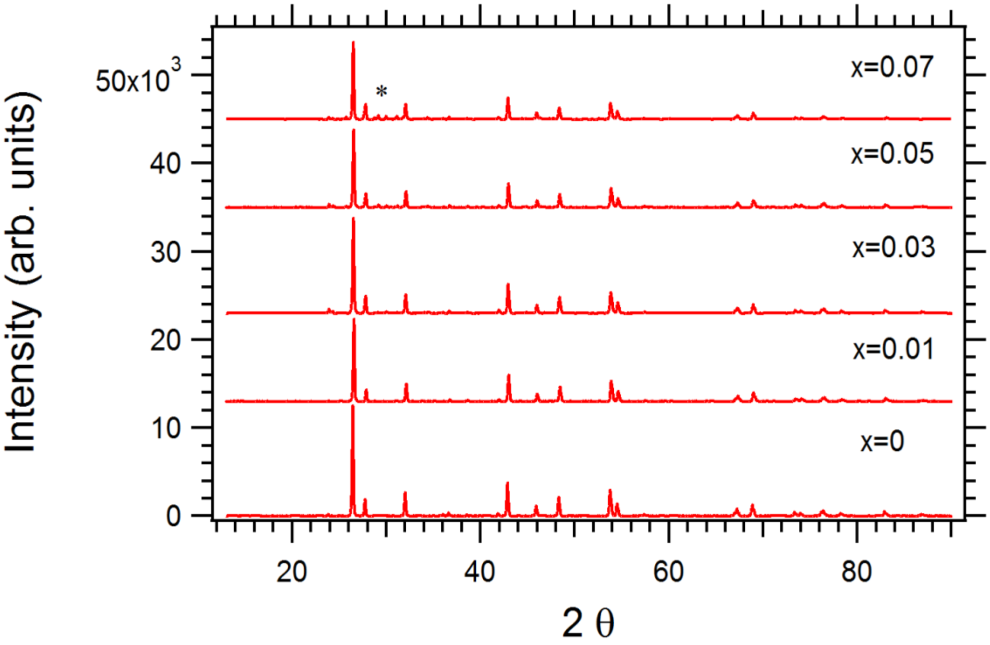

Figure 5.1: p-XRD of $Ba_{1-x}Y_xMoO_4$ (x= 0-0.07) scheelite materials. The asterisk in spectra x=0.07 indicates the onset of yttria phase evolution.

Doping in concentrations of 7% and higher leads to the evolution of new peaks in the diffractogram at 2θ = 29° shown in Figure 5.2, indication of separate phase formation. The formation of this phase is also evident from SEM imaging of the calcined material, shown in Figure 5.2, where small particles on the order of 200-500 nm are visible on the material surface. EDS spot analysis as well as database indexing of the p-XRD indicate that the new phase formed is Y_2O_3 (PDF: 00-001-0831).

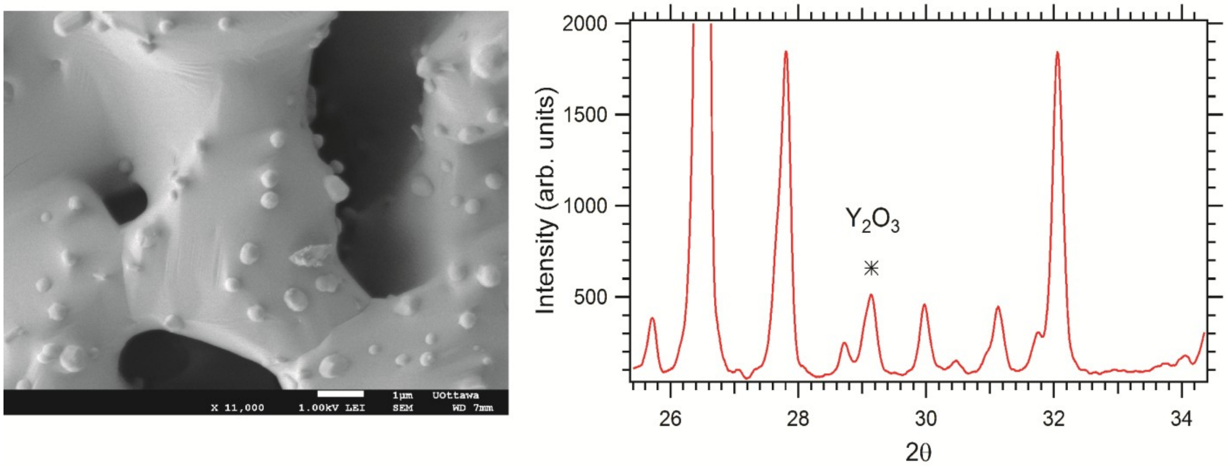

Figure 5.2: SEM and p-XRD (zoomed region) of $Ba_{0.93}Y_{0.07}MoO_4$ Scheelite material, indicating the phase separation of yttria.

Portions of powder samples $Ba_{1-x}Y_xMoO_4$ (x=0-0.07) were further reduced at 700°C in H_2 for 16 hrs, leading to the formation of the perovskite phase. The p-XRD spectra of $Ba_{1-x}Y_xMoO_3$ (x=0-0.07) perovskites post reduction are shown in Figure 5.3. The undoped material indexes well to $BaMoO_3$ (PDF: 00-034-0324) in a cubic perovskite structure with lattice constants $a = b = c = 4.044$ Å. Table 5.1 lists the tolerance factors and lattice parameters obtained from Rietveld refinement of $Ba_{1-x}Y_xMoO_3$ (x=0-0.07) p-XRD spectra. Here, it is evident that Y is incorporated into the perovskite lattice up to 5%. This is also evident from the p-XRD spectra where peaks corresponding to a new phase are present past 5% Y doping. Figure 5.4 plots the cubic lattice constant, a, versus Y concentration. For concentrations of 1-5% Y doping the lattice contracts, indicating incorporation of the smaller A site cation Y^{3+}. Beyond 5% doping there is minimal change in the lattice parameter of the unit cell, correlating well with the formation of a separate phase.

The solubility of Y doping in the similar $2^+/4^+$ perovskite $BaTiO_3$ has been studied in depth, demonstrating that Y^{3+} shows amphoteric behavior (may occupy the A and/or B site) [23–

25]. The amphoteric behavior arises from the intermediate ionic radius of Y^{3+} (r_{ion}= 0.9 Å), allowing for its incorporation in both cation positions within the perovskite lattice [25]. The preference of Y for the A or B site is related to several parameters such as firing atmosphere and temperature, but can be controlled by the relative concentrations of parent A and B cations [23]. In this case, a stoichiometric deficit of A site Ba^{2+} is introduced for the preparation method, leading to Y preferentially doping at the A site. We can conclude from p-XRD data and SEM imaging that the solubility limit of A site Y doping in $BaMoO_3$ is approximately 5% whereas increasing concentrations of Y lead to amphoteric behavior as well as phase separation.

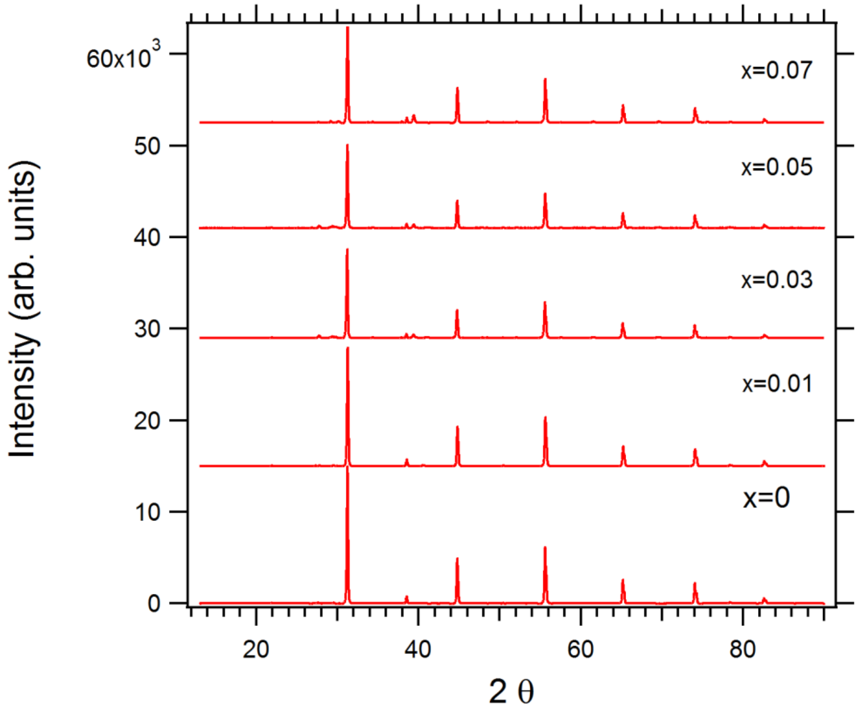

Figure 5.3: p-XRD of $Ba_{1-x}Y_xMoO_3$ (x=0-0.07) perovskites post reduction in H_2.

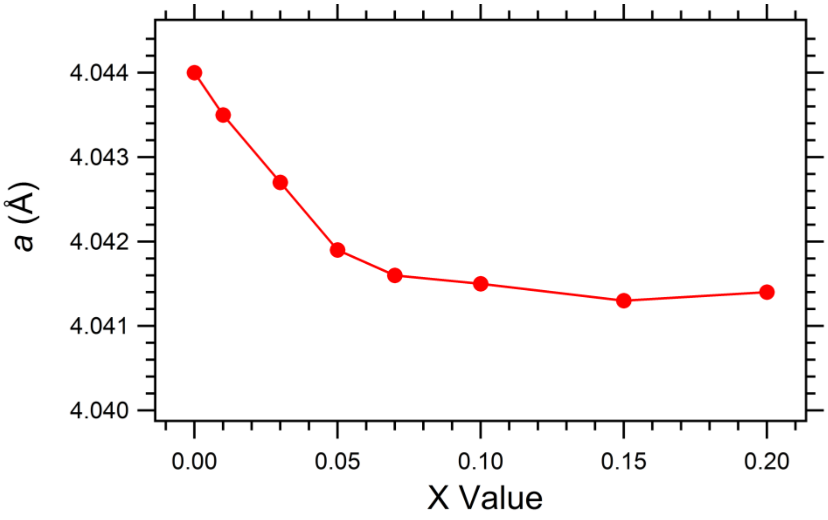

Figure 5.4: Lattice parameter, *a*, versus Y concentration in $Ba_{1-x}Y_xMoO_3$ (x=0-0.20) perovskites.

Table 5.1: Tolerance factors and P-XRD lattice parameters of $Ba_{1-x}Y_xMoO_3$ (x=0-0.20) perovskites.

		Unit Cell	
$Ba_{1-x}Y_xMoO_3$	**Tolerance Factor (*t*)**	***a,b,c* (Å)**	**Volume (Å^3)**
x=0.00	1.035	4.0440	66.135
x=0.01	1.033	4.0435	66.110
x=0.03	1.028	4.0427	66.072
x=0.05	1.023	4.0419	66.032
x=0.07	1.018	4.0416	66.018
x=0.10	1.011	4.0415	66.013
x=0.15	0.998	4.0413	66.003
x=0.20	0.987	4.0414	66.008

Following reduction, the material undergoes significant microstructural changes, evident from SEM imaging shown in Figure 5.5. Reduction to the perovskite phase leads to a highly crystalline material with crystallite sizes ranging from 200-500 nm. The material has moderate porosity with pore sizes on the order of 5-10 μm in diameter, as estimated from SEM imaging.

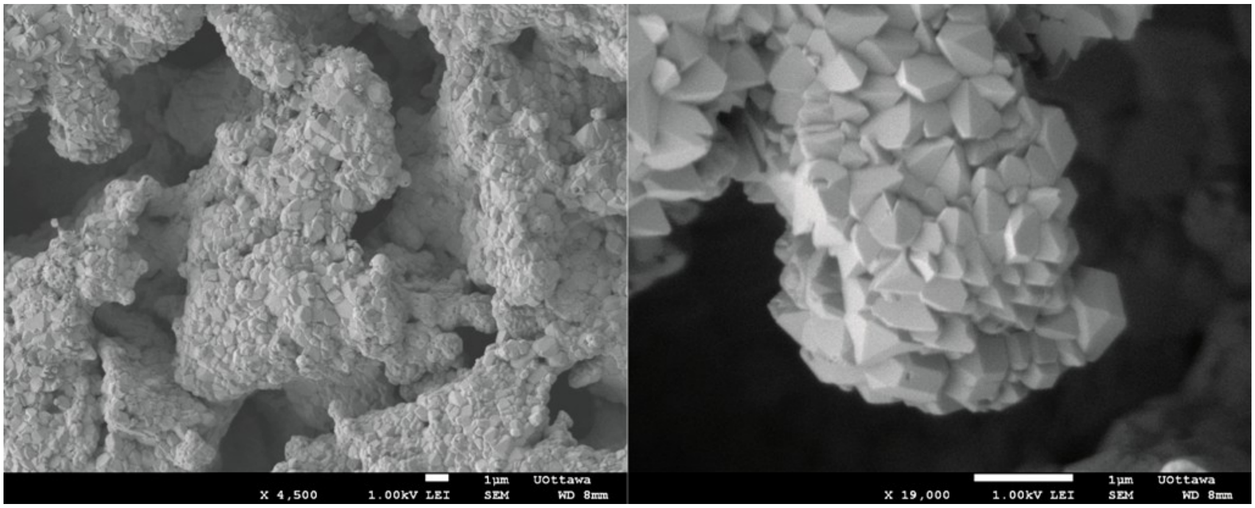

Figure 5.5: SEM images of $Ba_{0.95}Y_{0.05}MoO_3$ perovskite following reduction in H_2.

5.3.2 Electrical Conductivity

The electrical conductivities of $Ba_{1-x}Y_xMoO_3$ (x=0-0.07) perovskites were measured using the 4-point contact method on sintered pellets between 25-1000°C in dry H_2, as shown in Figure 5.6. All materials exhibit metallic behavior, mainly, a decrease in electronic conductivity with increased temperature. $BaMoO_3$ has been previously shown to have impressive metallic conductivity, a claim that is further reinforced in the current study where the undoped sample has σ values of 2500 S/cm and 444 S/cm at 25°C and 800°C respectively [14]. The incorporation of Y at the A site leads to increased resistance in these materials, a trend that is consistent with the inclusion of other dopants such as K^{+1} [14]. Nevertheless, the Y doped samples maintain conductivities between 100-500 Scm^{-1} at 800°C, impressive values in comparison to the majority of perovskites [8,26–29].

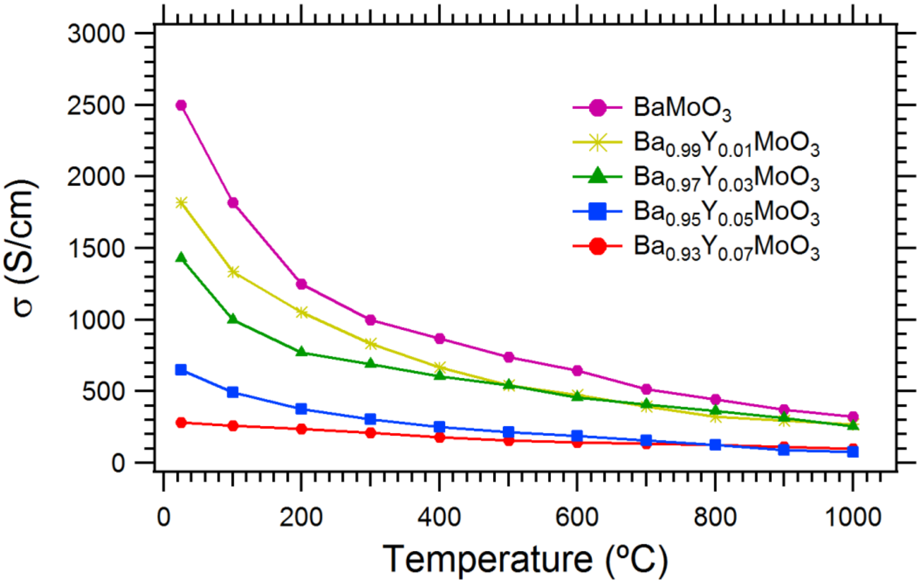

Figure 5.6: Electrical conductivity of $Ba_{1-x}Y_xMoO_3$ (x=0-0.07) perovskites in dry H_2 between 25-1000°C.

The conductivity of these materials is high in a reducing atmosphere, such as H_2, where adsorbed hydrogen may react with oxide species to release electrons to the conduction band. This is shown in Equation 5.1. As well, a bulk reaction may occur at high temperatures where oxygen vacancies are formed through elimination of electron holes, again releasing electrons to the conduction band (Equation 5.2). The high temperature stability of these materials is also heavily reliant on the atmosphere. As is shown in Equation 5.3, the introduction of air readily oxidizes the material back to the scheelite phase where it is an insulator. The oxidation from the perovskite to scheelite phase when exposed to air is expected to occur at temperatures of 473 K and higher [13].

$$2H_{(ads)} + 2O_{(ads)} \rightleftharpoons H_2O + 2e^- \qquad [5.1]$$

$$H_2 + O_O^x + 2h^\bullet \rightleftharpoons H_2O + V_O^{\bullet\bullet} + 2e^- \qquad [5.2]$$

$$Ba_{1-x}Y_xMoO_3 + \frac{1}{2}O_2 \rightleftharpoons Ba_{1-x}Y_xMoO_4 \qquad [5.2]$$

5.3.3 Applications as SOFC anode materials

The effect of Y doping on the anode performance of these perovskites was studied via button cell testing at temperatures between 500-800°C in dry H_2. SDC electrolyte supported cells with anode materials of $Ba_{1-x}Y_xMoO_3$ (x=0, 0.05) were fabricated and tested as outlined in Chapter 2 with results shown in Figure 5.7. Power vs. current density plots of these cells between 500-800°C are shown in Figure 5.7 a and b for anode materials $Ba_{1-x}Y_xMoO_3$ (x=0, 0.05) respectively. It is important to note that the low values for power in this case arise from the button cell geometry used (thick electrolyte). Both anodes exhibit increased power densities at higher temperatures, as expected, with the $BaMoO_3$ anode outperforming the Y doped material. We attribute the decreased power and current densities to the increased electrical resistance of the Y doped perovskite. As previously discussed, the conductivity of $Ba_{0.95}Y_{0.05}MoO_3$ at 500°C is 216 S/cm compared to 741 S/cm for the $BaMoO_3$ material. An increased material resistance leads to an overall decrease in current density for the doped anode material.

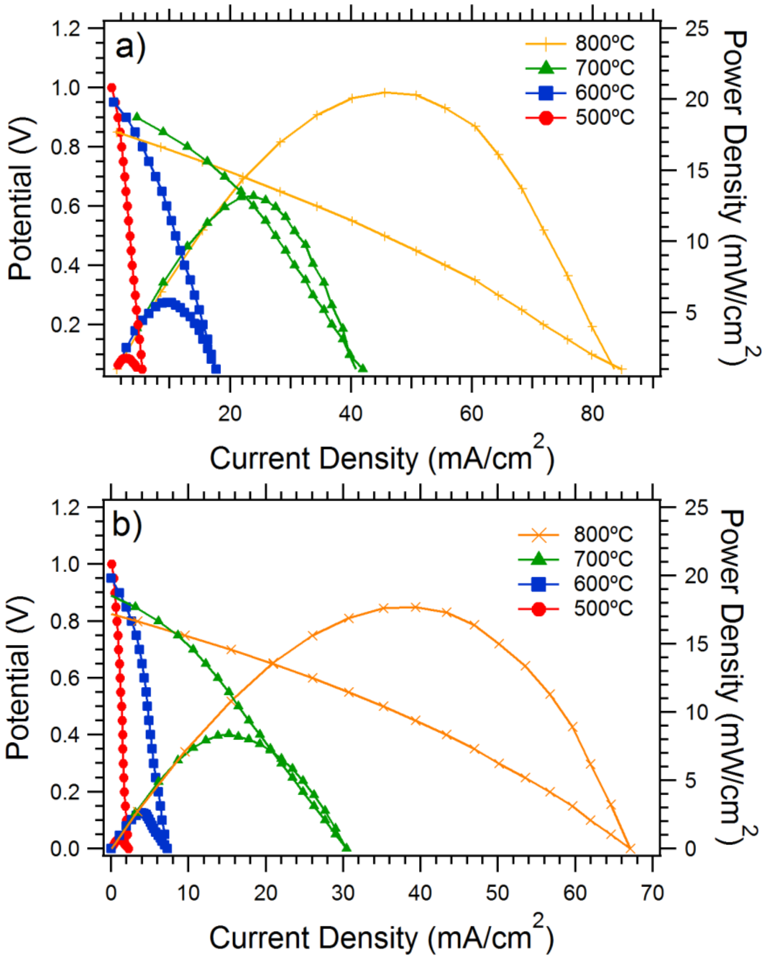

Figure 5.7: Power and voltage vs. current density plots of a) $BaMoO_3$ and b) $Ba_{0.95}Y_{0.05}MoO_3$ anode materials between 500-800°C.

The EIS spectra were fit according to the equivalent circuit ($L_1R_S[R_{CT}CPE_1]$), used previously in this thesis work, with data listed in Table 5.2. The $Ba_{1-x}Y_xMoO_3$ (x=0, 0.05) anode materials have low values for charge transfer resistance (R_{ct}) and therefore high exchange current densities (i_0). An example Nyquist plot for the $Ba_{0.95}Y_{0.05}MoO_3$ anode at 500°C is shown in Figure 5.8. Both cells exhibit high values for serial resistance (R_s), an indication of poor anode-electrolyte connectivity. This is directly related to the preparation of the button cell. This is due to issues with sintering; the molybdate materials did not achieve a good contact when co-sintered with the electrolyte during firing. This is most likely due to the difference in thermal expansions coefficient (TEC) of these perovskites compared to SDC. Ultimately, this leads to an inhomogeneous material connection at the anode-electrolyte interface, shown in Figure 5.9. Nevertheless, this work demonstrates the activity of the $Ba_{1-x}Y_xMoO_3$ (x=0, 0.05) anode materials for H_2 oxidation.

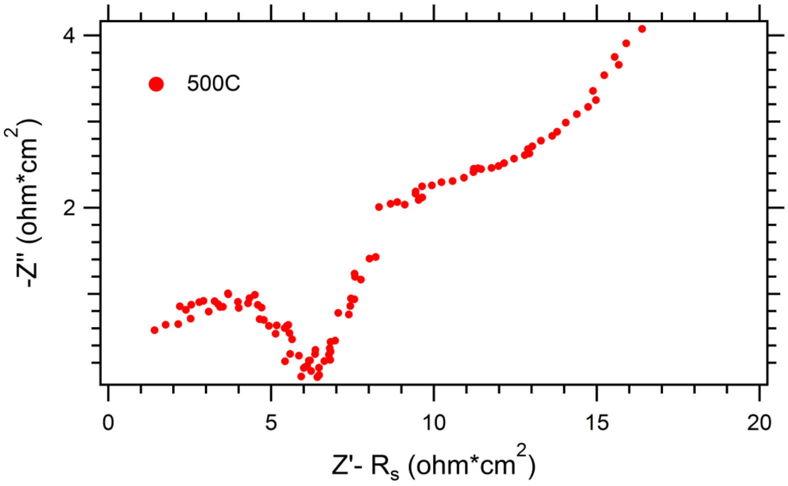

Figure 5.8: Nyquist plot of EIS for $Ba_{0.95}Y_{0.05}MoO_3$ anode at 500°C.

Table 5.2: EIS data for The $Ba_{1-x}Y_xMoO_3$ (x=0, 0.05) anode materials at 500-800°C.

Temperature	**OCV (Volts)**		**R_s (ohm*cm^2)**		**R_{ct} (ohm*cm^2)**		**i_o (mA/cm^2)**	
	x=0	**x=0.05**	**x=0**	**x=0.05**	**x=0**	**x=0.05**	**x=0**	**x=0.05**
500°C	1.019	0.992	32.27	63.83	3.15	6.33	21.12	10.52
600°C	0.961	0.944	15.78	23.71	0.34	1.10	197.65	60.55
700°C	0.891	0.886	8.06	10.58	0.12	0.38	550.48	175.29
800°C	0.807	0.825	7.39	7.29	0.11	0.11	611.09	605.53

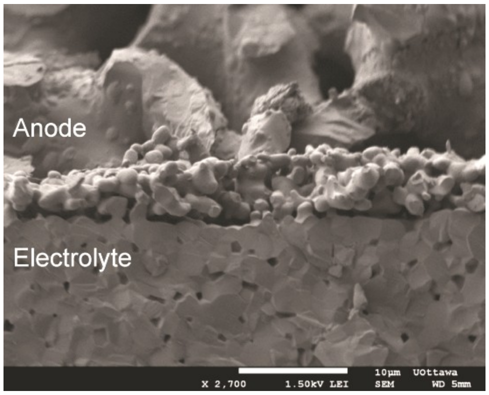

Figure 5.9: Post mortem cross sectional SEM of anode-electrolyte interface of $Ba_{1-x}Y_xMoO_3$ (x= 0.05) fuel cell.

In an attempt to improve the anode-electrolyte contact, hence decreasing the serial resistance, composite materials consisting of 50% SDC/50% perovskite (w/w) were prepared via mixing of the scheelite precursor with SDC followed by 16 hrs reduction in dry H_2 at 700°C. This yields a dual phase perovskite/SDC material that is completely stable to ionic inter-diffusion upon high temperature reduction in H_2. This is illustrated in Figure 5.10. The inclusion of SDC improved the TEC match between anode and electrolyte, thereby allowing for the high temperature co-sintering of these anode materials. SDC is known to have high ionic conductivity and should therefore increase the size of the triple phase boundary (TPB) as outlined in Chapter 1, however, when tested for performance at 800°C the EIS data revealed a drastic increase in both serial resistance and charge transfer resistance. Figure 5.11 shows an EIS Nyquist plot for the x=0.05 anode at 800°C. Clearly, the addition of SDC to form a composite anode material immensely reduces the electronic conductivity of the anode, hindering performance. As well, it has been previously concluded that the catalytic performance of similar perovskite materials is directly related to the B site Mo. This means that the formation of a composite anode material not only reduces the electronic conductivity, but also decreases the amount of Mo and therefore the catalytic performance of these cells. Therefore, one may conclude that the electronic conductivity as well as Mo content is crucial to the performance of these perovskites as SOFC anode materials.

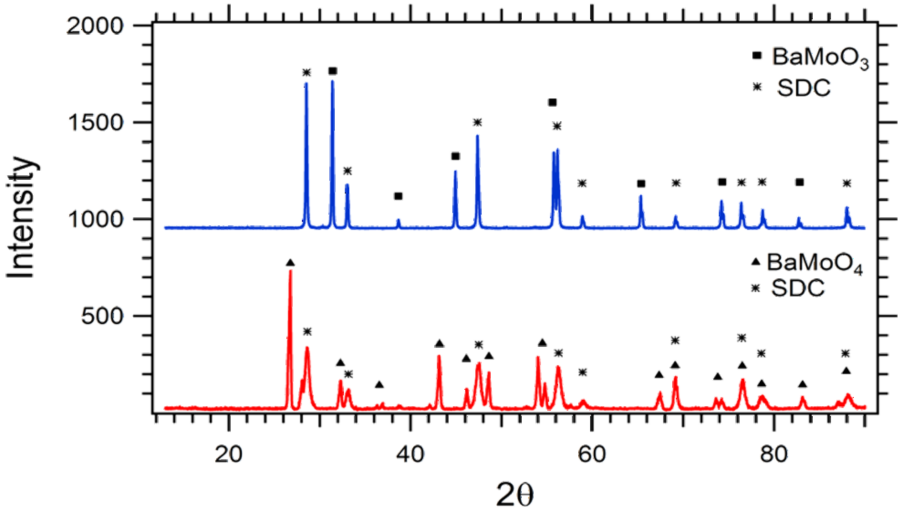

Figure 5.10: p-XRD spectra of Scheelite/SDC to perovskite /SDC composite material before and an after reduction in H_2 at 700°C.

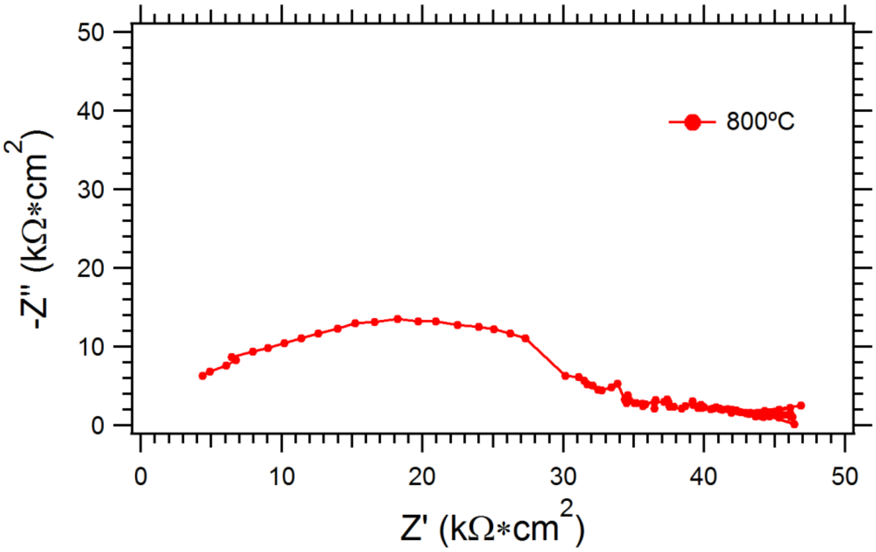

Figure 5.11: EIS Nyquist plot of $BaMoO_3$ / SDC composite anode at 800°C.

As mentioned previously, the rapid high temperature oxidation of these materials means that the perovskite structure, and hence high conductivity, is only stable in a reducing atmosphere. Interestingly, post mortem p-XRD of the tested anode materials, $Ba_{0.95}Y_{0.05}MoO_3$ anode for example, revealed that the dominant phase is the oxidized scheelite form (Figure 5.12a). The oxidation to the perovskite may occur during the quenching procedure, in which the Pyrex seal at the anode side of the button cell is particularly susceptible to cracking. The formation of even slight cracks in the seal would lead to an inflow of air to the anode at elevated temperature; a possible explanation for the re-oxidation upon cooling. In addition to cracks in the Pyrex seal, drawing current from the button cell during chronoamperometry experiments may lead to partial oxidation of the perovskite at the anode-electrolyte interface from the diffusion of oxide species through the SDC electrolyte. To test for oxidation due to cracks, another fuel cell consisting of a $Ba_{0.95}Y_{0.05}MoO_3$ anode was mounted on the test apparatus, sealed at 950°C in air, and then reduced in a typical fashion in dry H_2 overnight. An OCV experiment confirmed complete sealing of the cell. Then, instead of quenching, the cell was slow cooled to room temperature with a constant flow of H_2 to the anode. The p-XRD of the anode post cooling (Figure 5.12 b) indicates the retention of the perovskite phase. This confirms the hypothesis that the re-oxidation witnessed previously is a result of cracks formed during rapid cooling of the fuel

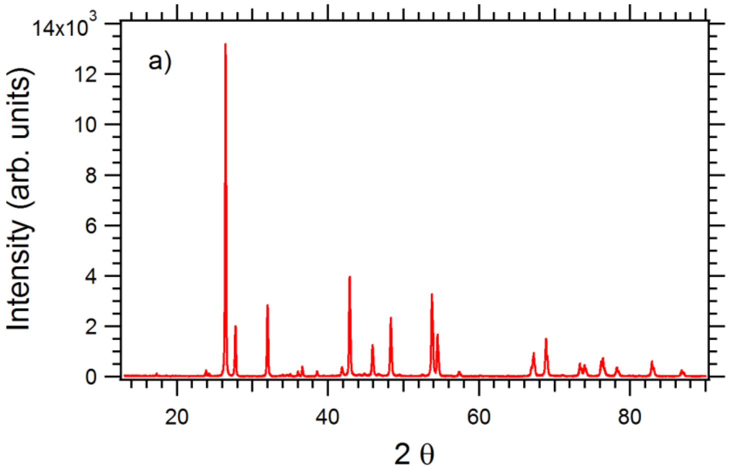

cell.

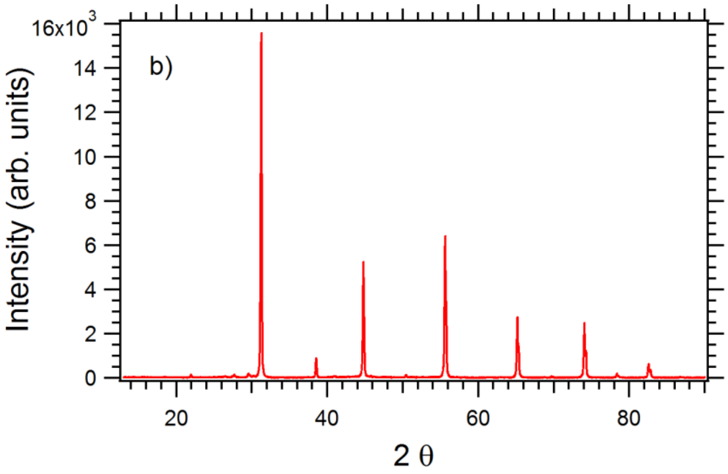

Figure 5.12: Post mortem p-XRD of $Ba_{0.95}Y_{0.05}MoO_3$ anodes after a) quenching and b) slow cooling.

This is intriguing when considering the results of the composite anode ($Ba_{0.95}Y_{0.05}MoO_3$ /SDC) testing outlined previously (Figures 5.10 and 5.11). This cell exhibited extremely high values for both R_s and R_{ct} (Figure 5.11), an indication of poor anode performance or poor contact from sintering. The high resistance of this anode may also be attributed to an incomplete sealing of the cell, leading to the oxidized scheelite form of the anode instead of perovskite when measuring the impedance. The highly insulating scheelite phase would exhibit large values for both R_s and R_{ct} when analyzing the EIS data. Repeated tests with optimized cell sealing may lead to the retention of the perovskite and hence improved results. Aside from the integrity of the gas seal, one cannot rule out the possibility of full or partial oxidation of the perovskite to the scheelite phase due to the diffusion of oxide anions to the anode during operation.

5.4 Conclusion

A new perovskite family $Ba_{1-x}Y_xMoO_3$ (x=0-0.05) has been prepared via high temperature reduction of the corresponding scheelite type precursors followed by structural and electronic characterization. Refinement of the p-XRD spectra as well as SEM imaging conclude that the solubility limit of Y doping at the A site is 5 mol%, beyond which Y_2O_3 segregation occurs. 4-point electronic conductivity measurements on sintered pellets indicate that the undoped $BaMoO_3$ sample has a colossal room temperature conductivity of 2500 S/cm in dry H_2. As well, all materials investigated maintain metallic conductivity in the temperature range of 25-1000°C with resistance increasing upon Y doping. The $Ba_{1-x}Y_xMoO_3$ (x=0, 0.05) materials exhibit good performance as SOFC anode materials between 500-800°C, with R_{ct} values at 500°C in dry H_2 of 3.15 and 6.33 ohm*cm^2 respectively. The formation of a 50% SDC/50% perovskite (w/w) composite anode yields a stable material that can be co-sintered with the SDC electrolyte. Results of composite anode testing indicated poor performance, however we conclude that the integrity of the Pyrex seal may be in question, confirmed by post mortem p-XRD of quenched vs. slow cooled anodes.

5.5 References

[1] P. Cowin, C. Petit, R. Lan, J.T.S. Irvine, S. Tao, Adv. Energy Mater. 1 (2011) 314.

[2] J.B. Goodenough, Y.-H. Huang, J. Power Sources 173 (2007) 1.

[3] J.T.S. Irvine, Perovskite Oxide for Solid Oxide Fuel Cells, Springer US, Boston, MA, 2009.

[4] S.C. Singhal, K. Kendall, High Temperature Solid Oxide Fuel Cells, Elsevier Ltd, New York, USA, 2003.

[5] C. Sun, U. Stimming, J. Power Sources 171 (2007) 247.

[6] S. Suthirakun, G. Xiao, S.C. Ammal, F. Chen, H.-C. zur Loye, A. Heyden, J. Power Sources 245 (2014) 875.

[7] S. Hui, A. Petric, J. Eur. Ceram. Soc. 22 (2002) 1673.

[8] D.P. Fagg, V. V Kharton, A. V Kovalevsky, A.P. Viskup, J. Eur. Ceram. Soc. 21 (2001) 1831.

[9] S.M. Bukhari, J.B. Giorgi, ECS Trans. 33 (2011) 81.

[10] K. Kurosaki, T. Oyama, H. Muta, M. Uno, S. Yamanaka, J. Alloys Compd. 372 (2004) 65.

[11] S. Yamanaka, K. Kurosaki, T. Maekawa, T. Matsuda, S. Kobayashi, M. Uno, J. Nucl. Mater. 344 (2005) 61.

[12] I. Nagai, N. Shirakawa, S. Ikeda, R. Iwasaki, H. Nishimura, M. Kosaka, Appl. Phys. Lett. 87 (2005) 024105.

[13] J. Kubo, W. Ueda, Mater. Res. Bull. 44 (2009) 906.

[14] S.B. Zhang, Y.P. Sun, B.C. Zhao, R. Ang, X.B. Zhu, W.H. Song, J. Alloys Compd. 479 (2009) 22.

[15] R. Martínez-Coronado, J. a. Alonso, a. Aguadero, M.T. Fernández-Díaz, J. Power Sources 208 (2012) 153.

[16] R. Martínez-Coronado, J. a. Alonso, a. Aguadero, M.T. Fernández-Díaz, Int. J. Hydrogen Energy (2013) 1.

[17] Q. Liu, D.E. Bugaris, G. Xiao, M. Chmara, S. Ma, H.-C. zur Loye, M.D. Amiridis, F. Chen, J. Power Sources 196 (2011) 9148.

[18] Y.-H. et al. Huang, Science (80-.). 312 (2006) 254.

[19] T.G. Howell, C.P. Kuhnell, T.L. Reitz, a. M. Sukeshini, R.N. Singh, J. Power Sources 231 (2013) 279.

[20] B. He, Z. Wang, L. Zhao, X. Pan, X. Wu, C. Xia, J. Power Sources 241 (2013) 627.

[21] S.M. Bukhari, J.B. Giorgi, J. Power Sources 198 (2012) 51.

[22] C.M. Grgicak, R.G. Green, J.B. Giorgi, J. Power Sources 179 (2008) 317.

[23] M. Lin, H. Lu, Mateirials Sci. Eng. Sci. Eng. 335 (2002) 101.

[24] P. Blanchart, J.F. Baumard, P. Abelard, J. Am. Ceram. Soc. 72 (1992) 1068.

[25] Y. Tsur, T.D. Dunbar, C.A. Randall, J. Electroceramics 2 (2001) 25.

[26] Z. Cheng, S. Zha, L. Aguilar, D. Wang, J. Winnick, M. Liu, Electrochem. Solid-State Lett. 9 (2006) A31.

[27] T. Miruszewski, B. Bochentyn, J. Karczewski, M. Gazda, B. Kusz, Cent. Eur. J. Phys. 10 (2012) 1202.

[28] H. Wiemhofer, Solid State Ionics 175 (2004) 93.

[29] J.J. Tunney, M.L. Post, J. Electroceramics 51 (2000) 63.

Chapter 6
Conclusions

The development of new perovskite materials for SOFC anodes and electrochemical gas sensors is currently an area of intense chemical research. The optimization of their electronic properties through elemental doping may one day lead to the incorporation of perovskites into many technological fields. Three separate perovskite systems have been investigated in this work, with intriguing and promising results when applied as sensors and SOFC anode materials.

Primary findings of this work concluded that low mol% A site Ce doping in the $BaFeO_3$ perovskite leads to several advantageous properties. The incorporation of 5 mol% Ce changes the perovskite structure from hexagonal to cubic and, in doing so, leads to the formation of oxygen vacancies through charge compensation. The net result is an increase in total conductivity throughout the entire temperature range, reaching a value of 3.3 S/cm at 800°C in air. It was further determined that the increase in total conductivity arises from increased electronic and ionic conductivities in the material. The $Ba_{0.95}Ce_{0.05}FeO_{3-\delta}$ material was found to have the highest conductivity and was further tested as an oxygen sensor at temperatures of 500-700°C. The sensor experiments yielded reproducible, linear sensing behavior for oxygen concentrations of 25-45% in air. As well, the high temperature bulk equilibration of oxygen throughout the material leads to promising temperature independent sensing behavior. Testing of these materials in a more predictable manner, with the utilization of a spray system and thin film sensor setup, should yield a behavior that may be compared to conventional state of the art oxygen sensors used in commercial lean burn engines.

Perovskites are also promising candidates as SOFC anode materials in light of the limitations of conventional Ni-YSZ anodes employed today. Perovskites with formulae

$Sm_{0.95}Ce_{0.05}Fe_{1-x}M_xO_{3-\delta}$ where the dopant M is either Co or Ni in 3 mol% have previously been shown to be active as SOFC anode materials at intermediate temperatures (500-800°C) for H_2 and CH_4 oxidation. In order to advance research into these types of perovskites, an investigation into their sulfur tolerance is crucial. Therefore, three perovskites $Sm_{0.95}Ce_{0.05}FeO_{3-\delta}$, $Sm_{0.95}Ce_{0.05}Fe_{0.97}Ni_{0.03}O_{3-\delta}$ and $Sm_{0.95}Ce_{0.05}Fe_{0.97}Co_{0.03}O_{3-\delta}$ were tested as anode materials at 500°C in two concentrations of H_2S: 0.5% and 5% balanced in H_2. Interestingly, H_2S significantly enhances the performance of these anode materials, verified by impedance spectroscopy and DC chronoamperometry experiments. The improvement arises from a surface sulfidation of the perovskite anode microstructure, leading to the formation of metal sulfides that increase the overall anode conductivity. Extensive post mortem analysis revealed that the presence of H_2S also forms a highly conductive FeS_2 layer at the anode-electrolyte interface, dramatically improving the electrode contact through a decrease in resistance. The SCF-Co anode exhibited the most promising improvement, with an increase in exchange current density, i_o, from 13.72 to 127.02 mA/cm^2 when switching from H_2 to 0.5% H_2S/99.5% H_2 fuel composition. Recovery tests performed on the SCF-Co anode conclude that the open cell voltage (OCV) and power density of these cells recover within 4 hours of H_2S removal. We conclude that the formation of metal sulfide species is only partially reversible, yielding an anode material with an overall lower R_{ct} upon switching back to pure H_2. This is verified by post mortem SEM imaging where clusters of metal sulfides remain on the perovskite surface after recovering in H_2.

Combining their performance in sulfur containing fuels with their previously reported coke tolerance makes these perovskites especially attractive as low temperature SOFC anodes in sour fuels. Especially of interest is the improvement witnessed when switching to a mixture of

H_2S and H_2 fuel. Further research should investigate the sulfur tolerance of these materials when utilizing carbon based fuels such as CH_4. The sulfidation improvement witnessed in H_2S/H_2 may also be evident when utilizing methane with sulfur impurities. This is of interest when considering the anode coking as well since these materials have previously been demonstrated to be coke resistant.

The final area of research for this thesis involved the structural and electronic effects of Y doping in the $BaMoO_3$ perovskite system, with a primary goal of improving the ionic conductivity in these materials. Structural characterization revealed that Y has a moderate solubility at the A site in $BaMoO_3$, with an experimental solubility limit of 5 mol%. As well, these perovskites have colossal electronic conductivities, as high as 2500 S/cm in dry H_2, which decrease with increasing concentrations of Y. The decrease in electronic conductivity upon Y doping is expected and, if accompanied by an improvement in ionic conductivity, should yield a promising MIEC for SOFC anode applications. Difficulties arise when considering the redox chemistry of these perovskites since they readily oxidize to the scheelite structure when exposed to air at elevated temperatures. This limits the measurement of conductivity to a reducing atmosphere. Further work should consider alternative methods to separate and measure the ionic and electronic contributions to total conductivity.

To compare their performance as SOFC anode materials, the $BaMoO_3$ and $Ba_{0.95}Y_{0.05}MoO_3$ perovskites were tested at temperatures of 500-800°C in dry H_2. The undoped material exhibited the most promising performance, with low values for charge transfer resistance and high exchange current densities. Further testing as a composite anode material (50% w/w perovskite/SDC) resulted in poor performance, evident from EIS experiments. However, post mortem XRD imaging of the anode indicates that the Pyrex gas seal is especially important when considering the performance of these materials due to the ease of oxidation when exposed to air at high temperatures. Further experimentation with alternative sealing materials may improve the performance of the barium molybdates by ensuring complete isolation from air at the anode, thereby avoiding oxidation from perovskite to the insulating scheelite phase.